KINETIC CHARACTERIZATION OF ENHANCED IMPURITY SPUTTERING DUE TO ION CYCLOTRON RADIO-FREQUENCY HEATING

BY

MOUTAZ ELIAS

DISSERTATION

Submitted in partial fulfillment of the requirements
for the degree of Doctor of Philosophy in Nuclear, Plasma and Radiological Engineering
in the Graduate College of the
University of Illinois Urbana-Champaign, 2021

Urbana, Illinois

Doctoral Committee:

Associate Professor Davide Curreli, Chair
Professor Rizwan Uddin
Professor David N. Ruzic
Dr. James Myra

ABSTRACT

Ion Cyclotron Resonance Heating (ICRH) devices are a cornerstone in the auxiliary heating requirement of future fusion devices as they are the most advanced and cost-effective option to heat the plasma. However, RF sheaths have been a major concern accompanying the use of ICRH systems. The presence of RF sheaths has been experimentally and theoretically linked to the enhancement of the impurity flux sputtered from the Plasma Facing Components. It is a pivotal task to minimize the impurity emission from the PFC of the ICRH system. Several mitigation strategies have been developed and tested on smaller scale devices experimentally. Previous attempts to model RF sheaths and PMI are limited to electromagnetic simulation and at best a fluid description of the plasma without any PMI simulations. RF sheaths require a detailed kinetic ion simulation that captures the ion dynamics in order to provide an accurate description of the IEAD at the PFC, particularly a Particle-In-Cell simulation would be advantageous. Using Maxwell-Boltzmann electrons would allow to overcome some of the limitations connected to the fast electron physics, but in order to avoid spurious electrostatic oscillations, it would require to enforce global charge conservation for transient and RF sheath plasma simulations.

In this work we developed a new charge conservation scheme enabling the treatment of RF sheaths, and other type of transients, in hybrid Particle-in-Cell codes having kinetic ions and Maxwell-Boltzmann electrons. We report

numerical tests on magnetized Radio-Frequency plasma sheath designed to test the stability and ability of the scheme to capture important RF sheath phenomena. An extensive benchmarking comparison of time-averaged and time dependent profiles with fluid codes is also reported. The developed hPIC model is used to analyze the dependence of the kinetic IEAD impacting on the RF antenna at various RF sheath parameters. Furthermore, a simulation case representing the latest JET campaign was analyzed. We found that in typical tokamak conditions of grazing magnetic field incidence, the IEAD of the ions impacting on the surface of the RF actuator exhibits a "phase-space cusp", which can be explained as an effect due to finite ion Larmor radius.

In order to quantify material emission consequent to ion bombardment, the hPIC framework was interfaced to the RustBCA sputtering code. RustBCA is a previously-developed binary-collision-approximation code, which can be used to simulate material sputtering in time resolved conditions. Time resolved coupling allowed us to inspect changes in sputtering yield during one RF cycle. We found that the yield has a highly non-linear evolution during the RF cycle, which is a consequence of the exponential dependence of sputtering vs. energy across the sputtering threshold.

Finally, we performed a preliminary validation using experimental data taken at the RF limiter on the WEST tokamak at CEA, France, with the goal of comparing the results from hPIC-RustBCA against experimental measurements. In order to allow the comparison against OES (Optical Emission Spectroscopy) acquisitions, we converted the sputtered fluxes calculated by the code into absolute spectral radiance. We found reasonable agreement between the calculated values and the experimental measurements of the tungsten W I optical line emission at 400.9 nm, representative of the amount of sputtered tungsten. The multiple sources of uncertainties affecting the

validation have been discussed, namely the high variability of the inverse photon efficiency S/XB, the actual impurity composition of the plasma (O, C, F, Cu, etc.), and the effect of higher charge states (O^+, O^{2+}, O^{3+}, ..., O^{8+}). A systematic analysis of the different sources of uncertainty has been reported.

شكراً لكَ أبي..

شكراً لكِ أمي..

لن أنسى أنكما من صنعتا مني رجلاً ناجحاً.

ACKNOWLEDGMENTS

A Ph.D. is not merely an academic degree, it is a period of rapid change in mindset and education. I am grateful to everyone who took part in this journey in both aspects. I would like to express my sincerest appreciation to my mentor and advisor, Professor Davide Curreli. I could not have found a mentor more suited for my journey. You were hands-on when I needed it and gave me the space to explore when I was ready. The troubles faced were in no way what you signed up for or expected, yet you helped me through them at the cost of your own self-interest. I am a much better researcher thanks to your leadership by example. Your support and guidance made this Ph.D. a lot smoother and enjoyable.

I would also like to thank, Professor Rizwan Uddin. Being your teaching assistant was a stroke of luck. I was always happy to pass by you, meet at the cafés and ask my never ending questions. You shared with me years of wisdom about the academic field and living in a foreign land. Special thanks to Dr. James Myra, a world expert in RF sheath physics. Even though we are decades apart in years and experience, you treated me as an equal and provided a plethora of knowledge.

I want to thank the members of the Laboratory of Computational Plasma Physics for their discussion, shared agony, and support. Mohammed Mustafa and Jon, your help was prompt and crucial. Without it would have taken me at least another semester to graduate. Rabel Rizkallah for the countless

physics debates. Logan, Dr. Rinat and Shane, it was always interesting to strike up a conversation about plasma, computation or AI. Steven, Mikhail, Mohammed Metwally, Sonata and Xin Zhi, our yearly trips to APS were always eventful and fun.

To my roommates, Dr. Ophelia Bolmin, Dr. Fouad Amer and Dr. to be Paul Gharzouzi, it was a pleasure sharing the vast majority of my time with you. Ophelia Bolmin for her putlocks, food and gym encouragements, Fouad for his wisdom and the scent of home, and Paul for his uplifting presence, hilarious joke and making errands enjoyable. The memories and tales of bil laban family will stay with me for years. Through the hardships, growth, changes, and new experiences I cannot understate what a crucial part of my support system you were. Dr. Adriano Abrantes, my first roommate and person to spend the most relaxing time with.

To Omnia, a 10-hour time difference still could not stop us from spending hours on the phone. You were my confidant, my thinking partner, and a lifeline during the dark times. You were proud of me when no one else was, for that I will be eternally grateful. To Amira, my errand friend, will never forget how you made me feel, you will always be a part of who I am. I will try your tea one day. I will miss you. To Dr Walid, you were always an aspiration. I hope we continue to meet on more continents. You showed me what kind of happiness I wanted, explicitly with wisdom and implicitly by example. To Omnia, Amira and Dr. Walid, Thank you for your unconditional love and support.

To my Champaign friends who have supported me during my time as a graduate student: Ali Kanj for the cultural addition, Mamdouh AlGhzawi for the countless hosted nights generosity and thinking of others, Mohammed Mustafa for discussion on society situations, Ibrahim AlJarrah the perfect

partner for any activity or project for the countless help throughout the years with courses, gym, life and ego, Issam Qamhiyeh for the endless trix nights, Hania Taha for making my life eventful, Elena and Leandro my favorite Italians, Oliver for fact checking, Nabil Ramlawi for his oud, Mohamemd ElMasri for Huda and Zeina, Duha for her laughter, Mohammed Rashad for his coaching, Ghada for physio therapy walks, Hussien Sibaie for his stories, Lina farouk for an endless list of items including but not limited to board games, volleyball, food, company, and most importantly constant support, Hassan Dbouk for his stickers and sarcastic comments, Sari Alkhatib for the endless meals, walks and talks, Omar Darwaish for his smile, Mohammed Hatem for his dark sense of humor, Sohaila Aboutaleb for the introduction to egyptian folk music and proofreading, Bayan Hamdan for poke ball and spicy drama, Amira and Omar Elsherbiney for making my life seem well managed in comparison, Watheq Sayeh for football analysis, Amir Ibrahim, Mohammed Metwally and Ahmed Helmy for chivalry,

To my friends around the world Lamia, Abduallah Habashy, Yumna, Abdulrahman Amarneh, and Bilal, 5 years apart and you made me genuinely happy the second I met you again. To Reinad and Mohammed Arif, my favorite couple, you are dear to me each apart and invaluable together. Mohammed Alsayadi and Mohammed Aljallaf, my time with you is always special joyful and most importantly intellectually lovely. To all my friends around the world not mentioned in here by name I have not forgotten you, Thank you for every second of support, and apologies for any dereliction.

Finally, I would like to thank my parents and my brother Sewar, whom this thesis is dedicated to. To Sewar, I am always proud of you and glad to be there when you need me. This thesis is as much yours as it is mine. I am forever indebted to you.

TABLE OF CONTENTS

LIST OF TABLES

LIST OF FIGURES

LIST OF ABBREVIATIONS

ADAS	Atomic Data and Analysis Structure
BCA	Binary Collision Approximation
DS	Debye Sheath
EAD	Energy Angle Distribution
ECRH	Electron Cyclotron Resonance Heating
FA	Field Aligned
FS	Faraday Screen
FW	Fast Wave
hPIC	hybrid Particle-In-Cell
ICRH	Ion Cyclotron Resonance Heating
IEAD	Ion Energy Angle Distribution
IEM	Impurity Emission Model
ITER	International Thermonuclear Experimental Reactor
MPS	Magnetic Pre-Sheath
NBI	Neutral Beam Injectors
PFC	Plasma Facing component
PIC	Particle-In-Cell
PMI	Plasma Material Interaction
RF	Radio-Frequency
SEE	Secondary Electron Emission
SW	Slow wave
TA	Toroidally Aligned

CHAPTER 1

INTRODUCTION

1.1 The need for auxiliary heating in fusion reactors

Nuclear energy encompasses any energy derived from nuclear reactions. The principle of mass–energy equivalence, stated by Einstein's famous equation $E = mc^2$, allows the extraction of huge amounts of energy from the small difference in masses between the reactants and the products. There are three possible types of nuclear reactions which can be harvested for power generation fission, fusion and decay. Nuclear fusion, while not an established commercial power source, remains the focus of international research with the largest International Thermonuclear Experimental Reactor (ITER) in its final stages.

For Deuterium-Tritium nuclear fusion reactors to produce a net positive energy, reactors are required to operate at $T = 15$ KeV. Heating and maintaining the plasma to $T = 15$ KeV using auxiliary heating alone requires a constant supply of power that will deem a commercial power plant unattainable. Luckily, heating the plasma can be split into two phases $0 - 6$ KeV and $7 - 15$ KeV. During phase one, the plasma has to be heated externally using ohmic and auxiliary heating until it reaches temperature of $5 - 7$ KeV. During this phase the self heating of the plasma from fusion byproducts, known as alpha heating, is negligible. At phase two, when the plasma crosses the $5 - 7$ KeV threshold, the alpha heating starts to dominate, heating the plasma

to temperatures that allow ignition. The presence of alpha heating allows us to decrease the auxiliary heating power required to sustain the plasma and extract a net positive electrical output from the fusion reactor. There are several methods, each with their advantages and limitations, that can be used to deliver power to the reactors during phase one.

Table 1.1: Auxiliary Heating systems. Advantages and disadvantages of NBI, ECRH, ICRH and LHCD.

Parameter	**NBI**	**ECRH**	**ICRH**	**LHCD**
Cost ($\$/W$)	4	6	2	3
Source Requirement	1 MeV	140 GHz	40 MHz	3 GHz
Advantages	Feeds fuel to the plasma	Does not require plasma proximity	Cheapest and least technical challenges	Can be used for current drive
Disadvantage	Need to develop 1MeV ion sources	Need to develop 140GHz wave source	Proximity to plasma	Low efficiency

While several auxiliary heating systems shown in Table 1.1 are available, there is no clear winner for fusion devices the size of ITER. With the exception of ICRH, all have considerable technological challenges and require the development of sources to fit ITER. A detailed description of the advantages and disadvantages as well as technological challenges associated with each heating system is presented[1]. Ion Cyclotron Resonance Heating (ICRH) systems are currently the most cost effective and cheapest auxiliary heating systems [1]. Additionally, ICRH uses RF waves in the rage of tens of Mega-Hertz giving it an advantage in terms of density limits for propagation into the plasma. This thesis is centered around the use of Ion Cyclotron Resonance Heating (ICRH) in tackling a crucial problem in fusion power plants, plasma heating. This chapter provides a detailed overview of the problems

associated with the use of ICRH as well the current state of research in terms of mitigation strategies proposed.

1.2 The role of Ion Cyclotron Resonance Heating

ICRH heating technique is based on the principal of wave resonances and energy transfer. Through different energy transfer mechanisms, RF waves can transfer their energy into the plasma particles. The are specific characteristic frequencies for each plasma species j where the energy transfer is facilitates. Most notable of these is the cyclotron frequency(ω_{cj}) where most of the resonant energy transfer happens. At resonance, the wave creates an electric field that aligns with motion of the plasma species throughout the gyro orbit providing constant acceleration for the plasma species as the wave energy damps out. The process of cyclotron resonance is demonstrated in Fig 1.1.

By tuning the RF wave frequency to the specific cyclotron frequency(ω_{cj}), we are able to control not only the mechanism of interaction and energy deposition, but also which species is the energy deposited in. The ICRH technique targets the ion cyclotron frequency(ω_{ci}). The waves are created in gyrotrons launched into the plasma through a serious of wave guides and an antenna. Our main concern in this thesis are the components of the ICRH that interact with the plasma edge.

Plasma facing components of an ICRH system

The two main components of the ICRH system that interact with the plasma are the ICRH antenna faraday screen (FS) and the ICRH antenna limiters. The FS and limiter are shown for JET in Fig 1.2. The main function of

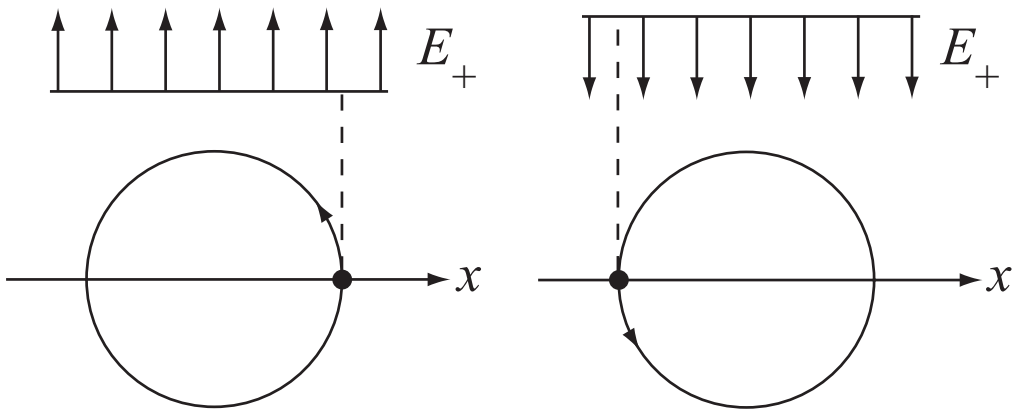

Figure 1.1: Mechanism of cyclotron resonance at the plasma frequency ω_{pi}. Figure from [1]

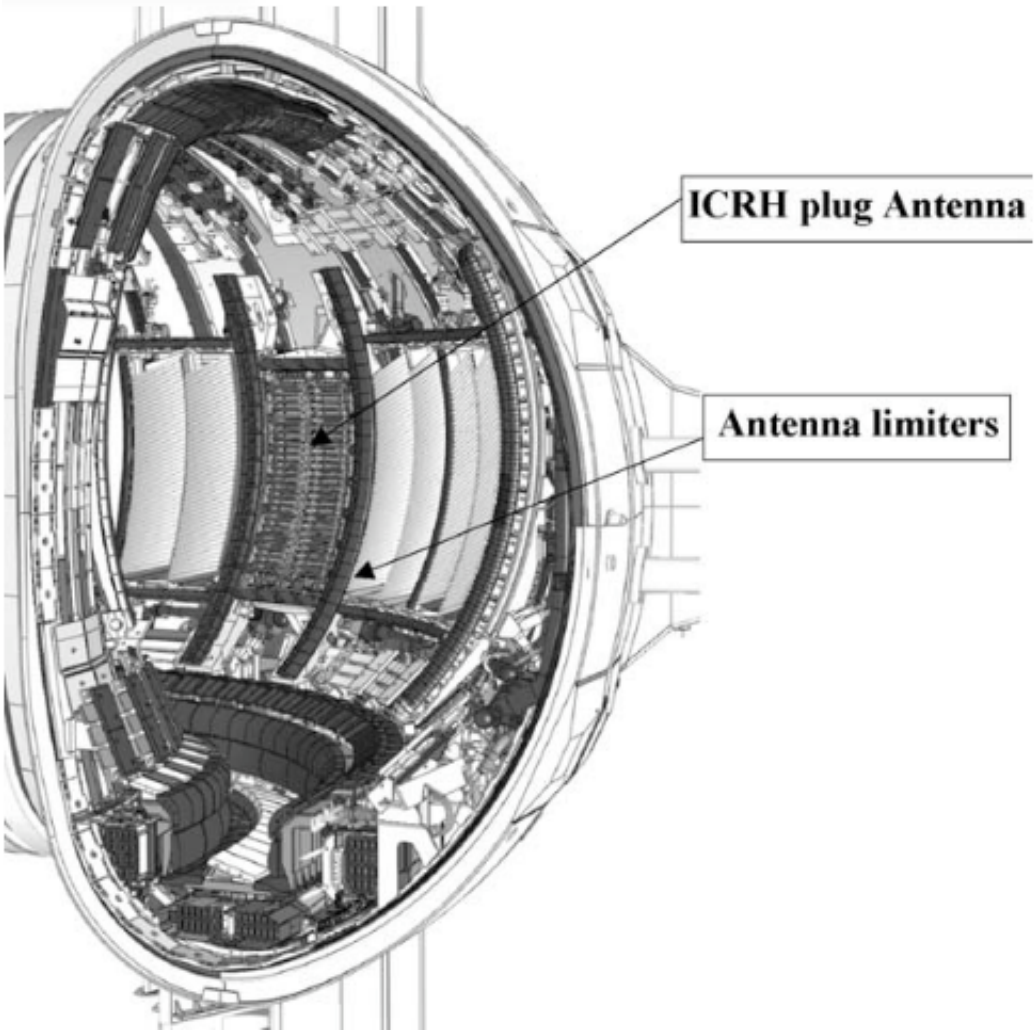

Figure 1.2: JET in-vessel view of the ICRH antenna and limiters. Figure from [2].

the limiters is to allow for proper protection of the antenna from the plasma current. There are two sets of limiters boxing the antenna a cross limiter above and below the antenna and the more common poloidal limiter set. In WEST, Fig 1.3, only poloidal limiters made of Tungsten W are deployed. Limiters near ICRH antennas have been shown to be magnetically connected to the ICRH antenna [15]. This couples the local impurity sputtering at the limiters to the operating regime of the ICRH device. This feature has enabled the deployment of spectroscopy devices with lines of sight distributed on the limiters as a method of measuring the enhancement in impurity sputtering due to the ICRH usage [15]. A set of spectrometers are often deployed with the lines of sight vertically covering the whole limiter. ASDEX Upgrade experiments have shown that the ICRF antenna limiters are the primary impurity source in their device [16]. The connection between limiters and antennas is further discussed in Sec 1.3.

The second component of the ICRH system that comes in contact with the plasma is the antenna. The antenna is divided into separate current straps held together in an antenna box. Typically the antennas contain 2-4 current straps with a noval 3 strap antenna being designed and tested currently [17]. Fig 1.4 shows a two strap antenna with two quarters of the FS shown. The PFC of the antenna is the FS. The FS is an armored series of beryllium bars placed in front of the antenna straps. The engulfing box contains the whole antenna structure. A single antenna strap defined as two stacked FS quarter one over each other. The FS antenna quarters are biased at the same phase.

For proper coupling and injection of the RF waves, the FS needs to be in close proximity to the plasma edge. The proximity to the plasma edge and the high voltage bias at the FS leads to the emergence of RF plasma sheaths. The presence of RF sheaths is associated with an enhanced plasma material

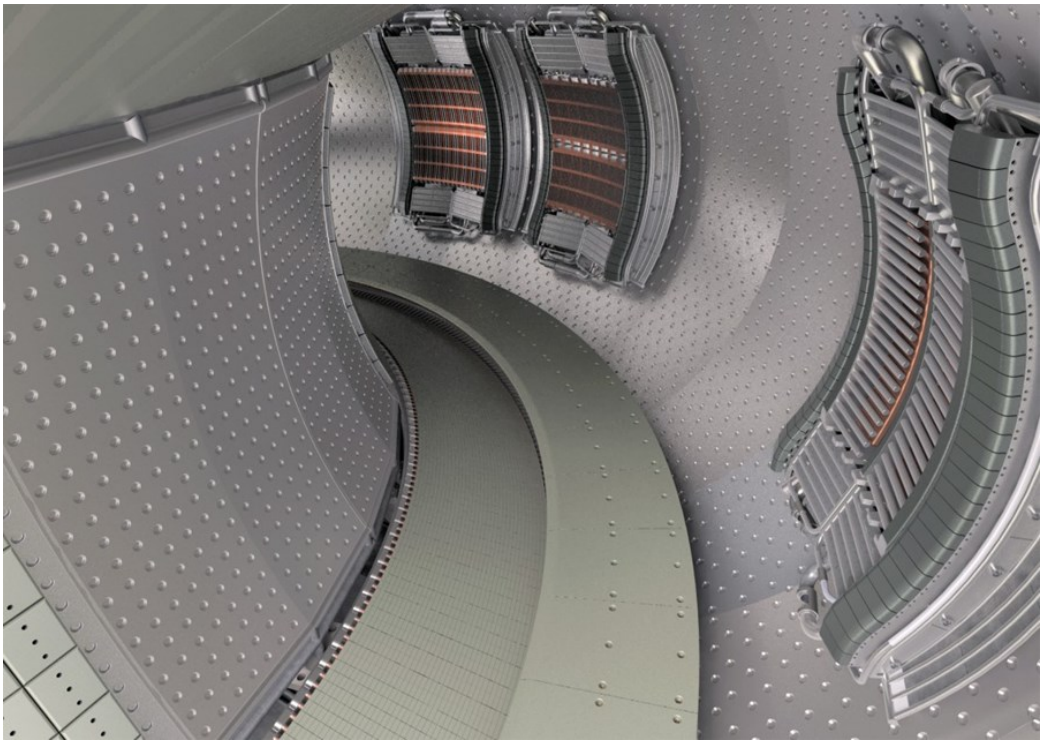

Figure 1.3: WEST in-vessel view of the whole PFC. PFC coated with W including poloidal limiters surrounding antenna structure.

interaction (PMI) at the point of contact with the plasma facing components (PFC) [18, 19, 8].

1.3 Plasma Sheaths in magnetized Radio-Frequency conditions

Plasma sheaths are regions of space where there exists a net positive charge in the domain of question. This net positive charge is a result of the difference in ion an electron mobilities. As the electrons escape the plasma to the walls they create a net negative charge on the plasma facing component (PFC) which is balanced out by the net positive charge in the plasma sheath domain.

Plasma sheaths are a buffer domain between the net neutral PFC and the

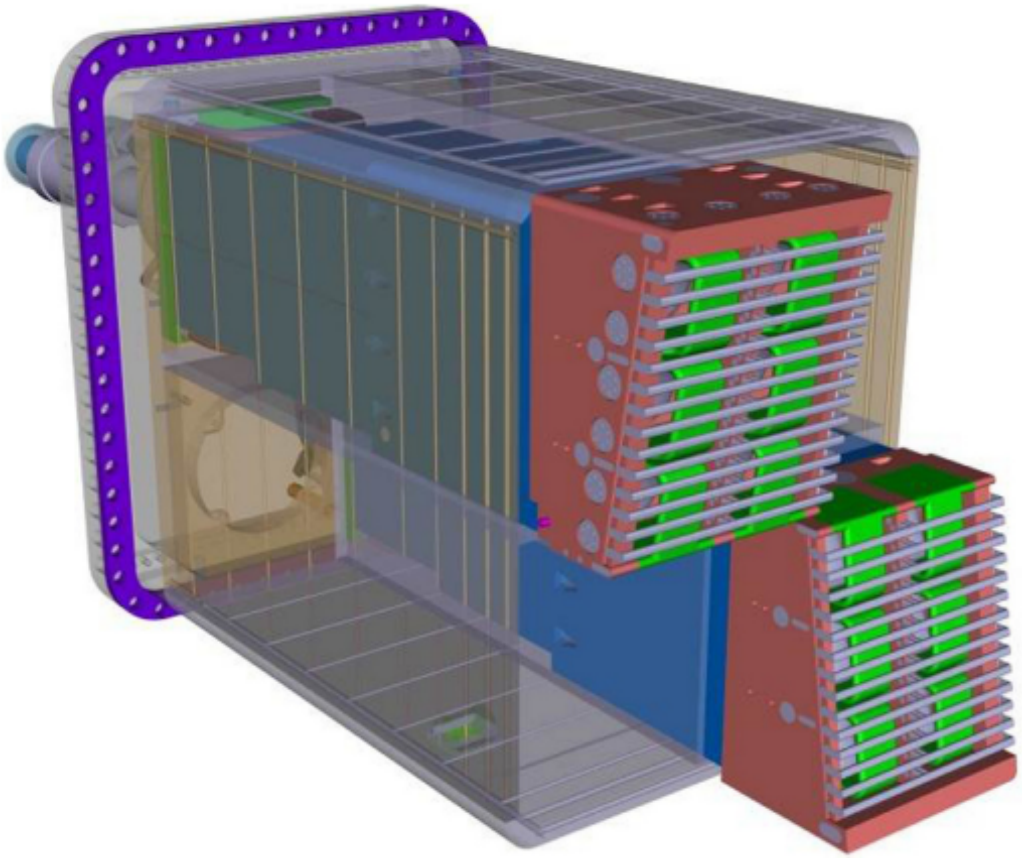

Figure 1.4: View of the front antenna, with two quarter of the FS. Antenna FS made of Be tiles. Fig from [3]

negative PFC. Additionally, the plasma sheaths is the plasma domain were all the PMI takes place. A steep potential gradient exists between the upstream plasma and the negative PFC. The resulting electric field accelerates the plasma ions in the direction of the PFC. Accelerated ions bombard the PFC at high energies sputtering neutral impurities from the PFC. The neutral impurities diffuse through the plasma sheath into the core of the plasma without interacting with electric or magnetic fields. Sputtering of impurities from the PFC is a major field of fusion research.

RF Sheaths

As good coupling of RF waves requires close proximity to the plasma, there are some regimes in which unwanted interactions of ICRF wave fields with the antenna and/or boundary plasma are observed [20, 21]. Large Radio frequency voltage biases on the PFC drive radio-frequency voltages in the plasma potential creating sheaths with rectified potentials known as RF sheaths [22, 23, 24]. RF sheaths increase the plasma potential relative to the wall, enhancing the energy of ions impacting the surface, and therefore increase sputtering and erosion. Radio frequency sheaths arise from the non-linear current response of the plasma to an applied voltage due to the high electron mobility compared to ions along the total magnetic field. Sheaths exist on a short spatial scale, nominally the Debye scale, which is generally small in fusion-relevant devices compared with RF wavelengths and device-size scale lengths.

The effects of the enhanced PMI include hot spots [25, 26], performance reduction [20, 6] and most importantly enhanced impurity production [27, 28, 17]. The emergence of rectified RF sheaths in magnetized [29, 30] and

demagnetized conditions [31] is a well-understood phenomena with extensive research work performed on the subject.

Recently, experimental work has been focused on enhanced impurity production from the usage of ICRH systems [32, 5, 33, 21]. Evidence from experiments suggested that RF sheaths are mainly driven by RF voltage biases on the FS antenna [22, 23, 24, 34, 35]. Ions in RF sheaths have kinetic energies on the order of hundreds of T_e. At these energies the ion sputtering yield is increased. In addition, unlike in classical sheaths, ion energy-angle distributions (IEAD) change as a function of time during a RF cycle.

Recently, Myra *et al.* [36, 24] and Elias *et al.* [9] developed models that investigate how the plasma and PMI behave in RF sheaths. Elias *et al.* [9] and Myra *et al.* [36, 24] have shown motivating agreement with experimental data. Despite research focus into modeling PMI in RF conditions, an accurate kinetic description of the IEAD has not been attempted. Fluid models produce the overall features of the PMI but lack the detailed description of the IEAD. Elias *et al.* [9] uses a fluid model to provide an IEAD under the assumptions of maxwellian fluid distributions for both the ions and the electrons. Due to the sensitivity of the PMI to IEADs, proper kinetic descriptions of the IEAD at the PFC are needed to model the surface response and impurity sputtering.

1.4 Enhanced impurity sputtering mitigation strategies

Several strategies for the mitigation of the negative effects of RF sheaths have been developed. These strategies have been tested both experimentally and using simulations. This section will be a broad overview of the mitigation strategies and the most notable experiments that evaluated them. While fluid

simulations and experiments evaluating the mitigation strategies have been performed, a clear gap exists in the lack of kinetic RF sheaths simulations that capture the ion dynamics behaviour and provide an accurate description of the ion energy angle distributions.

Antenna Phasing

An antenna box usually houses 2-4 toroidal current straps. The phasing of the voltage bias on the straps relative to the each other is what is referred to as antenna phasing. Typically the antenna straps are phased in a dipole phasing arrangements $[0, \pi, 0, \pi]$ due to the effects observed when all the antenna straps are biased at the same phasing , i.e, a monopole phasing [0, 0, 0, 0] operation. the effects include increased plasma impurity content, hot-spot formation, and arcing [37].

Alcator C-MOD [4] studied the phasing configurations experimentally. Several phasing options for the four strap antenna were investigated $[0, \pi, 0, \pi]$, $[0, 0, \pi, \pi]$, $[0, \pi, \pi, 0]$, $[0, 0, 0, 0]$, $[0, \pi/6, 0, \pi/6]$, $[0, \pi/2, \pi, 3\pi/2]$. Experiments showed that an attenuated RF field was observed with a balanced configuration. Garrett *et. al* [4] preformed electromagnetic simulations modeling the Alcator C-MOD experiments and found similar results reaffirming the experimental results. Fig 1.5 shows a comparison for the parallel electric field between the typical antenna phasing and a balanced phasing. The largest reduction in RF voltages occurs for monopole phasing and pseudo-monopole phasing, which provide the optimum magnetic flux coupling to the plasma.

EAST [5] ran an experimental campaign with a 2 strap antenna and tried three different phasings $(0, 0), (0, \pi/2)$ and $(0, \pi)$. They found that

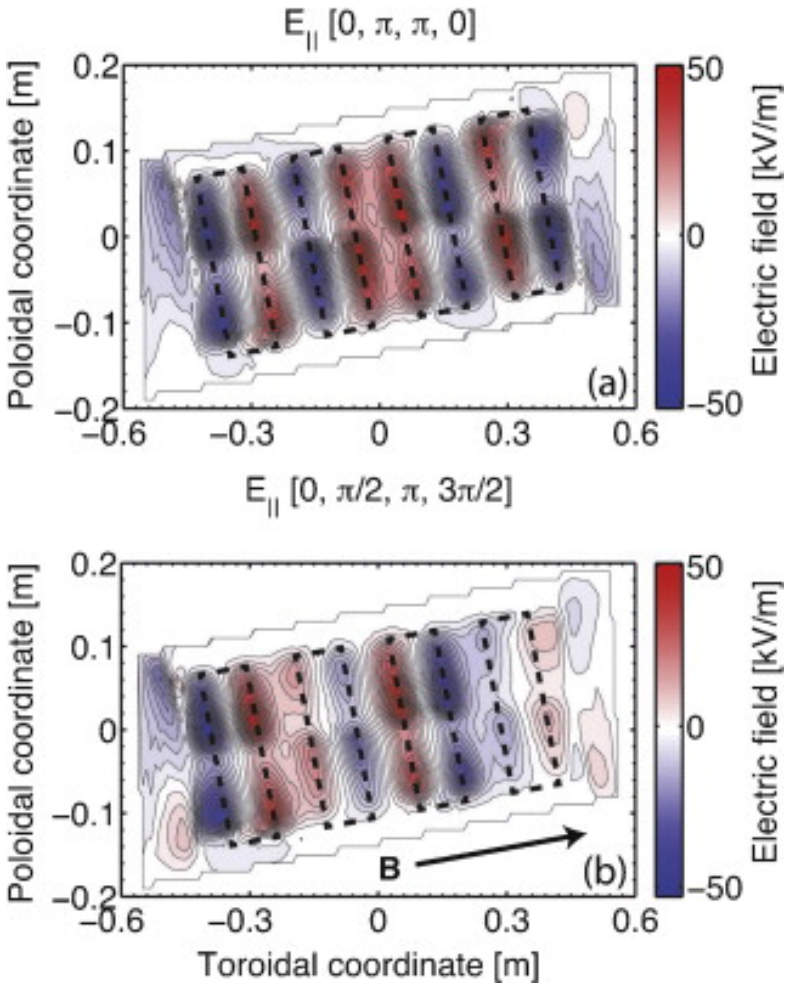

Figure 1.5: Parallel electric field plotted on projections of a flux surface 0.5 cm radially inward of the poloidal antenna limiters for the cold plasma model. Figure from [4]

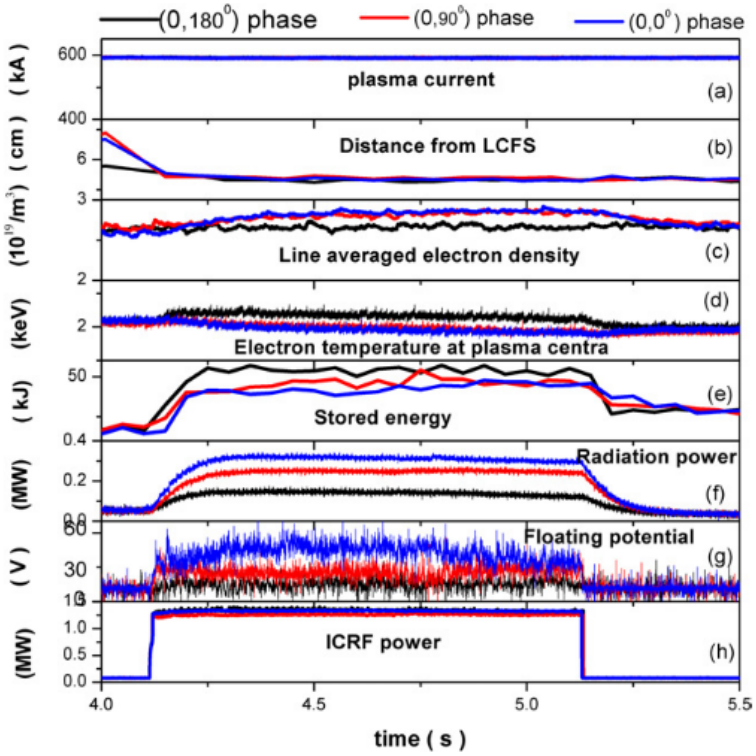

Figure 1.6: Comparison of floating potentials with $(0, 0), (0, \pi/2)$ and $(0, \pi)$ antenna phasing for the same plasma conditions (plasma current, electron density) including the coupled ICRF power. (a) Plasma current, (b) distance from the last closed flux surface to the antenna, (c) line-averaged plasma density, (d) electron temperature at the plasma center measured, (e) stored energy, (f) radiation power at the plasma center, (g) floating potential measured, (h) about 1.2MW ICRF power applied. Figure from [5]

the plasma potential was much lower with $(0, \pi)$ phasing was much lower than $(0, 0)$. Phasing $(0, \pi)$ also had the higher efficiency among the three phasings. Furthermore, the radiated power was also much lower than that with other phases. A comparison of all the experimental profiles is presented in Fig 1.6.

Antenna proximity

The proximity of the antenna to the plasma is one of the main causes leading to the emergence of RF sheaths. Ideally, PFC are to be placed far away from the last closed flux surface. However, coupling requirements require close proximity to the plasma surfaces. Experiments at AUG [15] and EAST [5] found that sputtering yield decreases when the ICRH is shifted away from the plasma, at the expense of a lower coupling resistance. Fig 1.7 provides the main results from the EAST experiment with comparision between a 6.5 cm gap and a 5 cm gap. A considerable increase can be seen in the floating potential, stored energy, radiated power, and electron density and temperature for 5 cm gap. This is mainly due to a higher local plasma density and temperature when the antenna is shifted towards the core. Such an optimization problem between loss of coupling and decrease in sputtered impurities was suggested as a mitigation strategy. AUG found similar results were the decrease in W sputtering yield came at the expense of coupling efficiency when the proximity of the ICRH was increased [15].

Antenna alignment

The angle between the antenna and the magnetic field in the torus is commonly referred to as the antenna alignment. Historically the FS has been

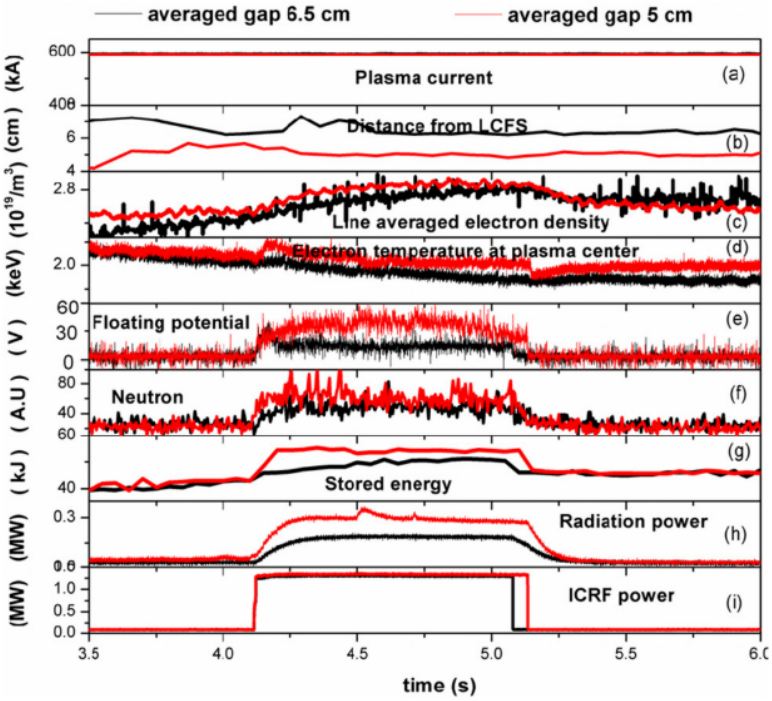

Figure 1.7: Comparison of floating potentials with different gaps (distance from the LCFS). (a) Plasma current, (b) distance from the LCFS to the antenna, (c) line-averaged plasma density at the plasma centre, (d) electron temperature at the plasma centre measured, (e) floating potential measured, (f) neutron flux, (g) stored energy, (h) radiation power at the plasma centre, (i) about 1.2MW ICRF power applied. Figure from [5]

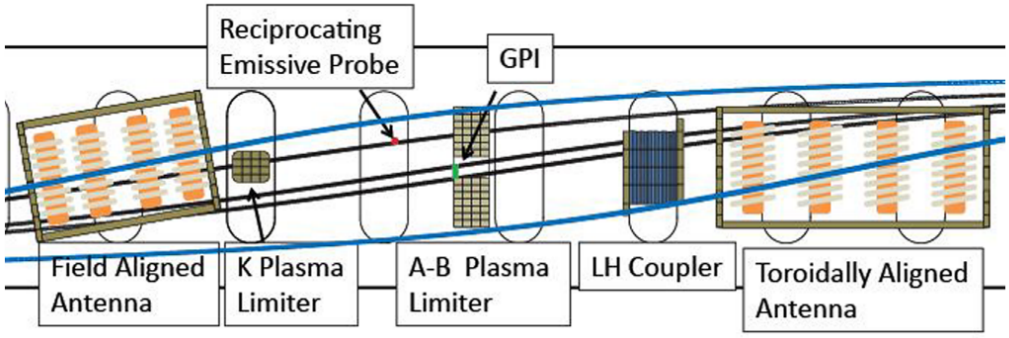

Figure 1.8: Schematic of tokamak wall containing two antenna alignments. The field aligned antenna is aligned to the total field and the conventional, toroidally aligned antenna has only its Faraday screen bars aligned to the total field. Figure from [6].

aligned with the torus of the tokamak. Such a configuration is known as Toroidally Aligned (TA) configuration. A proposed mitigation strategy has been to realign the FS with the magnetic field of the reactor, a model is presented for illustration purposes in Fig 1.9. Such a configuration is known as Field Aligned (FA) configuration. A schematic for comparison between the two alignment configurations is presented in Fig 1.8 to highlight the difference in arrangements.

Alcator C-MOD ran an experimental campaign comparing the two different alignment configurations [6, 4]. Fig 1.10 shows the main results from the spectrometer. FA antennas showed a decrease in the radiated power lost and in the amount of Molybdenum impurity detected while running in H-mode. FA antennas showed a reduction up to a factor of 5 in impurity contamination when compared to TA configurations. Encouraging experimental results were followed by a set of electromagnetic simulations of the C-Mod and ITER RF antennas [38]. Electromagnetic simulations on C-MOD and ITER found that the surface area covered by equivalently strong sheath potentials is visibly reduced for FA configurations when compared to TA configurations.

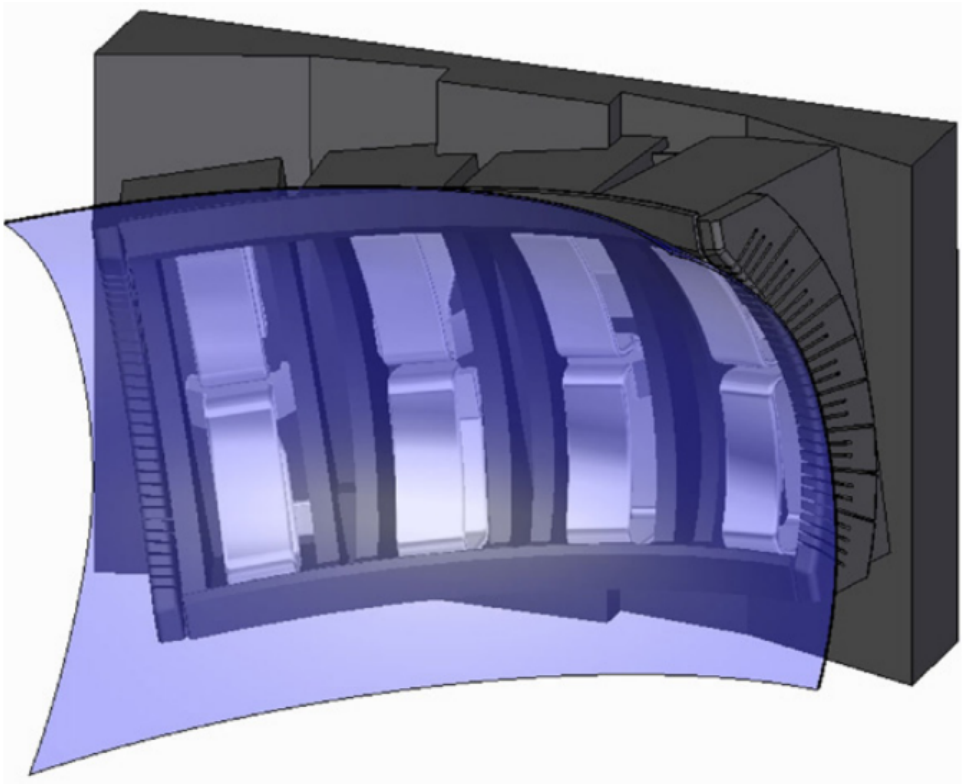

Figure 1.9: Model geometry for new FA antenna. Faraday rods are removed from the image for clarity. Figure from [4].

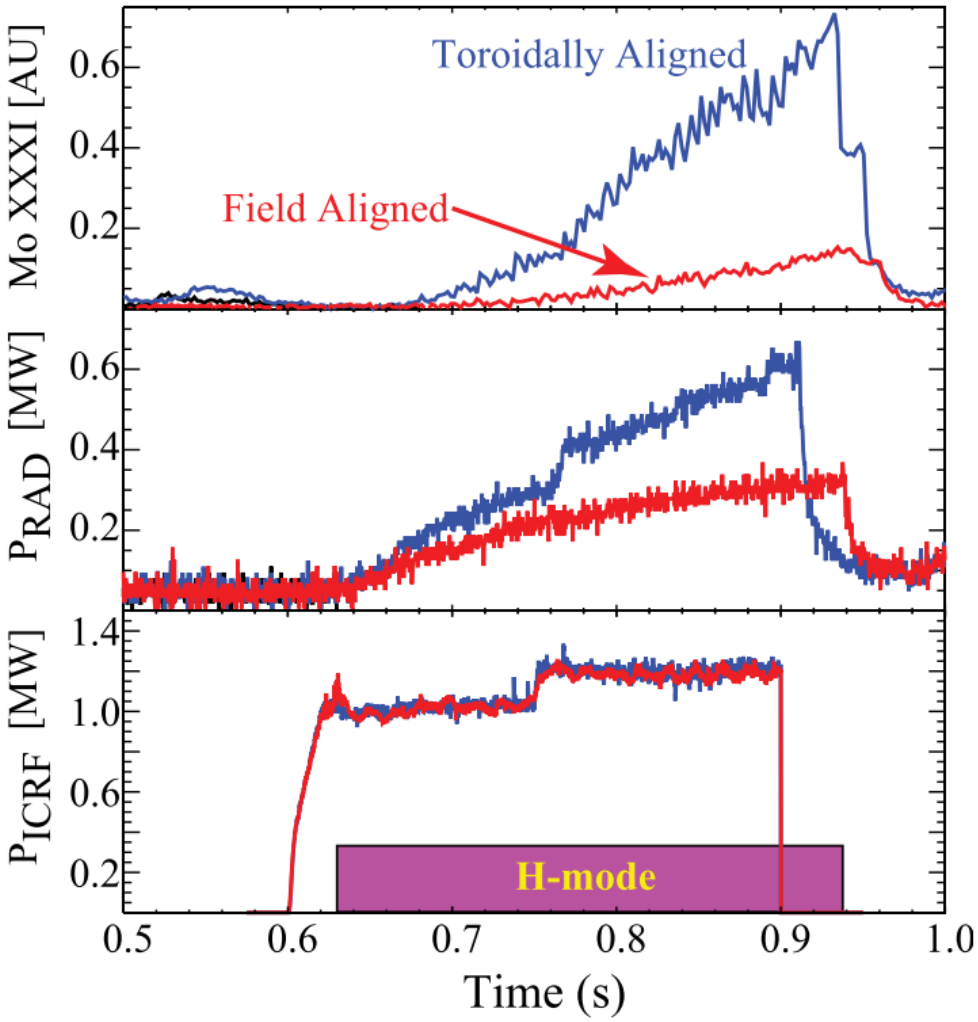

Figure 1.10: In H-mode, the molybdenum contamination and the radiated power are lower for the field aligned antenna than the toroidally aligned antenna. Figure from [6].

RF frequency

ICRH device designed for ITER is designed to operate in a range of RF frequency 40-55MHz. The frequency of operation can play a crucial role in the ion dynamics of the RF sheaths. Elias *et al.* performed a fluid simulation optimizing the RF frequency towards operating with minimal impurity sputtering. Results from fluid simulations indicated a decrease in total sputtering yield correlated with a decrease in RF frequency. However, kinetic effects in ion dynamics were not captured by fluid model.

1.5 Thesis Goal

ICRH devices are crucial to the development of future fusion reactors. However, undesired interactions between ICRH antenna and plasma create RF sheaths with rectified sheath potentials. RF sheaths are associated with enhanced impurity sputtering, parasitic power dissipation, and "hot spots" on antenna launchers and other nearby material surfaces [36, 39]. Impurity mitigation strategies have been developed, tested experimentally and simulated using purely electromagnetic simulations. Current simulation research is EM focused and does not simulate PMI. There exists a gap in the research for the evaluation of mitigation strategies on future devices. Kinetic Ion simulations of PMI are required to evaluate the applicability of the mitigation strategies to future devices.

The objectives of this thesis can be divided into four goals:

- To develop a particle-in-cell simulation code capable of capturing the most relevant RF sheath physics including rectification, charge conservation, ion dynamics, and high ion impact energies.

- Coupling of the PIC model to a model for material emission capturing the relevant plasma material interactions.
- Benchmark and validated kinetic ion model and coupled framework with established codes and relevant experimental results.
- Provide a tool that can analyze and simulate the proposed ICRH RF impurity mitigation strategies in an RF sheath environment using a 1D3V Particle in cell kinetic ion model coupled to a plasma material interactions code.

CHAPTER 2

DEVELOPMENT OF A NEW CHARGE CONSERVATION SCHEME FOR HYBRID PARTICLE-IN-CELLS INCLUDING RF BOUNDARY CONDITIONS

This chapter will be centered around the Particle-In-Cell method used to capture the kinetic description of the plasma particles. The theory behind PIC codes will be discussed. The distinguishing feature of the hybrid Particle-In-Cell (hPIC) code used in this thesis and the motivation behind its development will discussed. Finally this chapter will also discuss the novel charge conservation algorithm develop through the course of this work[40].

2.1 Development of the hybrid Particle-In-Cell method

The classical Particle-In-Cell technique attempts to model the plasma particles using super particles that are tracked throughout the domain. Each super particle represents a set number of plasma particles equivalent to the particles-per-computational particle ratio. Additionally, a mesh field where the super particle charges and current are interpolated upon is imposed. The mesh field points serves as basis points were the poisson equation is solved upon.

Any PIC code can be broken down into two main regimes. The field solver and the particle pusher. The field solver solves Maxwells equation on the provided mesh. The particle solver performs the path tracking and trajectory push of the simulated particles. Representing all the plasma particles, ions and electrons, as super particles enables the code to capture important

kinetic phenomena. However, as ions and electrons fundamentally move at different timescales and spatial scales, simulating the electrons kinetically using super particles adds an additional computational cost and complexity. hPIC simulates the ions as super particles and approximates the electrons using the Boltzmann electron approximation. Such a hybrid framework is ideal for RF sheaths were ion kinetics play the dominant role in PMI.

Boltzmann electrons allow efficient hybrid particle-in-cell (PIC) plasma simulations, applicable to all cases where the electron behavior can be approximated to an inertia-less charged fluid balancing the electrostatic and pressure forces. However, the numerical implementation of Boltzmann electrons requires solving for a non-linear Poisson problem, plus an additional condition enforcing global charge conservation for the calculation of the reference Boltzmann density. In time-dependant problems, such as radio-frequency sheaths or other low-frequency transient phenomena, the correct normalization of the reference Boltzmann density requires a self-consistent numerical scheme.

2.2 A new charge conservation algorithm for Boltzmann electrons

Particle-in-Cell (PIC) simulations using Boltzmann electrons necessarily require enforcing charge conservation to avoid uncontrolled electrostatic oscillations. Without enforcing charge conservation, large unphysical density fluctuations appear in the simulation, triggering strong nonlinear electrostatic waves [41]. Methods have been proposed to damp such oscillations, using both explicit approaches based on filtering [7] and implicit global approaches [42]. Here we describe a new explicit scheme to enforce charge conserva-

tion, in explicit PIC simulations with Boltzmann electrons, that does not require any unphysical ad-hoc filtering. The scheme is particularly suitable to transient problems, such as radio-frequency (RF) plasmas, RF sheaths, and problems with open boundaries, where the ion charge lost across a boundary is of utmost relevance. Furthermore, our scheme is general enough that it naturally applies with minor modifications to the case of multiple ion species, in both current-free and current-carrying conditions. We report the pseudo-code of the algorithm for quick adaptation into existing Particle-in-Cells, and show examples of our implementation in the hPIC [43] Particle-in-Cell (PIC) code.

On ion-transport time scales, the electron behavior can in first approximation be described simply considering a balance between electrostatic forces and pressure forces on an isothermal fluid: $-k_B T_e \nabla n_e + e n_e \nabla \phi \approx 0$, with usual meaning of symbols [44]. Integrating the balance of forces leads to a relation between the electron particle density and the plasma potential in the form of equation 2.1:

$$n_e(\mathbf{x}) = n_0 \exp(e\phi(\mathbf{x})/k_B T_e), \tag{2.1}$$

where n_0 is the reference electron density corresponding to $\phi = 0$. Boltzmann electrons hold an advantage in terms of computational cost over the alternative approximations used in PIC simulations. While alternative methods capture the physical phenomena of electron motion to a higher degree of accuracy, the added simulation complexity makes it computationally expensive to run large timescale simulations.

Time advancement schemes calculate unknown time-dependent variables at time $t^{k+1} = t^k + \Delta t$ from known variables at time t^k. Common time

advancement algorithm in PIC codes calculates the ion density n_i^{k+1} using plasma potential ϕ^k. Subsequently, the plasma potential ϕ^{k+1} is solved using the newly calculated ion density n_i^{k+1} and equation 2.1, i.e,;

$$\epsilon_0 \nabla^2 \phi^{k+1}(\mathbf{x}) = -\rho^{k+1}(\mathbf{x}) \tag{2.2}$$

$$= e n_e^{k+1}(\mathbf{x}) - e n_i^{k+1}(\mathbf{x}) \tag{2.3}$$

$$= e n_0^{k+1} \exp(\phi^{k+1}(\mathbf{x})/T_e) - e n_i^{k+1}(\mathbf{x}). \tag{2.4}$$

Equation 2.4 can be solved using Newton-Raphson, or other methods, to calculate the plasma potential for the next iteration. Problems arise when the reference electron density n_0 varies with time as is the case in the presence of a volumetric source/loss, or a boundary flux. A self-consistent numerical scheme to calculate n_0^{k+1} is required to maintain charge conservation. Breaking charge conservation leads to numerical oscillations and simulation divergence.

Cartwright et al. [41] proposed a self consistent numerical scheme for the calculation of the reference Boltzmann electron density n_0 (embedded in $n_e(\mathbf{x})$) from global electron conservation:

$$\frac{\partial N_B}{\partial t} + \iint_S n_e(\mathbf{x})\, \mathbf{u_e}(\mathbf{x})\, dx = G - L, \tag{2.5}$$

where G and L are volumetric ionization and recombination rate of the Boltzmann electrons, respectively. The surface, S, bounds the plasma domain enclosing a total number of Boltzmann electrons N_B. However, the numerical scheme, developed based on equation 2.5, leads to numerical difficulties when simulating time-evolving plasma sheaths. In particular, simulating the transient behaviour of plasma formation using Cartwright algorithm for n_0

in not self-consistent with Φ but lags one time step behind the Newton-Raphson Loop [42]. Such numerical oscillations limit the implementation of the Boltzmann electron model in transient plasma simulations.

Hagelaar [7] improved the global electron charge conservation from equation 2.5 by means of a second-order under-relaxed filter. Under-relaxing the plasma potential allows critical damping of numerical oscillations and enables fast convergence of the potential on timescales of ion transport. However, Hagelaar's under-relaxation fails when simulating oscillatory plasma conditions, such as time-dependent RF voltage wall biases.

In this section we describe a new numerical scheme for the calculation of the reference Boltzmann electron density based on global net charge conservation. The scheme enables the simulation of transient plasma sheaths without any unphysical ad-hoc filtering or large numerical oscillations. In section 2.2 we provide a derivation for the physical scheme proposed. Sections 2.2 and Sections 2.2 discuss the proposed explicit and implicit implementation algorithms. All variables are presented from this point forward are in SI units with the exception of temperatures T_i, T_e, presented in eV.

Physical Derivation

We derive our scheme starting from the Ampere-Maxwell equation [45] in differential form,

$$\nabla \times \mathbf{B} = \mu_0 \mathbf{J} + \epsilon_0 \mu_0 \frac{\partial \mathbf{E}}{\partial t} \tag{2.6}$$

As usual, local charge conservation is obtained by taking the divergence of equation 2.6 and calling the displacement current as $\mathbf{J_D} = \epsilon_0 \frac{\partial \mathbf{E}}{\partial t}$

$$\nabla \cdot (\nabla \times \mathbf{B}) = \mu_0 \nabla \cdot \mathbf{J} + \mu_0 \nabla \cdot \left(\epsilon_0 \frac{\partial \mathbf{E}}{\partial t} \right) \tag{2.7}$$

$$0 = \nabla \cdot \mathbf{J} + \nabla \cdot \mathbf{J}_D, \tag{2.8}$$

where the conduction current $\mathbf{J} = \mathbf{J}_i + \mathbf{J}_e$ is the sum of the contributions from the ion current $\mathbf{J}_i$ and the electron current $\mathbf{J}_e$. Equation 2.8 can equivalently be expressed as

$$\nabla \cdot (\mathbf{J}_e + \mathbf{J}_i + \mathbf{J}_D) = 0 \tag{2.9}$$

or using its integral form,

$$\int_V \nabla \cdot (\mathbf{J}_e + \mathbf{J}_i + \mathbf{J}_D) dV = 0 \tag{2.10}$$

In the presence of volumetric source G and loss L terms, equation 2.10 becomes

$$\int_V \nabla \cdot (\mathbf{J}_e + \mathbf{J}_i + \mathbf{J}_D) dV = G - L \tag{2.11}$$

The Boltzmann electron model described in equation 2.1 implicitly assumes the electron distribution is at a Maxwellian thermal equilibrium. For a Maxwellian thermal distribution , with a mean thermal electron velocity $\mathbf{u_e} = \sqrt{\frac{8K_bT_e}{\pi m_e}}$, the current density at the location $\mathbf{x}$ can be expressed as [44]:

$$\mathbf{J}_e(\mathbf{x}) = -e\mathbf{\Gamma}_e(\mathbf{x}) = -en_0\mathbf{u}_e \exp(e\Phi(\mathbf{x})/T_e) \tag{2.12}$$

By substituting Equation 2.12 into Equation 2.11 and solving for n_0, immediately yields an expression for the reference Boltzmann electron density n_0

$$n_0 = \frac{\int_V \nabla \cdot (\mathbf{J}_i + \mathbf{J}_D) dV - G + L}{\int_V \nabla \cdot e\mathbf{u}_e \exp(e\Phi(\mathbf{x})/T_e) dV} \tag{2.13}$$

Equation 2.13 can be directly used to enforce global charge conservation in explicit PIC schemes with Boltzmann electrons. An example algorithm is discussed hereafter.

Explicit implementation algorithm

A simple explicit algorithm implementing Equation 2.13 for updating the Boltzmann density n_0 from time step t^k to time step t^{k+1} is as follows.

1. Calculate ion density n_i^{k+1} using the plasma potential ϕ^k at the previous time step, using the classical explicit PIC scheme;

2. Calculate reference Boltzmann electron density at n_0^{k+1} at time step t^{k+1} using equation 2.13 and boundary conditions for ϕ^{k+1};

$$n_0^{k+1} = \frac{\int_V \nabla \cdot (\mathbf{J}_i^{k+1} + \mathbf{J}_D^k) dV - G^{k+1} + L^{k+1}}{\int_V \nabla \cdot e\mathbf{u_e} \exp(e\phi^{k+1}/T_e) dV} \tag{2.14}$$

3. Solve the plasma potential ϕ^{k+1} using ion density n_i^{k+1}, boundary conditions for ϕ^{k+1}, the Poisson equation (Eq. 2.4) and reference Boltzmann electron reference density n_0^{k+1}.

The algorithm can be equally applied to plasma domains of arbitrary dimensionality in 1D, 2D or 3D without any loss of accuracy. However, the con-

ventional Courant–Friedrichs–Lewy condition on the time step remains necessary to ensure accuracy on the particle pusher, and to resolve ion-timescale phenomena.

Implicit implementation algorithm

The simulation of RF sheath cases with large RF bias frequency requires an implicit implementation of the algorithm. Such simulations requires implementing Eq. 2.14 implicitly using J_D^{k+1} instead of J_D^k, where steps 2 and 3 in the proposed scheme are iterated over until an appropriate convergence criteria for n_0^{k+1} is met.

Slight modification are proposed to the algorithm for an implicit implementation:

1. Calculate ion density n_i^{k+1} using the plasma potential ϕ^k at the previous time step, using the classical explicit PIC scheme;

2. Calculate reference Boltzmann electron density at n_0^{k+1} at time step t^{k+1} using equation 2.13 and boundary conditions for ϕ^{k+1};

$$n_0^{k+1} = \frac{\int_V \nabla \cdot (\mathbf{J}_i^{k+1} + \mathbf{J}_D^{k+1}) dV - G^{k+1} + L^{k+1}}{\int_V \nabla \cdot e\mathbf{u_e} \exp(e\phi^{k+1}/T_e) dV} \tag{2.15}$$

3. Solve the plasma potential ϕ^{k+1} using ion density n_i^{k+1}, boundary conditions for ϕ^{k+1}, the Poisson equation (Eq. 2.4) and reference Boltzmann electron reference density n_0^{k+1}.

4. Update the displacement current $\mathbf{J}_D^{k+1}$ at the boundaries.

5. Iterate steps 2-4 till convergence.

In the next chapter we apply this algorithm to four test cases, a steady-state plasma sheath, a steady-state plasma sheath with a biased wall, a radio-frequency plasma sheath with a grounded wall and a radio-frequency plasma sheath. The numerical testing cases are intended to verify the algorithms ability to capture relevant physics such as RF sheath rectification, sheath voltage modulation, sheath currents and electrical properties, ion dynamics, and high ion impact energies.

Being local in time, the numerical scheme is expected to yield accurate results when simulating both steady-state and transient conditions. An advantage associated with the scheme presented in this thesis is the ability to capture the ion dynamics and ion energy angle distribution in plasma sheaths and RF sheaths. These abilities will be benchmarked in chapter 3.

CHAPTER 3

BENCHMARKING HPIC FRAMEWORK IN RF CONDITIONS

3.1 Numerical Testing of classical and RF sheaths in hPIC

The numerical charge conservation scheme proposed in chapter 2 was tested on the full-orbit Particle-in-Cell hPIC [43], for the case of a magnetized plasma between two metallic plates. The plasma domain is sketched in Fig. 3.1, where the x axis is the spatial coordinate going from the first plate placed at $x = x_1$ to the second plate at $x = x_2$, and $L = x_2 - x_1$. The particle orbits were integrated in three spatial coordinates and three velocity coordinates, while the electrostatic potential $\phi(x)$ was solved along the single coordinate x. The magnetic field B was kept uniform across the domain, at an angle $\psi = 70°$ with respect to the x axis.

Table 3.1: Plasma parameters used for the numerical tests of charge conservation.

Test	B[T]	ψ	T_i[eV]	T_e[eV]	n[m^{-3}]	$n_0^{k=0}$[m^{-3}]
1-4	1.0	70°	10	10	5×10^{16}	5×10^{16}

All tests were run for kinetic ions (hydrogen) and Boltzmann electrons, using simulation parameters reported in Table 3.1 and numerical discretization parameters reported in Table 3.3. The variations between cases was limited to the wall bias and operation regime. The wall biases for each of the four

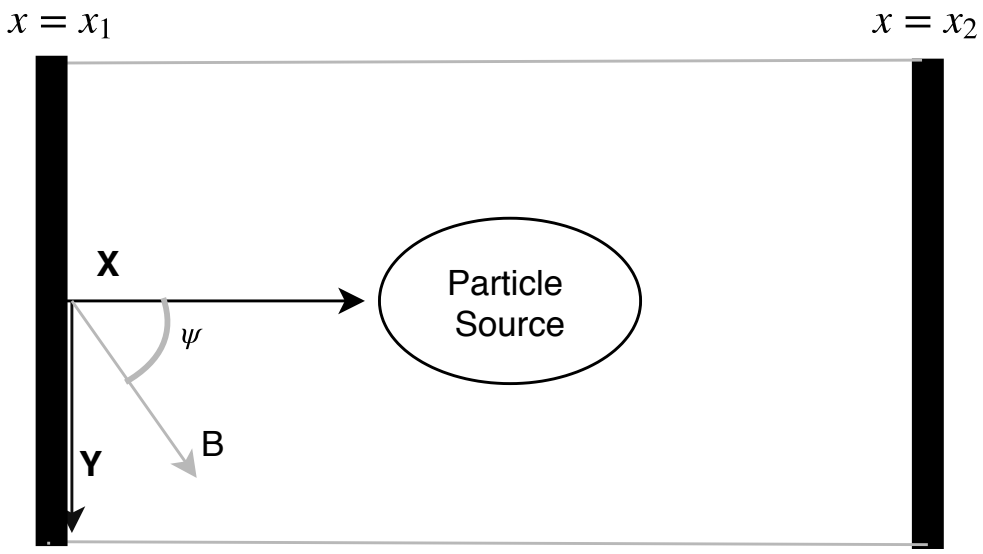

Figure 3.1: Geometrical sketch of symmetric dual plate plasma sheath model with a particle source. Dual plates located at $x = x_1$ and $x = x_2$. Magnetic field angle ψ taken with respect to X axis.

cases is reported in Table 3.2. In all tests, a uniform ionization source S was used to constantly replenish the particle wall losses. The spatial grid and time step (reported in Table 3.3) were set in compliance with the CFL condition for the fastest particles. The total simulation time was set to cover more than one ion acoustic transit time, allowing test cases 1 and 2 to reach steady state and test cases 3 and 4 to reach a periodic state.

Tests 1 and 4 are chosen to highlight the ability of the hPIC code to capture proper charge conservation and voltage rectification and modulation. Preliminary benchmarking will be performed comparing the potential of those cases to the values in literature. Test 2 and 3 are chosen to test the ability of hPIC in capturing high ion impact energies and the ion dynamics and changes in IEAD in transient RF sheath condition.

The first test was for the formation of a thermal plasma sheath between two

Table 3.2: Wall bias parameters used for the numerical tests of charge conservation.

Test	$\phi(x_1)$ [V]	$\phi(x_2)$ [V]	V_{pp} [V]	$\omega[rad/s]$
1	0.0	0.0	0.0	0.0
2	0.0	$\frac{V_{pp}}{2}$	200	0.0
3	0.0	$\frac{V_{pp}}{2}\sin(\omega t+\pi)$	200	1.5×10^8
4	$\frac{V_{pp}}{2}\sin\omega t$	$\frac{V_{pp}}{2}\sin(\omega t+\pi)$	200	1.5×10^8

Table 3.3: Numerical discretization parameters used for the numerical tests of charge conservation.

Test	$L[\lambda_D]$	Cells/λ_D	dt/T_{gyro}	Particles/Cell	Simulation Time[μs]
1-4	200	2	50	5000	1.0

plates electrically grounded and a uniform source. Fig. 3.2 shows the time evolution of the plasma potential $\phi(L/2)$ at the center of the plasma domain (blue curve), and a comparison against the theoretical value (red curve). The same figure also reports a comparison against a scheme previously suggested in literature [7], that was based on a fourth-order under-relaxed filter. The plasma potential converges to the expected theoretical value in both cases, but with different time constants. While the scheme proposed in [7] had an artificial time constant related to the use of the under-relaxed filter, the scheme here proposed based on Eq. 2.13 naturally enforces charge conservation at every time step of the simulation. Numerical oscillations are completely damped out within the first time step of the simulation, exhibiting a convergence to steady state governed only by ion dynamics. At long time scales ($t > 0.15\mu$s) the characteristic behavior toward steady state is

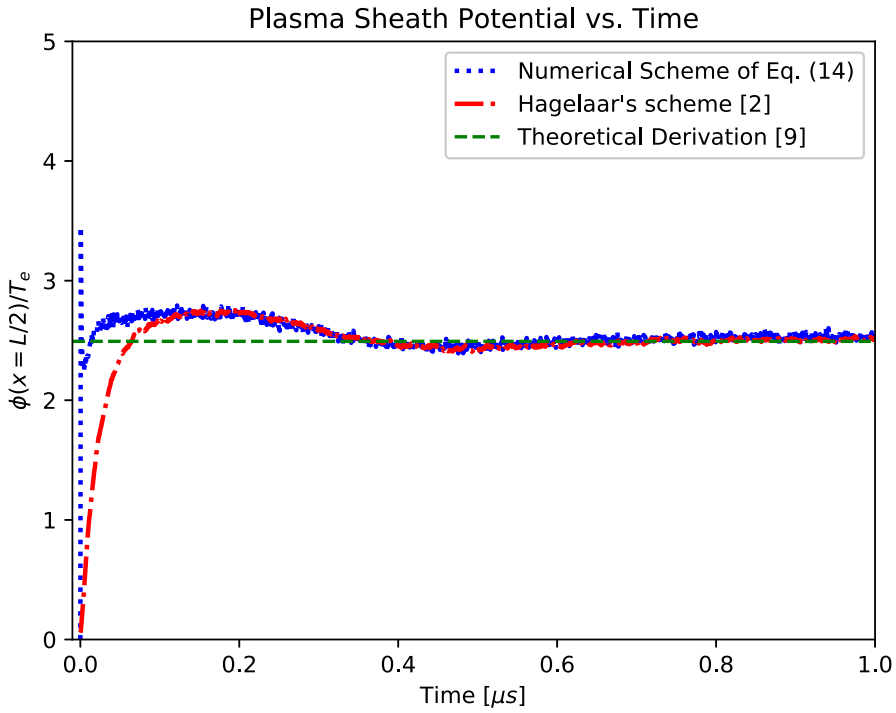

Figure 3.2: The formation and time evolution of the midpoint plasma potential, obtained using Hagelaar scheme [7], equation 2.14, and theoretical derivation [8] ($\phi(x = L/2) = ln(\frac{M_i}{4\pi m_e})^{\frac{1}{2}}$). Numerical overshoot present at the start of simulation due to initial condition choice. Test parameters presented as Test 1 in Tables 3.1- 3.3

independent of the numerical scheme. At time scales of the order of the ion transit time ($t \sim 0.67\mu$s) the phase space relaxes to its steady state distribution, exhibiting the typical supersonic acceleration of the ions toward the walls.

The second test was for the high ion energy impact of a thermal plasma sheath between a grounded plate and a high negative bias. Supplementary plasma potential profile is provided in Fig 3.3. Fig. 3.4 shows the Ion Energy Angle Distribution (IEAD) at the walls of the plasma domain, i.e., impacting the PFC. Two centers to the IEAD are clearly visible, a high energy center (centered around $125eV$) attributed to the right wall biased at $-100V$, and

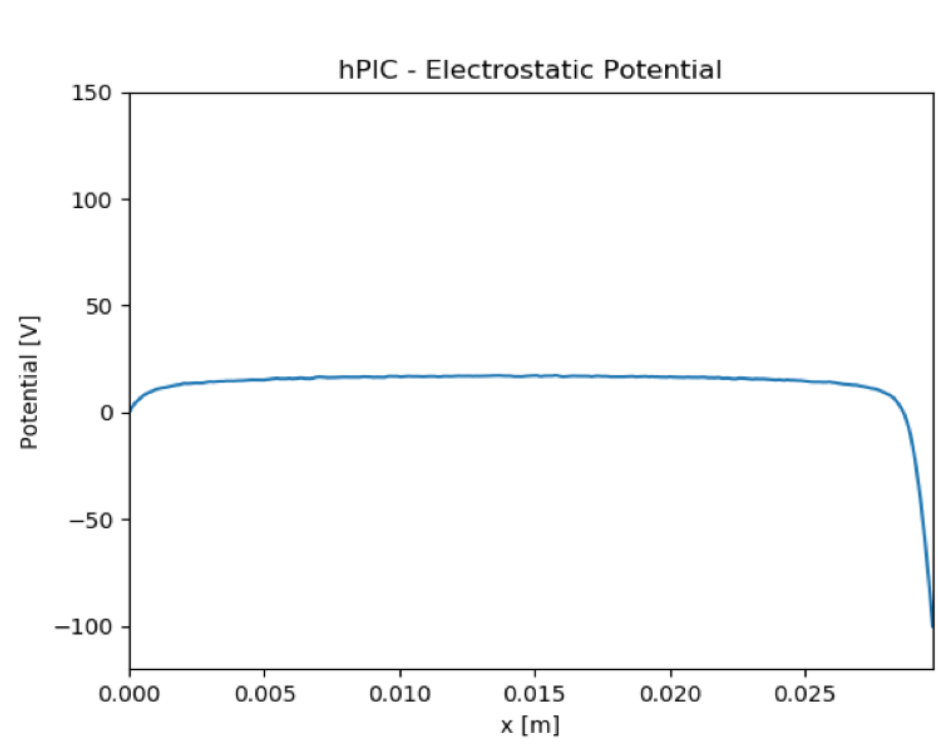

Figure 3.3: Plasma potential profile for test case 2. Test parameters presented as Test 2 in Tables 3.1- 3.3

a low energy distribution center (centered around $30eV$) attributed to the left wall biased at $0V$. Ions impacting the right wall fall through a higher potential gradient hence gaining larger energies. Additionally, the spread in the angular distribution varies considerably when comparing the distributions of the high and low energy centers. This further proves hPIC's abilities in capturing the proper ion dynamics associated with the plasma potential drop. The presence of two clear distinct distributions is a clear indication of hPIC abilities to capture appropriate IEAD for the given plasma sheath profile.

The third test was designed specifically to test hPIC ability in translating the modulation in RF rectification into the IEAD. The plasma sheath is placed between a grounded plate and an oscillating RF voltage bias $\phi(x_2) = (V_{pp}/2)\sin(\omega t)$. Fig. 3.5 shows the Ion Energy Angle Distribution (IEAD)

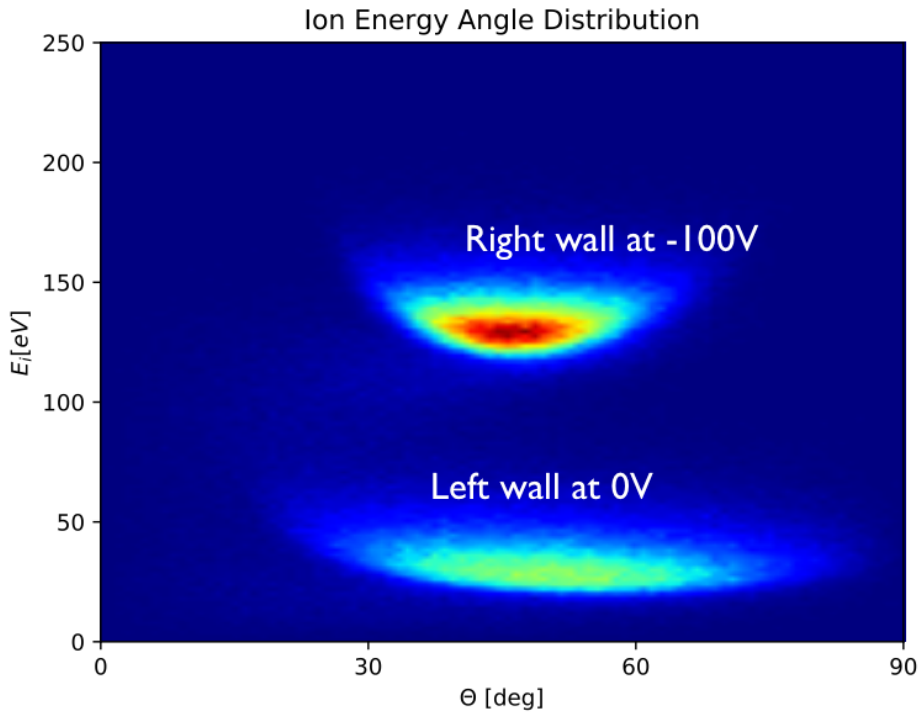

Figure 3.4: IEAD resulting from a thermal plasma sheath between a grounded plate and a high negative bias. IEAD shows two distinct peaks representing the two walls biased at different voltages. Test parameters presented as Test 2 in Tables 3.1 - 3.3

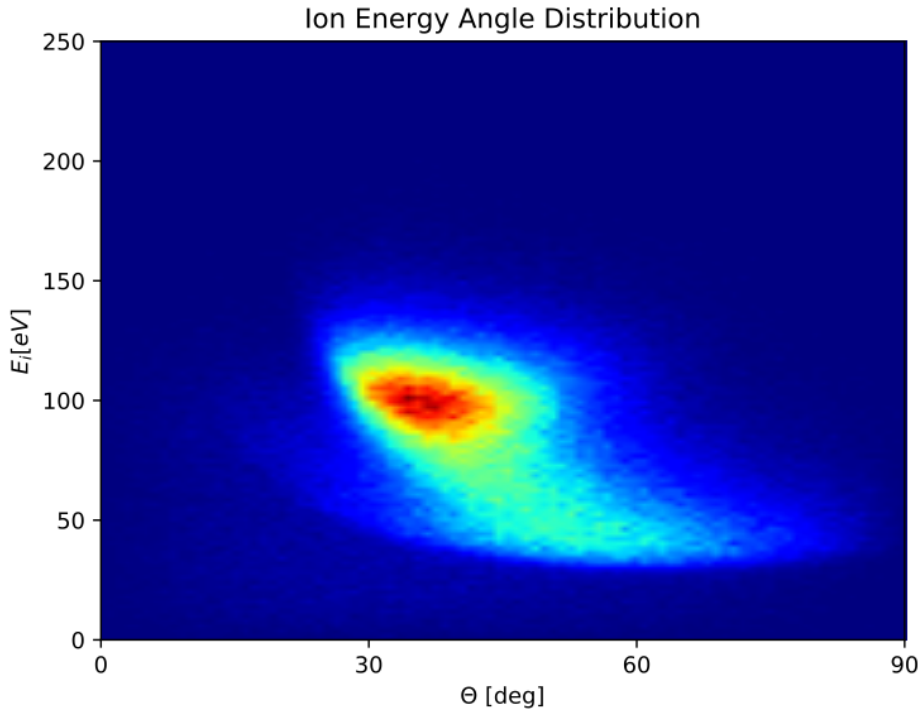

Figure 3.5: IEAD for a plasma sheath is placed between a grounded plate and an oscillating RF voltage bias $\phi(x_2) = (V_{pp}/2)\sin(\omega t)$. IEAD resulting from changing impact energy and angles as a function of RF phase. Test parameters presented as Test 3 in Tables 3.1- 3.3

at the walls of the plasma domain, i,e. impacting the PFC. Compared with Fig. 3.4, the two distributions in the IEAD are now connected and no longer distinct. The ion impact energies and angles change as a function of time oscillating between periods of high RF rectification and high impact energies and low RF rectification and low impact energies. Accumulated over time the IEAD distribution is widely spread over the range of possible impact energies. The ions dynamics at play change over the course of an RF period. hPIC IEAD provide clear evidence of its ability to capture the changes in the RF sheath rectification over time and the effect of this on the subsequent IEAD.

A fourth test case was for the formation of a radio-frequency (RF) plasma

sheath between two metallic plates with anti-symmetric RF drive, $\phi(x_1) = -\phi(x_2) = (V_{pp}/2)\sin(\omega t)$ V, where V_{pp} is the peak-to-peak voltage on the biased walls and ω is the oscillation frequency of the voltage bias. This fourth test case shows the ability to simulate plasma sheaths in transient and time-dependant conditions, an innovative feature of the proposed numerical scheme with respect to the previous explicit scheme based on under-relaxed filtering. Fig. 3.6 shows the time evolution of the plasma potential at the center of the plasma domain $\phi(L/2)$ as calculated by our numerical scheme (blue), and a comparison against the theoretical expected value (orange), as derived in [9, 36]. The simulated plasma potential is in agreement with both amplitude and phase with the theoretical value [9, 36]. In this fourth test the plasma potential does not achieve a constant potential value, but reaches a periodic oscillatory state due to sheath rectification at the RF frequency ω. The scheme here proposed allows to enforce charge conservation within the first time steps of the simulation. The sheath rectification phenomena, typical of RF sheaths, is successfully captured as the plasma oscillates between high and low potential/voltage rectification.

3.2 Benchmarking of RF sheaths time-averaged and time dependent profiles with NoFlu

For the purpose of providing trust in our framework, a benchmarking activity has been performed with a well established code in literature and research field NoFlu[36]. The benchmark chapter is based on a joint activity with the developers of NoFlu[46].

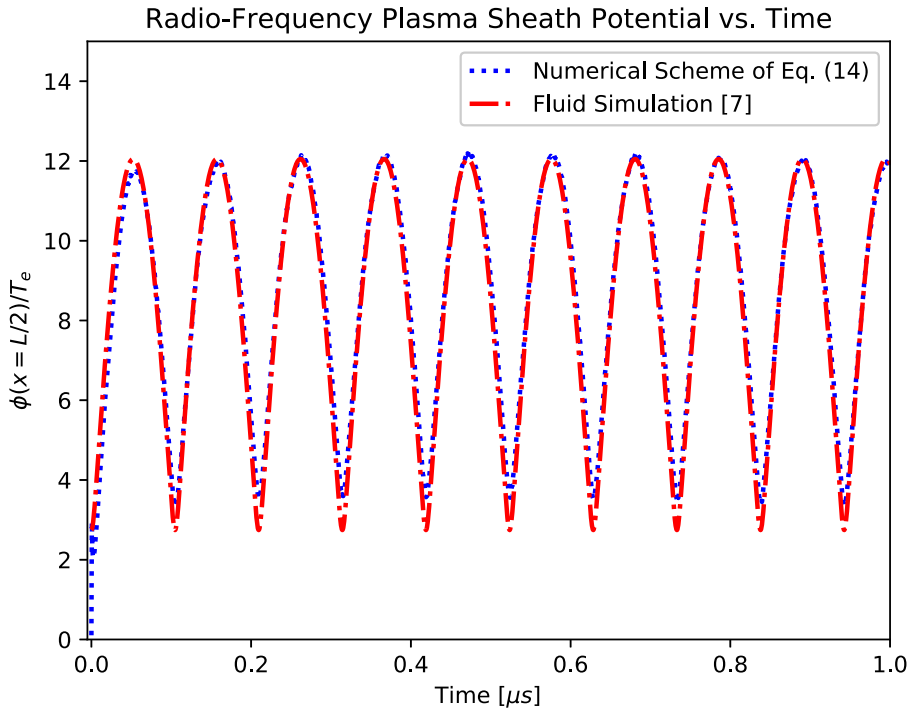

Figure 3.6: The formation and time evolution of the midpoint plasma potential in radio-frequency sheath cases. Obtained using Numerical Scheme proposed in equation 2.14, and theoretical derivation [9] ($\phi(x = L/2) = \ln\left[\frac{\mu}{u_o}\cosh\frac{eV_{pp}\cos\omega t}{2T_e}\right]$). Rectification and periodicity of the midpoint plasma potential are successfully captured. Test parameters presented as Test 4 in Tables 3.1- 3.3

NoFlu

NoFlu nonlinear fluid code solved in one dimensional space domain. NoFlu uses the cold ion approximation and approximates the electrons as isothermal Maxwell-Boltzmann electrons. The fundamental equations of the model are Poisson's equation for the electrostatic potential Φ, the Maxwell-Boltzmann relation for electron density n_e and the electron current density to the sheath J_e, the continuity equation for ion density n_i, and the three components of the ion momentum equation of motion under the Lorentz force. A more detailed description of the model, the assumptions and the equations solved is available in ref [36].

The code is discretized in space and time. NoFlu solves for all time points within a single RF period simultaneously and implicitly. Typical employed NoFlu resolutions for the cases in this dissertation range from 20 to 60 time discretization points per RF period , and 50 spatial discretization points for half the domain. Spatial discretization points translate to approximately two points per Debye length. The NoFlu model employed here is identical to the version described in Ref. [36, 24] except for the addition of a varrying DC current through the domain. Mathematica was used for code implementation with a typical run consuming 1 to 5 min (serial CPU) and requiring 70 MB of RAM[10].

Plasma domain model

The electrical circuitry and spatial geometry of the chosen plasma model are shown in Fig. 3.7. The model is a double-plate model similar to the one commonly used in literature [36, 24]. The model is made of a plasma-filled "capacitor" immersed in an oblique angle magnetic field, driven by anti-

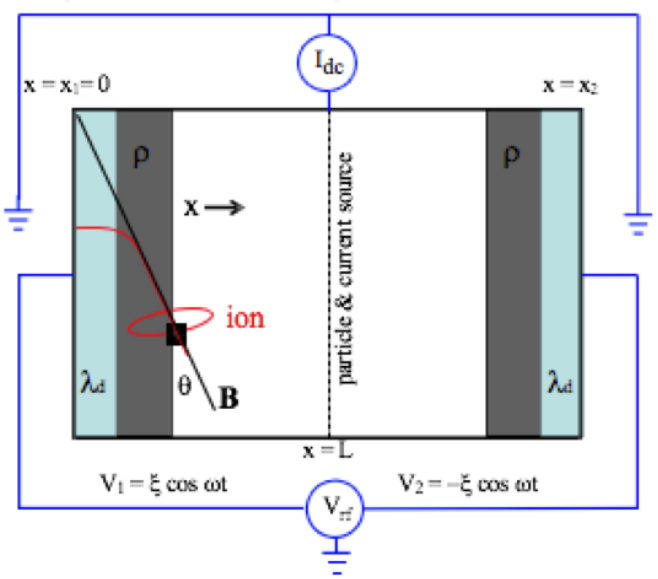

Figure 3.7: Dual plate symmetric RF sheath model. Plasma domain between x_1 and x_2. The PFC are RF driven with a phase difference ofπ and an amplitude ξ. DC current I_{DC} can be drawn through the sheath. Figure adapted from [10].

symmetric RF voltages on each of the two PFC. The model is one dimensional in space in the direction normal to the plates (x direction).

An RF sinusoidal voltage is applied on plates 1 and 2 (the plasma facing components) were $V_1 = V_{rf}cos(\omega t + \pi)$ and $V_2 = V_{rf}cos(\omega t)$. The PFC are RF driven with a phase difference ofπ and an amplitude ξ. The plates are kept grounded at a DC potential of zero. However, DC current I_{DC} can be drawn through the sheath. A scan over an imposed J_{DC} was performed and the effective RF phase averaged potential and electrical quantities were compared. Additionally five cases of varying frequency ω and DC current J_{DC} were chosen for an RF modulated inspection. The constant plasma parameters are defined in Table 3.4 and the varying frequency ω and DC current J_{DC} are provided in Table 3.5 normalized to the plasma frequency ω_{pi} and the ion saturation current J_{isat} for each case.

RF sheath rectification results in the upstream plasma potential Φ_0 to

Table 3.4: Plasma parameters used for the benchmarking cases between hPIC and NoFlu.

Case	B[T]	ψ	T_i[eV]	T_e[eV]	n[m^{-3}]	$V_{rf}[T_e]$
1-5	1.0	0°	10	10	5×10^{16}	10

Table 3.5: Varying case parameters used for the benchmarking cases between hPIC and NoFlu.

Case	$\omega[\omega_{pi}]$	$J_{DC}[J_{isat}]$
1	0.5	-3.13
2	0.5	0.90
3	0.5	0.00
4	2.0	0.00
5	9.0	0.00

reaching values on the order of V_{rf} where $eV_{rf} >> 3T_e$. The upstream plasma potential, modulated in time and averaged over an RF phase was chosen as the main target of the benchmarking activity. Another quantity of interest in the benchmarking activity is the sheath electrical property of admittance y. Admittance y is defined as a normalized ratio of the RF current density flowing through the sheath at frequency ω to the RF voltage across the sheath. As the admittance parameter $y = 1/z$, where z is the impedance, is an additive of the ion, electron and displacement currents it represents an effective comparison parameter quantifying the electrical properties of a complete RF phase. Additionally, detailed comparison of the ion, electron and displacement currents modulated over an RF period was also performed to provide further insight into the cases.

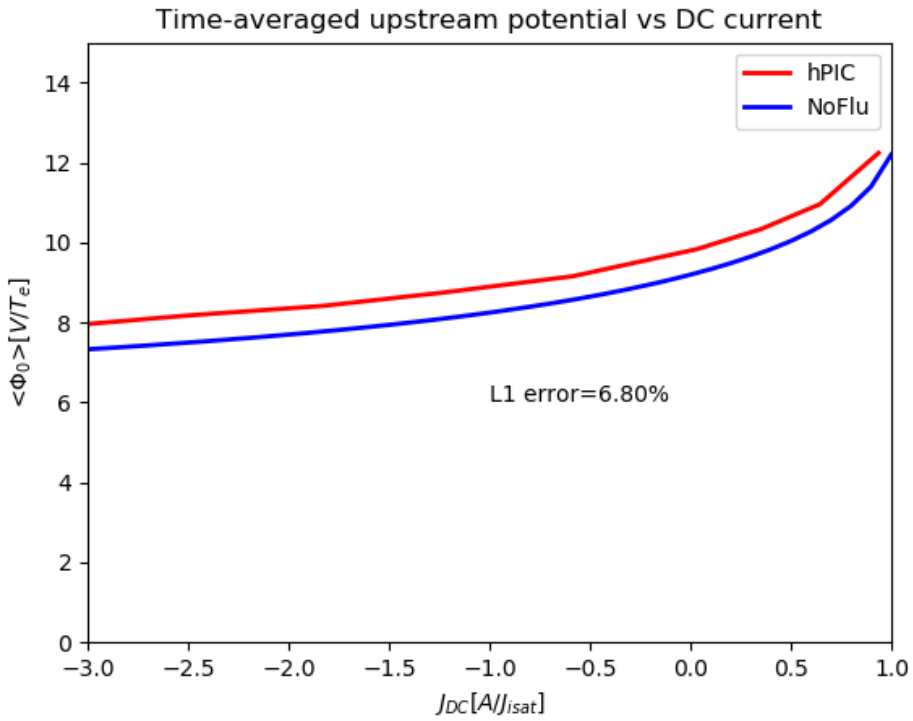

Figure 3.8: Time average upstream plasma potential Φ_0 vs J_{DC}. Simulation parameters give in Table 3.4 and $\omega = 2.5\omega_{pi}$. Data adapted from [10].

Case 0

The start of the benchmarking activity was performed by setting $\omega = 2.5\omega_{pi}$ and scanning over the DC current J_{DC} through the sheath. Consequently, this case is for a moderately high frequency sheath and a high RF voltage. Time averaged quantities of the averaged upstream plasma potential $\langle\Phi_0\rangle$ and the sheath admittance y were calculated. $\langle\Phi_0\rangle$ provides a measure of the sheath rectification phenomena and y quantifies the ion dynamic behavior.

Fig. 3.8 compares the output $\langle\Phi_0\rangle$ of the two codes. Good agreement can be seen between the two codes, quantified by an L1 norm difference of 6.80%. As J_{DC} increases towards more positive values, the upstream potential difference between the plasma and the plate, $\langle\Phi_0\rangle$, increases. This is as expected as larger $\langle\Phi_0\rangle$ confines more electrons in the plasma, decreasing the electron

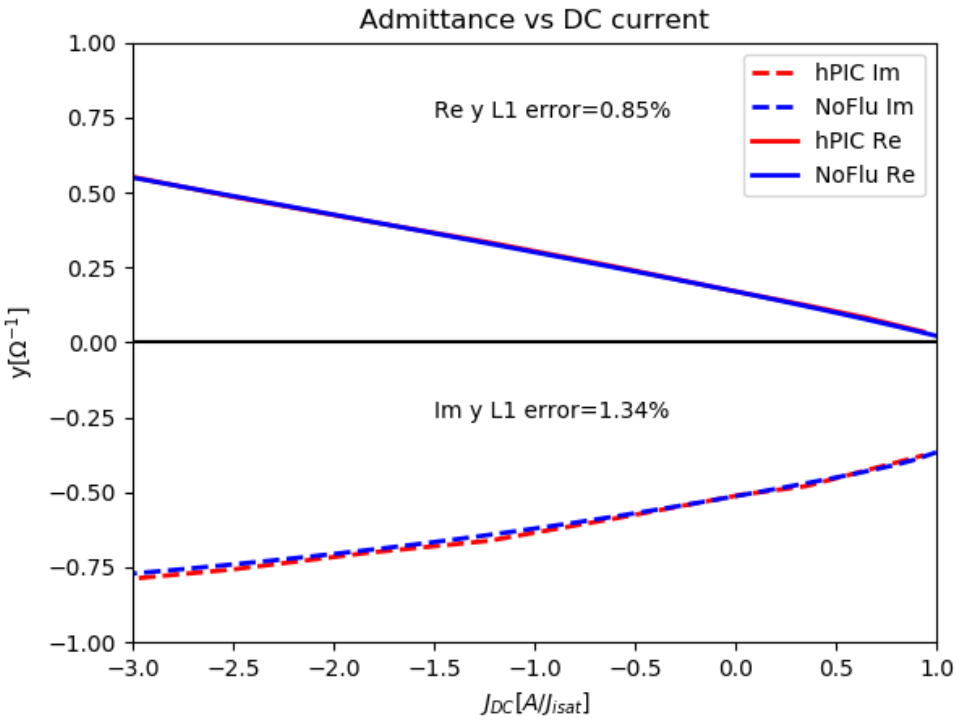

Figure 3.9: RF phase effective admittance y vs J_{DC}. Simulation parameters give in Table 3.4 and $\omega = 2.5\omega_{pi}$. Data adapted from [10].

particle flow to the plate, and thereby increasing the net J_{DC} to the plate. Both codes capture the relation between J_{DC} and $\langle\Phi_0\rangle$. There is a small offset between the hPIC results and the NoFlu results. The offset has been shown to be from differences in the volumetric particle source presheath models in the two codes [10], not an RF specific effect.

Fig. 3.9 compares the output y of the two codes. The admittance y is broken down into Real and Imaginary parts. Good agreement can be seen between the two codes, quantified by an L1 norm difference of 0.85% for the Real part and 1.34% for the Imaginary part . As J_{DC} increases towards more positive values, the magnitudes of both the real and imaginary parts of y decrease. The real part of y is primarily controlled by the electron current, which being suppressed at larger J_{DC}, results in reducing Re y.

The imaginary part of y primarily comes from the displacement current, i.e. sheath capacitance. At J_{DC} increases, and $\langle\Phi_0\rangle$ is larger, the sheath width broadens, reducing the capacitive current. Finally, the agreement between hPIC and NoFlu for y is excellent, which suggests that the time-dependent current waveforms from the two codes should also agree well. This is to be examined in the following cases.

Case 1

Fig. 3.10 compares the output $\langle\Phi_0\rangle$ of the two codes for case 1. Electrical and plasma parameters presented in Table 3.5 and Table 3.4 respectively. Good agreement can be seen between the two codes, quantified by an L1 norm difference of 7.74%. Such an offset, while still an excellent agreement, will be discussed in sec 3.2.

Fig. 3.11 compares the current waveforms at the left wall of the two codes for case 1. Electrical and plasma parameters presented in Table 3.5 and Table 3.4 respectively. Agreement on waveforms provides a crucial benchmarking step as they encompass the plasma dynamics, particle fluxes, electrical properties, and displacement current. Excellent agreement can be seen between the two codes with a maximum L1 norm difference of 2.11% for the displacement current. L1 norms difference for the current waveforms has been quantified and shown in Fig. 3.11.

Case 2

Fig. 3.12 compares the output $\langle\Phi_0\rangle$ of the two codes for case 2. Electrical and plasma parameters presented in Table 3.5 and Table 3.4 respectively. Good agreement can be seen between the two codes, quantified by an L1

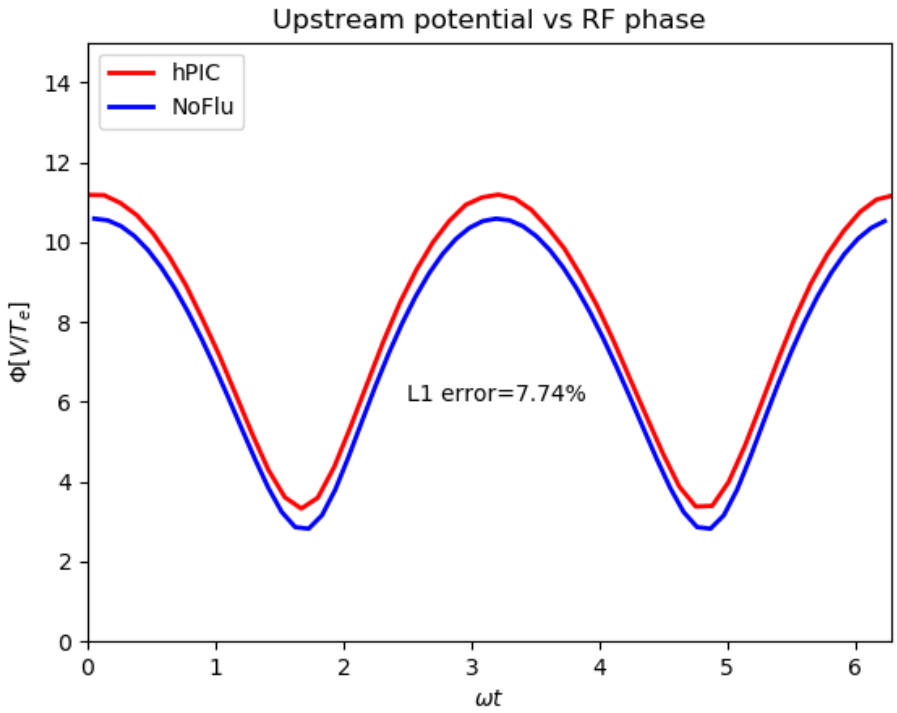

Figure 3.10: Time resolved upstream potential Φ_0. Case 1 electrical and plasma parameters presented in Table 3.5 and Table 3.4 respectively. Data adapted from [10].

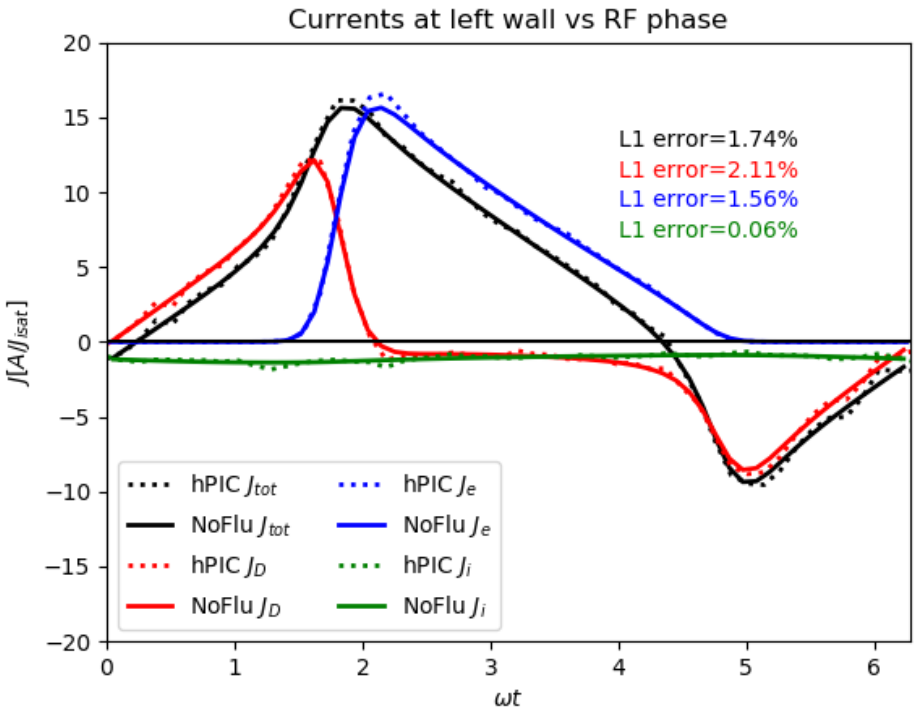

Figure 3.11: Ion J_i, Electron J_e, Displacement J_D and Total current J_{tot} waveforms at the left PFC. Case 1 electrical and plasma parameters presented in Table 3.5 and Table 3.4 respectively. Data adapted from [10].

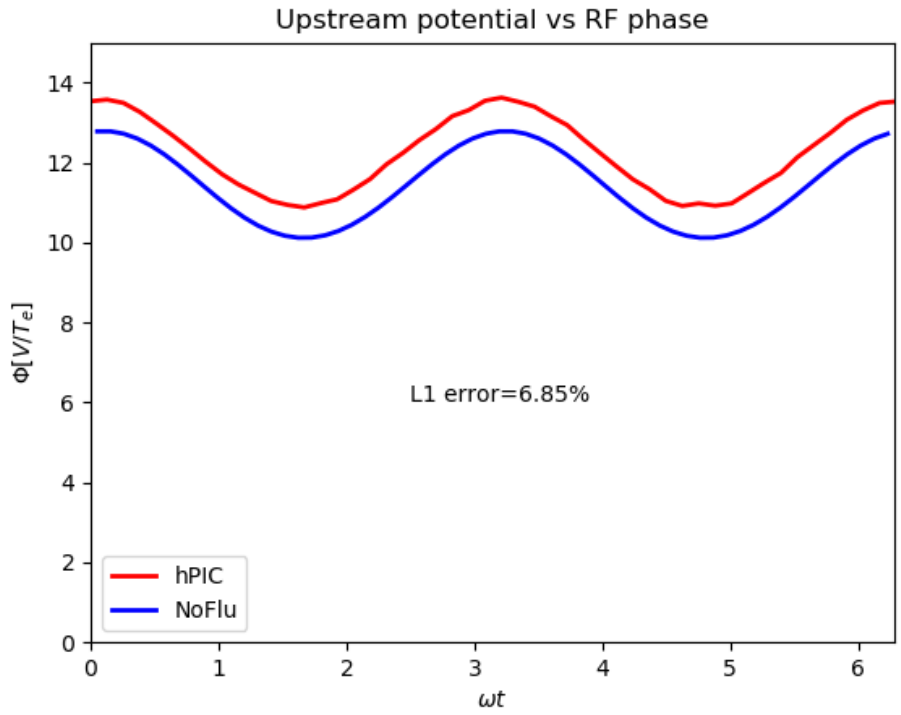

Figure 3.12: Time resolved upstream potential Φ_0. Case 2 electrical and plasma parameters presented in Table 3.5 and Table 3.4 respectively. Data adapted from [10].

norm difference of 6.85%. Such an offset, while still an excellent agreement, will be discussed in sec 3.2.

Fig. 3.13 compares the current waveforms at the left wall of the two codes for case 2. Electrical and plasma parameters presented in Table 3.5 and Table 3.4 respectively. Agreement on waveforms provides a crucial benchmarking step as they encompass the plasma dynamics, particle fluxes, electrical properties, and displacement current. Excellent agreement can be seen between the two codes with an L1 norm difference for total current J_{tot} of 2.13%. L1 norms difference for the current waveforms has been quantified and shown in Fig. 3.13. However, the electron current J_e L1 error stands out as the value is an order of magnitude higher at 17.17%. However, the electron current is small and does not play a role physically in comparison to

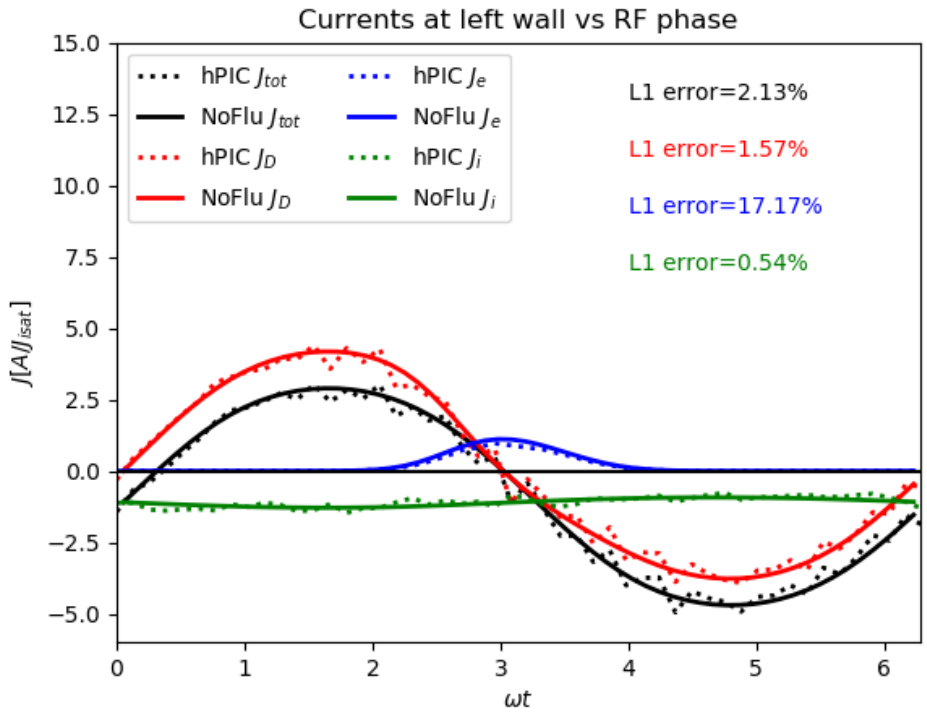

Figure 3.13: Ion J_i, Electron J_e, Displacement J_D and Total current J_{tot} waveforms at the left PFC. Case 2 electrical and plasma parameters presented in Table 3.5 and Table 3.4 respectively. Data adapted from [10].

the total current. Case 2 with a $J_{DC} = 0.9$ has a larger PIC noise evident in Fig. 3.13. The noise is related to approaching the physical singularity that would occur if one draws all the available upstream ion current i.e. the ion saturation current or $J_{DC} = 1.0$. This increases the sensitivity of the system and the numerical noise from the charge conservation algorithm.

Case 3

Fig. 3.14 compares the output $\langle \Phi_0 \rangle$ of the two codes for case 3. Electrical and plasma parameters presented in Table 3.5 and Table 3.4 respectively. Good agreement can be seen between the two codes, quantified by an L1 norm difference of 6.06%. Such an offset, while still an excellent agreement,

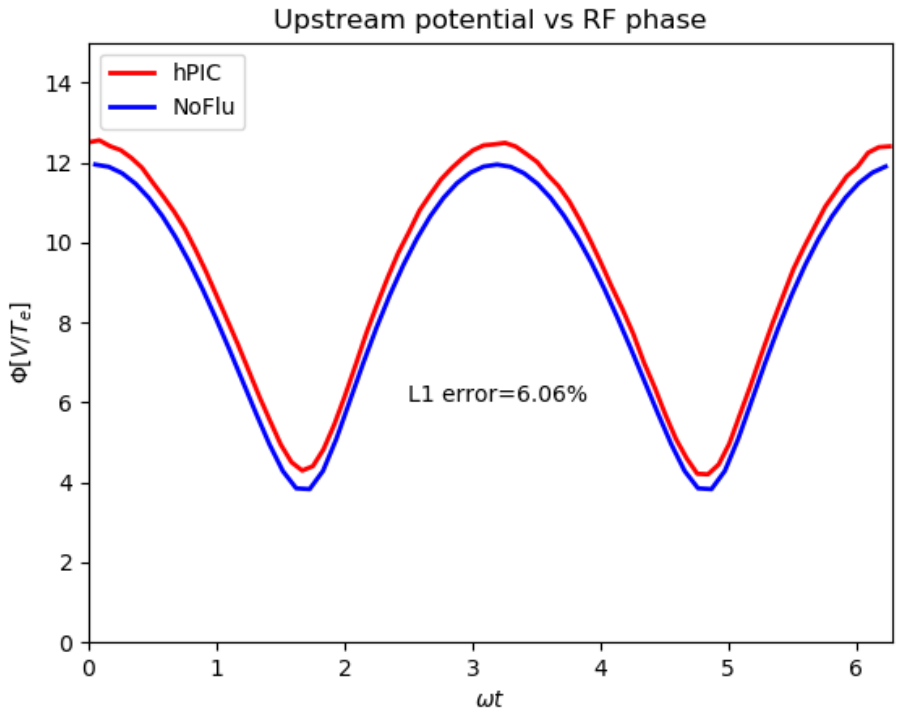

Figure 3.14: Time resolved upstream potential Φ_0. Case 3 electrical and plasma parameters presented in Table 3.5 and Table 3.4 respectively. Data adapted from [10].

will be discussed in sec 3.2.

Fig. 3.15 compares the current waveforms at the left wall of the two codes for case 3. Electrical and plasma parameters presented in Table 3.5 and Table 3.4 respectively. Agreement on waveforms provides a crucial benchmarking step as they encompass the plasma dynamics, particle fluxes, electrical properties, and displacement current. Excellent agreement can be seen between the two codes with a maximum L1 norm difference of 2.19% for the total current. L1 norms difference for the current waveforms has been quantified and shown in Fig. 3.15.

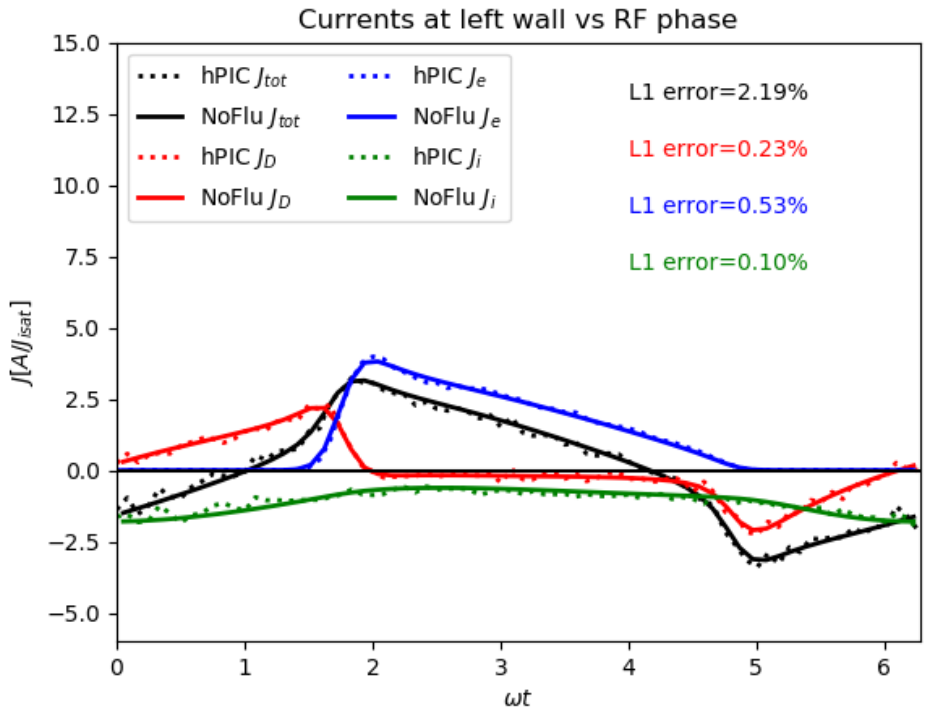

Figure 3.15: Ion J_i, Electron J_e, Displacement J_D and Total current J_{tot} waveforms at the left PFC. Case 3 electrical and plasma parameters presented in Table 3.5 and Table 3.4 respectively. Data adapted from [10].

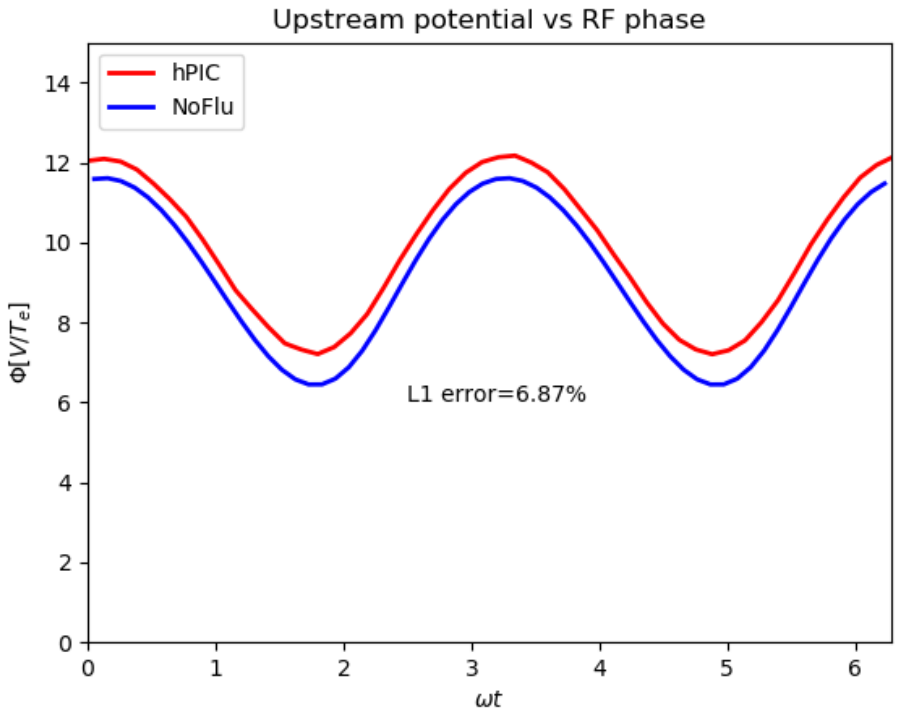

Figure 3.16: Time resolved upstream potential Φ_0. Case 4 electrical and plasma parameters presented in Table 3.5 and Table 3.4 respectively. Data adapted from [10].

Case 4

Fig. 3.16 compares the output $\langle \Phi_0 \rangle$ of the two codes for case 4. Electrical and plasma parameters presented in Table 3.5 and Table 3.4 respectively. Good agreement can be seen between the two codes, quantified by an L1 norm difference of 6.87%. Such an offset, while still an excellent agreement, will be discussed in sec 3.2.

Fig. 3.17 compares the current waveforms at the left wall of the two codes for case 4. Electrical and plasma parameters presented in Table 3.5 and Table 3.4 respectively. Agreement on waveforms provides a crucial benchmarking step as they encompass the plasma dynamics, particle fluxes, electrical properties, and displacement current. Good agreement can be seen between

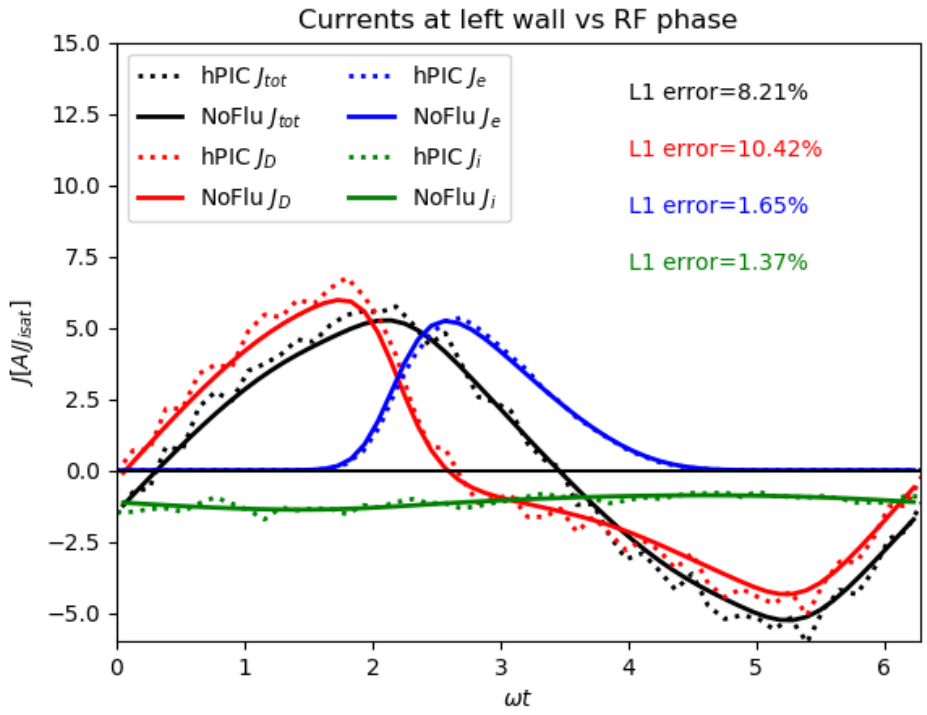

Figure 3.17: Ion J_i, Electron J_e, Displacement J_D and Total current J_{tot} waveforms at the left PFC. Case 4 electrical and plasma parameters presented in Table 3.5 and Table 3.4 respectively. Data adapted from [10].

the two codes with an L1 norm difference of 8.21% for the total current. L1 norms difference for the current waveforms has been quantified and shown in Fig. 3.17. At a frequency $\omega = 2.0$, the displacement current and electron current are on the same order of magnitude. Strong nonlinearity in the system comes from the exponential in the Maxwell-Boltzmann electron response. Due to the nature of the charge conservation regime [40], this case provides the hardest test for the implicit implementation testing the limits of convergence. While the explicit implementation has failed in such cases, the implicit implementation has successfully captured the displacement current within a 10% difference when compared to NoFlu.

Case 5

Fig. 3.18 compares the output $\langle \Phi_0 \rangle$ of the two codes for case 5. Electrical and plasma parameters presented in Table 3.5 and Table 3.4 respectively. Good agreement can be seen between the two codes, quantified by an L1 norm difference of 4.62%. Such an offset, while still an excellent agreement, will be discussed in sec 3.2.

Fig. 3.19 compares the current waveforms at the left wall of the two codes for case 5. Electrical and plasma parameters presented in Table 3.5 and Table 3.4 respectively. Agreement on waveforms provides a crucial benchmarking step as they encompass the plasma dynamics, particle fluxes, electrical properties, and displacement current. Excellent agreement can be seen between the two codes with a maximum L1 norm difference of 4.48% for the electron current. L1 norms difference for the current waveforms has been quantified and shown in Fig. 3.19.

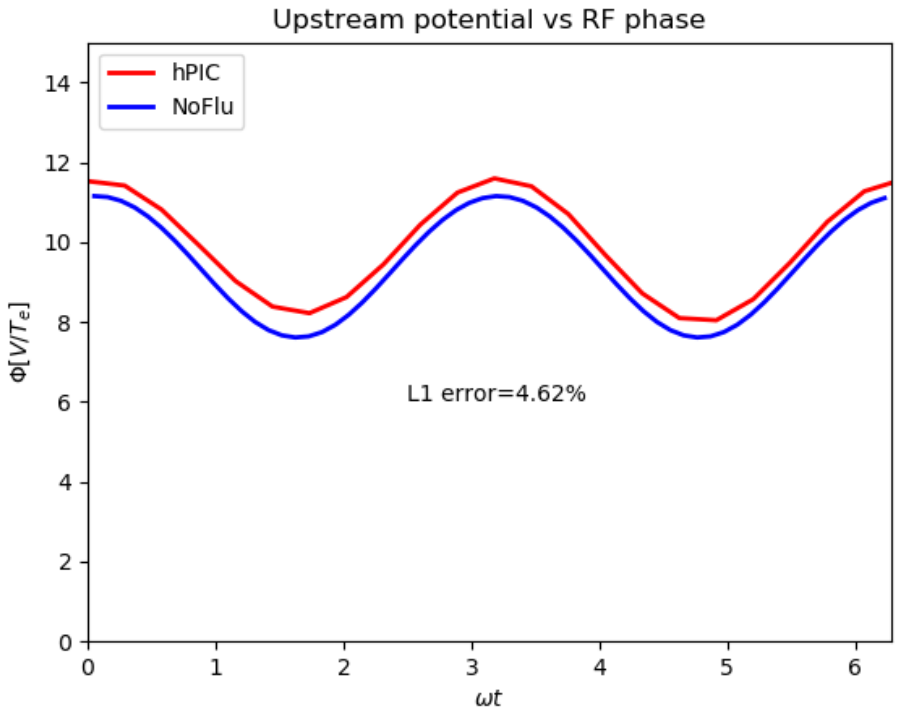

Figure 3.18: Time resolved upstream potential Φ_0. Case 5 electrical and plasma parameters presented in Table 3.5 and Table 3.4 respectively. Data adapted from [10].

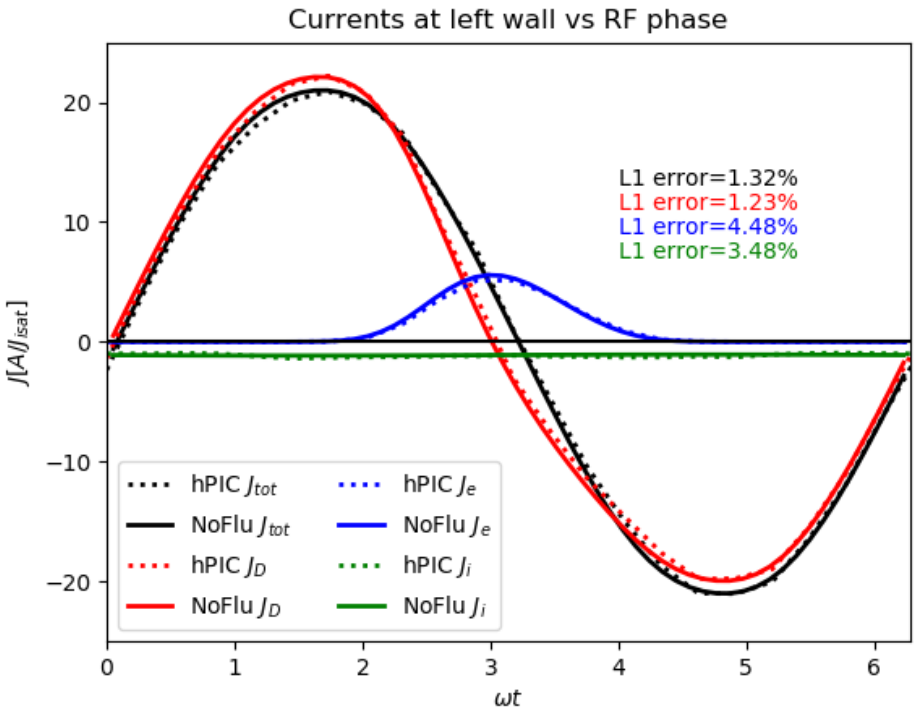

Figure 3.19: Ion J_i, Electron J_e, Displacement J_D and Total current J_{tot} waveforms at the left PFC. Case 5 electrical and plasma parameters presented in Table 3.5 and Table 3.4 respectively. Data adapted from [10].

Upstream potential offset

As previously noted, all the cases show a small offset between hPIC and NoFlu in the upstream plasma potential Φ_0, with the hPIC result exceeding the NoFlu result by about 0.5 to 0.7 in dimensionless units, i.e. relative to T_e. This difference can be traced to the additional contribution of the presheath, which is present in the hPIC simulations. For example, for the case *omega* = 0.5 at $\omega t = 0$, the measured presheath potential drop in hPIC is 0.575 in dimensionless (T_e/e) units, which is within the range of potential offsets between the two codes. In hPIC plasma is sourced throughout the entire volume with a mean initial velocity of zero and a thermal ion distribution. In NoFlu, the plasma is injected upstream towards the plates with a velocity on the order of sound speed $u_i = 1.1c_s$.

CHAPTER 4

NUMERICAL CHARACTERIZATION OF ION ENERGY ANGLE DISTRIBUTIONS IN RF SHEATHS

In RF sheaths kinetic ion energy-angle distributions (IEAD) are highly important. Ions in RF sheaths have kinetic energies on the order of hundreds of T_e. At these energies the ion sputtering yield is increased. In addition, unlike in classical sheaths, ion energy-angle distributions (IEAD) change as a function of time during an RF cycle. Recently, Myra *et al.*[36, 24] and Elias *et al.* [9] developed models that investigate how the plasma and PMI behave in RF sheaths. Elias *et al.* [9] and Myra *et al.* [36, 24] have shown motivating agreement with experimental data. Despite research focus into modeling PMI in RF conditions, an accurate kinetic description of the IEAD has not been attempted. Fluid models produce the overall features of the PMI but lack the detailed description of the IEAD. Elias *et al.* [9] uses a fluid model to provide an IEAD under the assumptions of Maxwellian fluid distributions for both the ions and the electrons. Due to the sensitivity of the PMI to IEAD, proper kinetic descriptions of the IEAD at the PFC are needed to model the surface response and impurity sputtering.

A fluid model is intrinsically unable to provide such distributions, because it only tracks the ion and electron densities, the fluid velocity, and the electric potential. A fluid model does not produce any inherently-kinetic quantity such as an IEAD. In a fluid model, values for the ion impact energy and angles must be reconstructed as most-probable values from the fluid moments. However, any calculation on impurity emission requires accurate IEADs as

an input to sputtering calculations. The hPIC model can be used to perform a parametric investigation of the IEAD in RF sheaths, and evaluate the impact of the ion bombardment on the Faraday screen of an ICRH antenna. The main focus of this chapter is to present a description of the IEAD coming from RF sheaths at the PFC.

4.1 RF sheath dual plate model

The simulation domain is shown in Fig. 4.1. It is a dual plate system with a magnetic field angle ψ evaluated with respect to the wall normal. The walls are biased using a sinusoidal voltage with a peak-to-peak voltage of $V_{pp} = 200$ V and a variable RF frequency denoted by $\hat{\omega}$. The 1-D computational domain has a size of 200 Debye lengths and is divided into 400 computational nodes. Fig 4.2 shows an example of plasma profiles, density and potential, obtained from hPIC for a case of $\hat{\omega} = 0.5$ and $V_{pp} = 200\,V$, and magnetic field angles of $\psi = 0°, 30°, 60°, 85°$. The snapshots of the plasma profiles were taken at a point of peak RF sheath rectification.

Fig 4.2 (a) shows clear evidence that simulation captures the RF sheath rectification phenomena. The upstream plasma potential reaches $\phi_0 \approx 10T_e$ V. Such upstream potentials are not seen in classical sheaths which generally have upstream potentials on the order of $\phi_0 \approx 3T_e\,V$. Fig 4.2 (a) demonstrates the large potential drops created in the plasma sheaths due to rectified potentials. The large potential drops strip the Debye Sheath (DS) from any electrons creating an electron poor sheath. This is seen in Fig 4.2 (b) where there is a drop of several orders of magnitude in the electron density (values on the order of 10^8 at the wall) 1-2 mm away from the wall. The size of the sheath, as seen from the electron-depleted region in Fig 4.2 (b), is highly

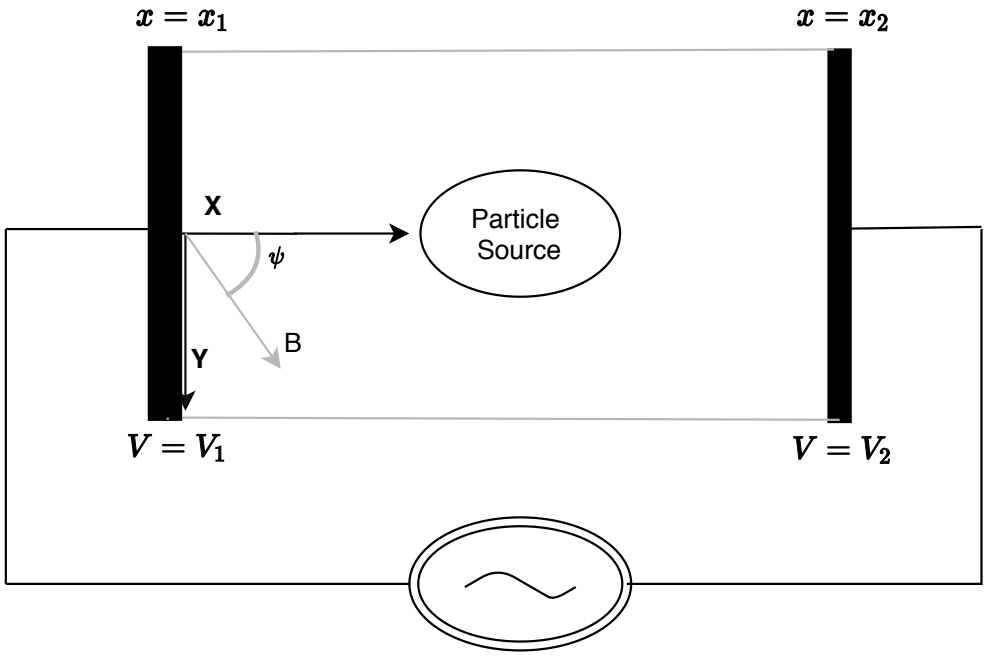

Figure 4.1: Sketch of the simulation domain. Magnetic field angle ψ measured with respect to the normal of the plasma facing component. Plasma facing components biased using an AC current.

dependent on the magnetic angle ψ, with most of the variation occurring at large magnetic angles. The magnetic presheath (MPS) needs to accelerate ions from the entrance condition of $|u_x| = c_s \cos\psi$ to the Bohm sheath criteria at the entrance of the Debye sheath, $|u_x| = c_s$, where u_x is the ion drift velocity in the direction perpendicular to the wall and c_s is the ion acoustic speed.

The MPS has to sustain a potential drop that can provide this acceleration. At larger magnetic field angles ψ, the difference in ion speeds between the MPS entrance criteria and the Bohm sheath criteria is larger. Hence, a physically larger MPS is needed to sustain a larger acceleration.

The ion density at the wall seen in Fig 4.2 (c) also depends on the size of the MPS. The ion densities at the wall fall from $1.26 \times 10^{16}\, m^{-3}$ at perpendicular incidence ($\psi = 0°$) to $2.53 \times 10^{15}\, m^{-3}$ at grazing incidence ($\psi = 85°$).

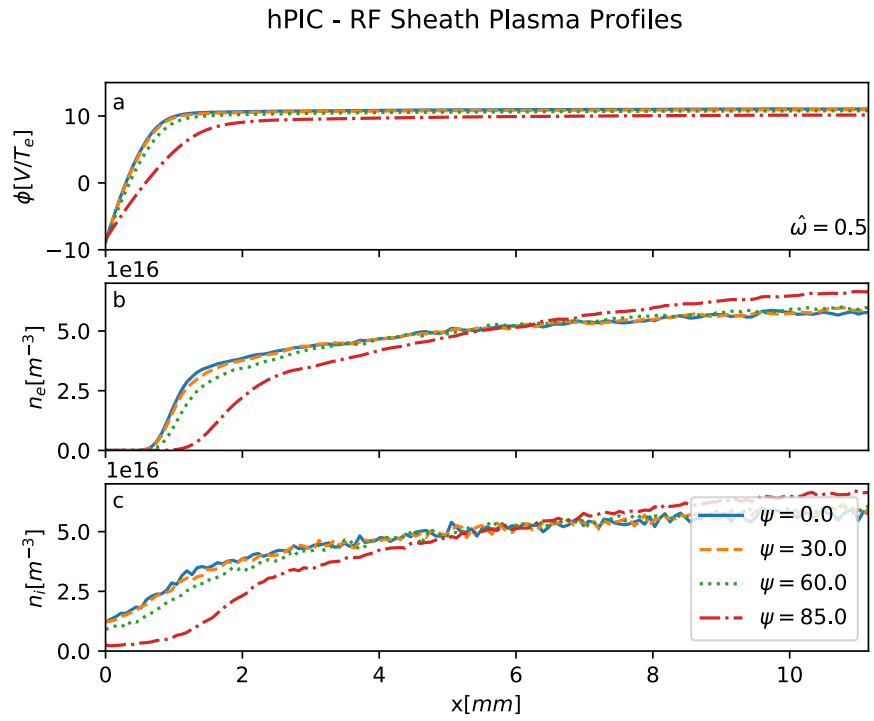

Figure 4.2: Time snapshot for profiles of simulated physical plasma parameters in an RF sheath for case $\hat{\omega} = 0.5$, $V_{pp} = 200\,V$. Four simulations with varying magnetic field angles $\psi = 0°, 30°, 60°, 85°$ plotted. Top (a) normalized electrostatic potential ϕ/T_e, center (b) electron density $n_e[m^{-3}]$, bottom (c) ion density $n_i[m^{-3}]$. The Faraday screen at $x = 0\,mm$ is biased at 88 V. Time snapshot taken at $\omega t = 0.5$.

However, while the MPS affects the ion density profile, most of the density drop is in the DS. The DS accelerates the ions through the large electric fields present, decreasing the ion density in the process. The DS also provides significant reorientation of the plasma deviating it away from a Maxwellian plasma distribution[47] assumed in fluid models.

4.2 Analysis of Ion Energy Angle Distributions in RF sheaths

In this section we report results from twelve significant simulations performed using the hPIC code. The simulations perform a parametric scan over three

physical variables, namely (1) the peak to peak RF voltage bias V_{pp}, (2) the normalized RF frequency $\hat{\omega}$, and (3) the magnetic field angle ψ. The magnetic field strength was set at a unitary value of 1 Tesla for all simulations. While NoFlu code used in Chapter 3 for benchmarking doesn't produce an IEAD, it provides a single ion energy-angle impact point at a given time. The changes in fluid ion impact energy and angle are overlaid on the kinetic hPIC IEAD figures (Fig. 4.3-4.6) for reference. We will overlay the results of the fluid model using black dots on top of the full-orbit distributions calculated using hPIC.

IEAD vs peak to peak RF wall bias

Figure 4.3 (a),(b),(c),(d) presents the IEAD plots obtained from the hPIC model for a varying peak-to-peak RF voltage of $V_{pp} = 0, 10, 100, 200\, Volts$ respectively. We chose values $V_{pp} = 0, 20, 100, 200\, V$ to span four cases containing different rectification degrees $V_{pp} = 0$, $V_{pp} = T_i$, $V_{pp} > T_i$. A constant RF frequency $\hat{\omega} = 0.5$ and magnetic field angle $\psi = 0°$ are adapted at this stage. The fluid model data is scattered as black "x" markers over the IEAD. For a magnetic field angle $\psi = 0°$, the fluid impact angle $\Theta_f \approx 0$ due to the lack of any kinetic or ion gyromotion effects. However, the fluid impact energy E_f sampled data points follow the centers the hPIC model, even clustering around the energy hot spots.

Fig. 4.3 (a) shows the IEAD for a classical plasma sheath with no wall bias and is provided for reference. Fig. 4.3 (b) represents an RF sheath with minimum RF rectification. The upstream plasma potential is on the same order of magnitude as classical sheaths. A slight horizontal stretch in the IEAD energy spread indicates that the acceleration of ions is present.

However, as the potential drop is on the order of T_i, there is no drastic shifts or splits in IEAD from classical sheaths in either the angular or energy spread.

Fig. 4.3 (c) presents the IEAD obtained in regimes were the RF rectified potential is larger than the ion temperature T_i. Two distinct IEAD centers are observed. The difference between the wall bias and the rectified upstream potential reaches values near $100\,V$ during periods of high RF rectification. This creates large electric fields that accelerate the ions to 100 eV energies. Thus, the high energy distribution center of the IEAD is centered around a maximum value $E_i \approx 100\,V$, the V_{pp} value. As the wall bias and RF sheath potential are oscillating the potential drop in the sheath oscillates between a maximum of V_{pp}, and a minimum value. The minimum value is near $E_i \approx 30\,V$, equivalent to the classical sheath potential drop. The 30 eV IEAD energy distribution center emerges from the periods of low RF sheath rectification when the electric field is at a minimum.

Fig. 4.3 (d) presents the IEAD obtained for an increased $V_{pp} = 200\,V$. Theoretically, the high energy distribution center of the IEAD is linearly dependent on the value of V_{pp}. This is confirmed by the high energy distribution center being shifted to 200 eV on the energy axis. Additionally, the spread in the angular distribution of the high energy distribution center is decreased. The acceleration gained from the potential drop is parallel to the electric field, i.e, the ions are accelerated to perpendicular impact directions. The large electric field during the period of high rectification strongly biases the ions towards a perpendicular impact angles. The low energy distribution center, on the other hand, is found to be independent of any RF voltage bias parameter. The ions represented by the low energy distribution center behave similarly to their classical sheath counterparts.

During an RF phase, the electric field acting on the ions oscillates in magnitude. The ion impact energies that are governed by electric field are also constantly oscillating from one distribution center to the other. The distribution line that connects the two centers of the distribution is due to this periodic movement of the ions between periods of low and high RF sheath rectification. We found that case Fig. 4.3 (d) $V_{pp} = 200\,V$ captured the most relevant rectification phenomena. It is also the commonly adapted voltage bias used in simulating JET[28]. Hence, a $V_{pp} = 200\,V$ is adapted as the constant value from this point forward. We also chose three set of normalized RF frequency $\hat{\omega} = 0.5, 2.0, 9.0$ and four sets of magnetic field angle $\psi = 0°, 30°, 60°, 85°$, thus covering the RF sheath regimes of interest to fusion and industrial applications.

IEAD vs Magnetic Field Angle

Fig. 4.4 presents the IEAD plots obtained from the hPIC model for a constant RF frequency $\hat{\omega} = 0.5$ and four different magnetic field angles. The magnetic field angle is increasing moving from left plot to the right plot i.e, Fig. 4.4 (a),(b),(c),(d) are plotted for cases with magnetic field angles $\psi = 0°, 30°, 60°, 85°$ respectively. The "x" markers represents the ion impact energy and angle sampled from the fluid model. At near perpendicular magnetic field angles (Fig. 4.4 (a),(b)) two clear distribution centers for the IEAD can be seen. The IEADs have a low energy distribution center at around $E_i \approx 30\,eV$ and a high energy distribution center around $E_i \approx 200\,eV$.

The created electric field is in the direction of the potential drop, i.e, normal to the biased wall. As the electric field is at a perpendicular angle with respect to the wall, the magnetic field inclination governs the effects

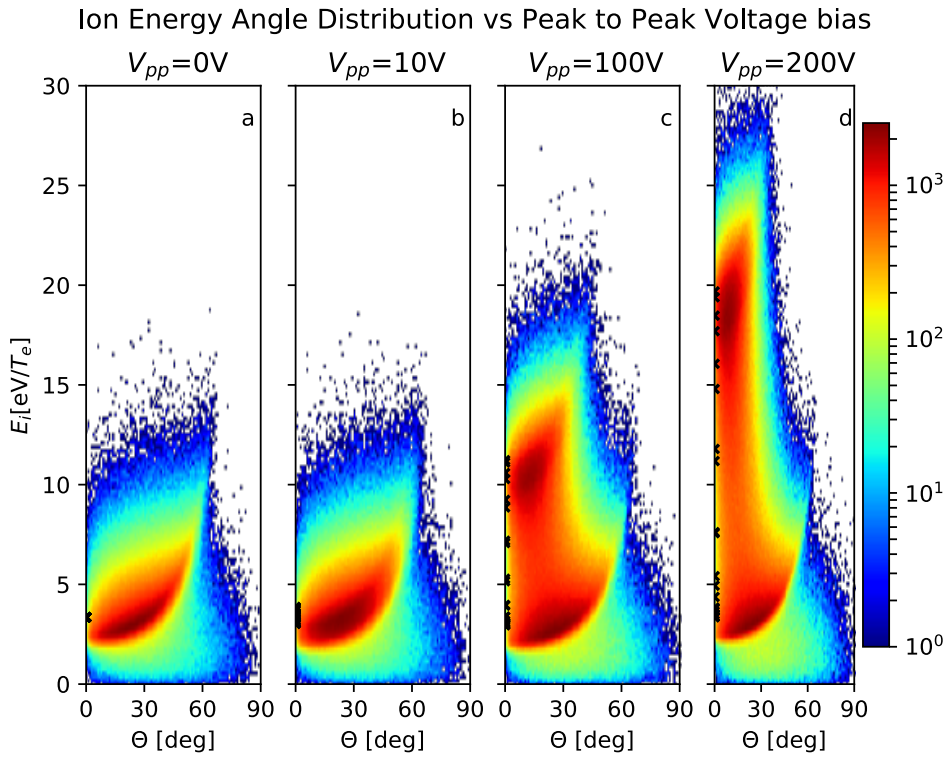

Figure 4.3: Kinetic ion energy-angle distribution at the wall obtained using hPIC. The energy axis is normalized to the electron temperature T_e. The simulations ran for case with $\hat{\omega} = 0.5$, $\psi = 0°$ and varying V_{pp}. Distribution plot colors are on a logarithmic scale. The contour color bar represents log_{10} of the number of particles in a $dEd\theta$. Black "x" markers over the ion energy-angle distribution represent the fluid impact energy and angle. The fluid model data consists of 20 points acquired by uniform sampling from the time domain. The sampled points cover a complete RF cycle.

of the $E \times B$ force on the particle drift. For magnetic fields perpendicular to the wall $\psi = 0°$, the electric and magnetic fields are parallel yielding an $E \times B$ force equal to zero. The $E \times B$ force has no effect on the particle drift or impact energy and angle. As the fluid model does not capture any kinetic or gyromotion effects any angular spread is be attributed to the $E \times B$ force alone. At low magnetic field angles the ion motion is mainly governed by the electric field. The $E \times B$ force effects start to become apparent as the magnetic field angle increases.

Fig. 4.4 (c) shows the IEAD for a magnetic field angle $\psi = 60°$. Such a magnetic field angle represents what is known as toroidal aligned configuration. In toroidal aligned configurations, the ICRH faraday screen is aligned with the tokamak's toroidal axis rather than the magnetic field. During periods of low RF sheath rectification the $E \times B$ drift affects the low energy center ($E_i \approx 50\,eV$) of the distribution in both the kinetic and fluid models. The center of the distribution is shifted towards the magnetic field angle $\psi = 60°$. During periods of high RF sheath rectification, when the electric field force is at its maximum, the $E \times B$ drift still affects the IEAD center but is competing with a stronger electric field. The shift of the angular distribution is visible in the high energy center ($E_i \approx 200\,eV$) of the distribution. However, due to the presence of a stronger perpendicular electric field the shift is smaller when compared to the low energy center of the distribution.

Fig. 4.4 (d) shows the IEAD for a magnetic field angle $\psi = 85°$. Such a magnetic field angle represents what is known as a field aligned configuration. Field aligned configurations result when the ICRH FS is aligned with the tokamak's magnetic field. This configuration has been shown experimentally to reduce sputtering[20, 21]. Fig. 4.4 (d) suggests that the IEAD could play a role in the reduction of sputtered impurities for field aligned configuration.

At high inclination magnetic fields $\psi = 85°$ (Fig. 4.4 (d)), the $E \times B$ force dominates. The subsequent $E \times B$ drift creates a shift in the angular center of the distribution towards the magnetic field angle. The shift in angular distribution is consistent at both low and high energy centers of the distribution. The oscillatory nature of the rectified electric field is overshadowed by the constant $E \times B$ force. As the fluid model does not capture any ion gyromotion effects, the model has failed under such conditions. A phase space analysis into the ion gyromotion is provided in Sec 4.3.

The effect of the $E \times B$ drift dominating is that the ions have a more uniform acceleration throughout the RF phase. The two distinct high and low energy distribution centers are shifted to lower and higher energies respectively. The boundaries between the high and low energy distribution centers fades and one can consider them merged. As the sputtering yield exhibits a non-linear response to the ion impacting energy, the downward shift in the high energy distribution center can have a more significant impact on the sputtering yield than the upward shift in the low energy distribution center. This suggests that a lower sputtering yield would arise from the IEAD simulated using a field-aligned FS vs the IEAD simulated using a poloidal-aligned FS. While such findings are consistent with experimental data[6], a complete simulation using coupled sputtering and hPIC simulation codes would be required to confirm the hypothesis.

IEAD vs RF frequency

Fig. 4.5 (a),(b),(c) presents the IEAD for three increasing RF frequencies of $\hat{\omega} = 0.5, 2.0, 9.0$ for a magnetic field angle $\psi = 30°$. At low magnetic field inclinations the $E \times B$ effects are overshadowed by the presence of a strong

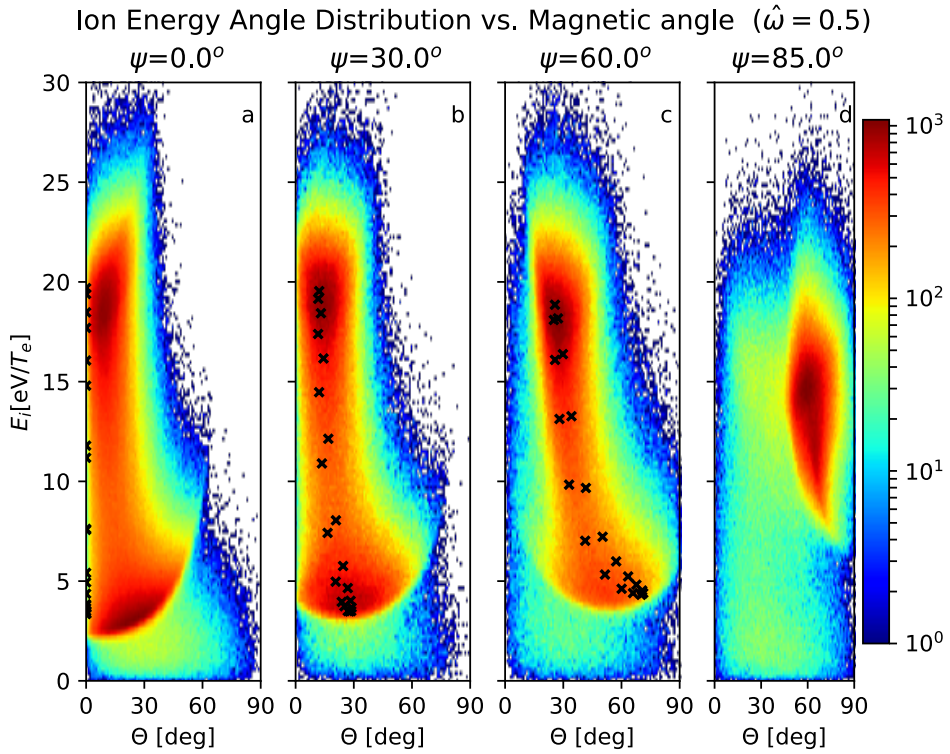

Figure 4.4: Kinetic ion energy-angle distribution at the wall obtained using hPIC. The energy axis is normalized to the electron temperature T_e. The simulations ran for case with $\hat{\omega} = 0.5$, $V_{pp} = 200\,V$ and varying ψ. Distribution plot colors are on a logarithmic scale. Contour color bar represents log_{10} of the number of particles in a $dEd\theta$. Black "x" markers over the ion energy-angle distribution represent the fluid impact energy and angle. The fluid model data consists of 20 points acquired by uniform sampling from the time domain. The sampled points cover a complete RF cycle.

electric field. Fig. 4.5 (a) presents the IEAD for an RF frequency $\hat{\omega} = 0.5$ and magnetic field angle $\psi = 30°$. At an RF frequency of $\hat{\omega} = 0.5$, the ions are highly mobile. There are two distinct distribution centers; a low energy distribution center at around $E_i \approx 50\,eV$, and a high energy distribution center around $E_i \approx 200\,eV$. The ions feel the effect of the sinusoidal RF potential rectification as they respond more rapidly. As the RF frequency increases, the ions lose their mobility. The ions do not have enough time to fall through the potential drop before the upstream RF rectified potential decreases. In effect the ions pass through a time averaged acceleration and electric fields. The loss of ion mobility has clear effects on the IEAD.

Fig. 4.5 (b) presents the IEAD for an increased RF frequency (with respect to Fig. 4.5 (a)) $\hat{\omega} = 2.0$ and magnetic field angle $\psi = 30°$. In terms of the angular spread of the IEAD an increase in the RF frequency, for a magnetic field angle $\psi = 30°$, does not shift the distribution angularly. The gap between the high and low energy distribution centers decreases, a direct result of the decrease in ion mobility. The low energy distribution center increases to around $E_i \approx 80\,eV$ and a high energy distribution center decreases to around $E_i \approx 140\,eV$. The effects of the decrease in the high energy distribution center outweigh the increase in low energy distribution center. Therefore, an increased RF frequency is expected to decrease the total sputtering yield from the FS due to the non-linearity of the sputtering yield curve.

A further increase in RF frequency above $\hat{\omega} = 2.0$ leads to a further loss of ion mobility. Fig. 4.5 (c) presents the IEAD for an RF frequency $\hat{\omega} = 9.0$ and magnetic field angle $\psi = 30°$. Consistent with the previous increases in RF frequency the high and low energy distribution centers are further shifted to lower and higher energies respectively. At RF frequencies $\hat{\omega} \gg 1$, the IEAD high and low energy distribution centers converge to one energy distribution

center around $E_i \approx 110\,eV$. Effectively, the ions are no longer subject to any modulation in the rectified sheath potential and instead experience a time-averaged potential drop. Any further increase above $\hat{\omega} = 2.0$ in RF frequency does not produce notable shifts in IEAD. Additionally, at small magnetic field angles, the $E \times B$ force has no effect on the the angular spread of the IEAD.

For field-aligned magnetic field inclinations, similar to those in future fusion devices, the effect of an increase in RF frequencies extends to the angular spread of the IEAD. Fig. 4.6 (a),(b),(c) presents the IEAD for three increasing RF frequencies of $\hat{\omega} = 0.5, 2.0, 9.0$ for a magnetic field angle $\psi = 85°$. At high inclinations the $E \times B$ effects are dominant across all RF frequencies. The angular distributions are shifted towards the magnetic field angles. At low RF frequencies $\hat{\omega} < 1$, effects of the sheath rectification are still visible. For high RF frequency $\hat{\omega} > 1$, the effects of the RF rectified sheath modulation are minimized. Fig. 4.6 (b) presents the IEAD for an increased RF frequency (with respect to Fig. 4.6 (a)) $\hat{\omega} = 2.0$ and magnetic field angle $\psi = 85°$. The high and low energy centers have already converged towards a single distribution center. Further increasing in RF frequency, Fig. 4.6 (c) $\hat{\omega} = 9.0$, has minimal effects on the IEAD.

4.3 Discussion of kinetic ion effects on Ion Energy Angle Distributions

Our discussion will focus on a simulated case taken to represent the recent experimental campaign in JET[11]. JET campaign excited RF waves with an RF frequency of 42 MHz. JET campaign also measured a minimum electron density of 1e17 m^{-3} near outer limiters. This corresponds to a maximum

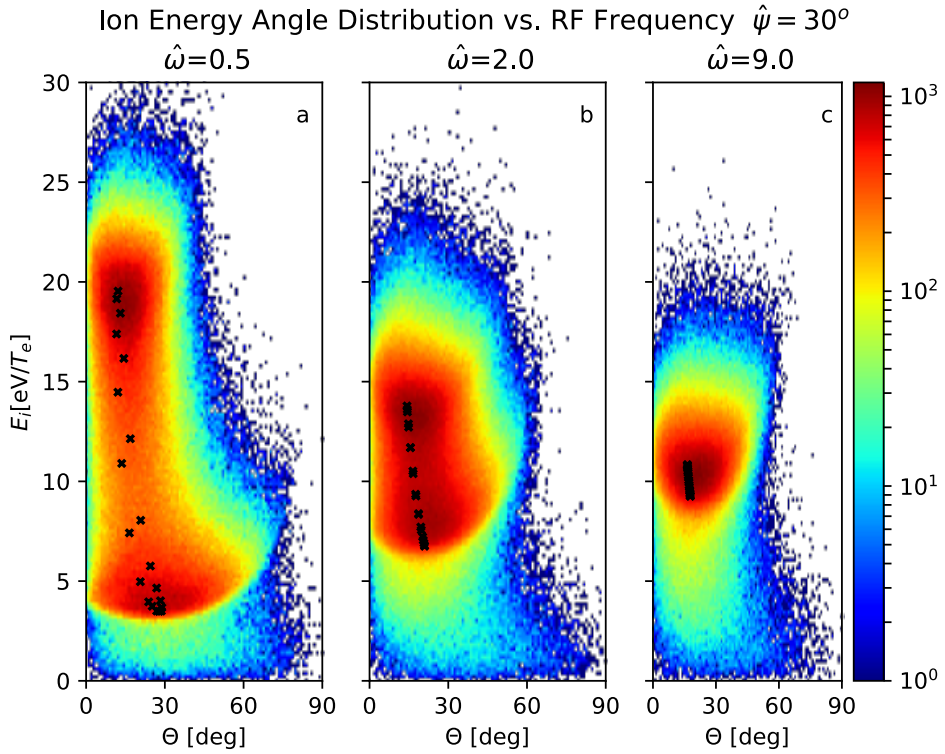

Figure 4.5: Kinetic ion energy-angle distribution at the wall obtained using hPIC. The energy axis is normalized to the electron temperature T_e. The simulations ran for case with $V_{pp} = 200\,V$, $\psi = 30°$ and varying $\hat{\omega}$. Distribution plot colors are on a logarithmic scale. Contour color bar represents log_{10} of the number of particles in a $dEd\theta$. Black "x" markers over the ion energy-angle distribution represent the fluid impact energy and angle. The fluid model data consists of 20 points acquired by uniform sampling from the time domain. The sampled points cover a complete RF cycle.

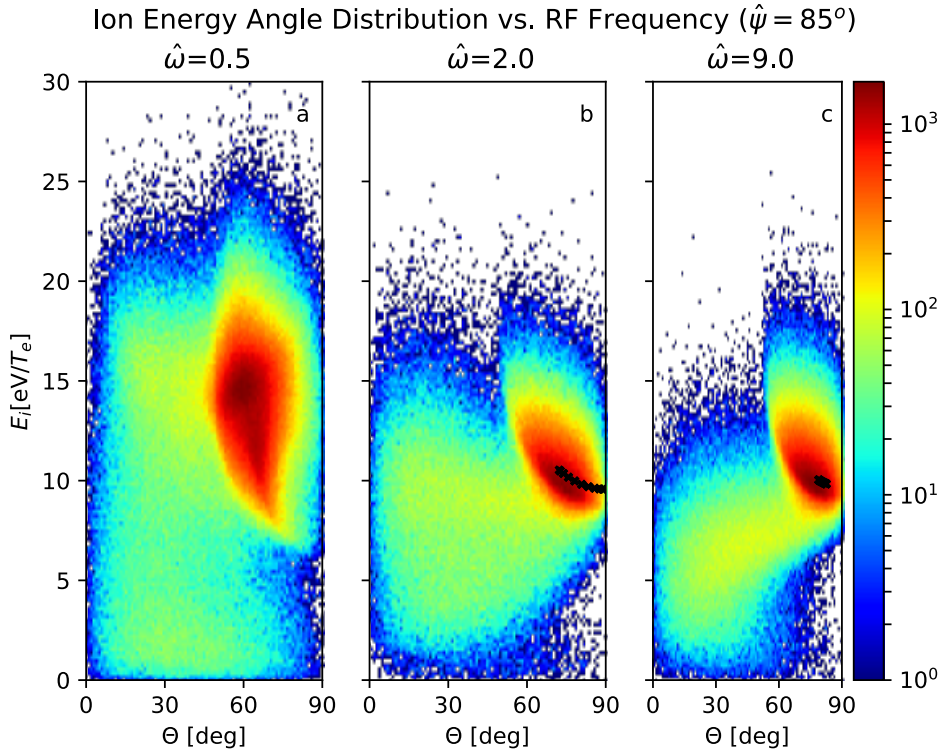

Figure 4.6: Kinetic ion energy-angle distribution at the wall obtained using hPIC. The energy axis is normalized to the electron temperature T_e. Contour color bar represents log_{10} of the number of particles in a $dEd\theta$. The simulations ran for case with $V_{pp} = 200\,V$, $\psi = 85°$ and varying $\hat{\omega}$. Black "x" markers over the ion energy-angle distribution represent the fluid impact energy and angle. The fluid model data consists of 20 points acquired by uniform sampling from the time domain. The sampled points cover a complete RF cycle.

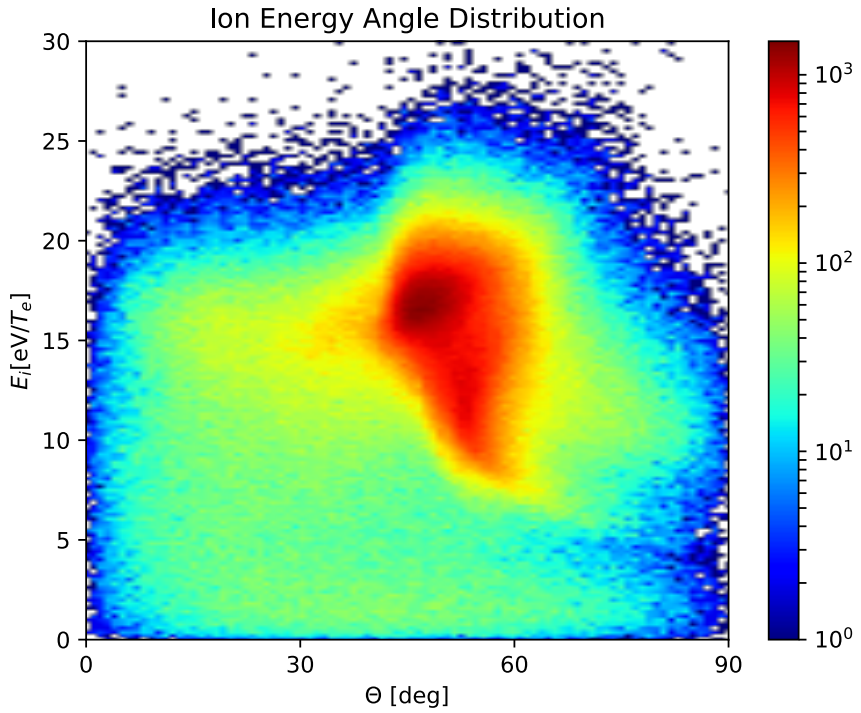

Figure 4.7: Kinetic ion energy-angle distribution at the wall obtained using hPIC. The energy axis is normalized to the electron temperature T_e. Distribution plot colors are on a logarithmic scale. Contour color bar represents log_{10} of the number of particles in a $dEd\theta$. The simulations ran for case with $V_{pp} = 200\,V$, $\psi = 85°$ and $\hat{\omega} = 0.63$. The case taken to represent the physical parameters in recent JET experimental campaign[11].

normalized RF frequency of 0.63. In addition, field-aligned configurations were adapted for JET operation and the simulated case. Thus our discussion will focus on a simulated case with he following parameters: $V_{pp} = 200V$, $\hat{\omega} = 0.63$, and $\psi = 85°$. The fluid model simulations have failed to converge under such conditions. The failure of fluid models further supports the need for a PIC model to simulate such cases.

The simulation was performed using the hPIC model. Fig. 4.7 presents the IEAD for the simulated case. The physical phenomena apparent in the IEAD are similar to Fig. 4.6 (a) for the case $V_{pp} = 200V$, $\hat{\omega} = 0.5$, $\psi = 85°$. The $E \times B$ force dominates the RF sheath physics and effect of the sheath

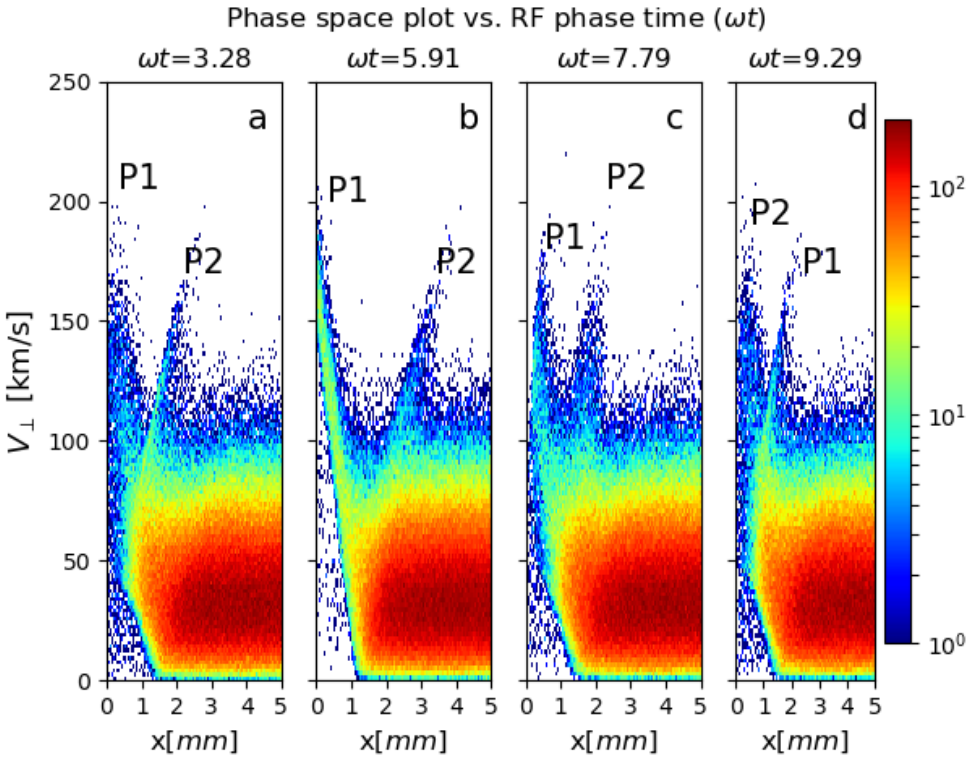

Figure 4.8: Snap shots of the phase space analysis obtained using hPIC. Velocity $v_\perp$ represents the velocity in the direction perpendicular to the magnetic field. The simulations ran for case with $V_{pp} = 200\,V$, $\psi = 85°$ and $\hat{\omega} = 0.63$. Phase space plot colors are on a logarithmic scale. Contour color bar represents log_{10} of the number of particles in a $dEd\theta$. The case taken to represent the physical parameters in recent JET experimental campaign[11]. The Faraday screen at $x = 0\,mm$ biased using an AC current. Snapshots taken to cover a complete RF cycle duration $\Delta\omega t \approx 2\pi$.

rectification is the observed. However, the modulation of the RF sheath rectification plays a minimal role. The main physical phenomena of interest is the cusp apparent at lower energies in the IEAD, a purely kinetic feature due to the ion gyromotion. Fluid models fail to capture such a feature and break down when simulating field-aligned cases at low $\hat{\omega}$.

The presence of the cusp suggests a truncation in the ion distribution at the wall. A fraction of the distribution impacts the wall while the rest complete the ion gyromotion. Phase space analysis of the case helps provide an explanation for the IEAD cusp. Fig. 4.8 presents consecutive snapshots of the phase space for the velocity perpendicular to the magnetic field $v_\perp$ spanning an RF frequency cycle. Fig. 4.8 (a) demonstrates the presence of two peaks in the phase space of $v_\perp$ that represents the high energy distribution of the ions. Peak 1 and 2 are labeled in the snapshots of Fig. 4.8. The two peaks represent ions in different phases of the ion gyromotion; peak 1 is heading towards the wall while peak 2 is heading away from the wall. The time snapshots help understand the transition between the two peak phases.

Transitioning from Fig. 4.8 (a) to Fig. 4.8 (b), peak 1 is moving towards the wall and a portion of the distribution has impacted the wall. Only a fraction of the high energy distribution is visible. The rest of the distribution has impacted the wall and is no longer part of the simulation. Transitioning from Fig. 4.8 (b) to Fig. 4.8 (c), part of the high energy ion distribution avoids the wall impact and follows the ion gyromotion back into the plasma simulation domain.

Peak 2 on the other hand, is moving away from the wall in Fig. 4.8 (b) as the ions are completing their circular gyromotion. Fig. 4.8 (c) shows peak 2 now moving towards the wall in the opposite direction to peak 1. In Fig. 4.8 (d) peak 1 and 2 have switched directions and positions relative to Fig. 4.8

(a) starting a new cycle in the process. The peaks continue to perform the periodic motion transitioning between the phases with only a portion of their distributions impacting the wall. This truncation of the ion distribution is what we hypothesise as the cause of IEAD cusp.

CHAPTER 5

NUMERICAL CHARACTERIZATION OF IMPURITY SPUTTERING IN RF SHEATHS

The main issue associated with the use of ICRH devices is the enhancement of impurity sputtering. In order to investigate the causes and mechanism behind this enhancement, our framework needs to account for PMI (Plasma-Material Interactions) in presence of ICRH operations. Plasma material interactions are highly non-linear in nature, translating the RF sheath rectification into an amplification in the sputtering yield and sputtered flux.

The nonlinear dependence of the Ion energy angle distribution on the RF sheath phase and RF sheath parameters was highlighted in Chapter 4. This nonlinearity comes into play when considering the nature of PMI. Previously, the hPIC framework simply registered the particles leaving the domain in a list that is available for post-processing. This list of particles is post processed into the Ion energy angle distributions (shown in chapter 4) assumed to be interacting with the PFC.

To accurately capture the nonlinear nature of the plasma material interactions and for proper evaluation of impurity sputtering from ICRH antennas and limiters, an impurity emission model (IEM) was added to the hPIC framework. The IEM handles the plasma material interaction section of the framework and must be able to translate incoming IEAD into a sputtered impurity list. Identifying a proper IEM is the first task in creating a hPIC-IEM framework. For the purposes of this work, we have identified RustBCA [13] as a compatible IEM model.

5.1 RustBCA: A new Binary Collision Approximation code

Coupling of the PIC model to RustBCA allows us to capture the relevant plasma material interactions. Some of those interactions that are captured by RustBCA are presented in Fig 5.1. The main interactions that concern a complete hPIC-RustBCA framework would be the sputtering of impurities from the PFC. The minimum requirements that the desired IEM should be able to capture are:

- Simulate all combinations of incident ion and target species
- Perform 2D geometry simulations
- Track ions, recoils, and target atoms full trajectories
- Accept an easy human readable input
- Accept a kinetic description of particles
- Compatible with hPIC framework
- Provide the kinetic description of emitted particles including energy and angle distribution
- Provide the sputtering yields and reflection yields for the given incoming IEAD

The considered candidates for the IEM were the Binary approximation material interaction codes RustBCA and Fractal TRIDYN (FTridyn) [12]. We settled on RustBCA as it is more compatible with hPIC and easier to use. Note that the author of this thesis has not contributed to the development of RustBCA or FTridyn, the codes were already developed.

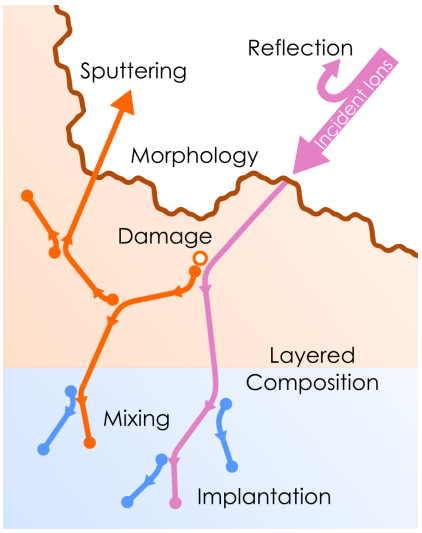

Figure 5.1: Cartoon of the physical model implemented in RustBCA (Figure taken from [12]).

RustBCA is a plasma material interaction code based on binary collision approximation. RustBCA was developed mainly for the interactions between sheaths and PFC. Additionally, RustBCA was designed and built as a scientifically flexible easy to use ion-material interactions BCA code.

Extensive benchmarking activities have been performed on RustBCA with previous available data in literature [13]. Fig. 5.2, adopted from RustBCA source code page [13], shows excellent agreement between the sputtering code against F-Tridyn [12], Yamamura [48], Bohdansky, Thomas, MD and experimental data.

5.2 Coupling Scheme

The coupling between hPIC and RustBCA was accomplished through a simple file-based, one-way weak-coupling. The IEAD output from hPIC was saved on file at each time step, converted into an input readable by RustBCA, and fed to a sequence of decoupled RustBCA simulations. RustBCA

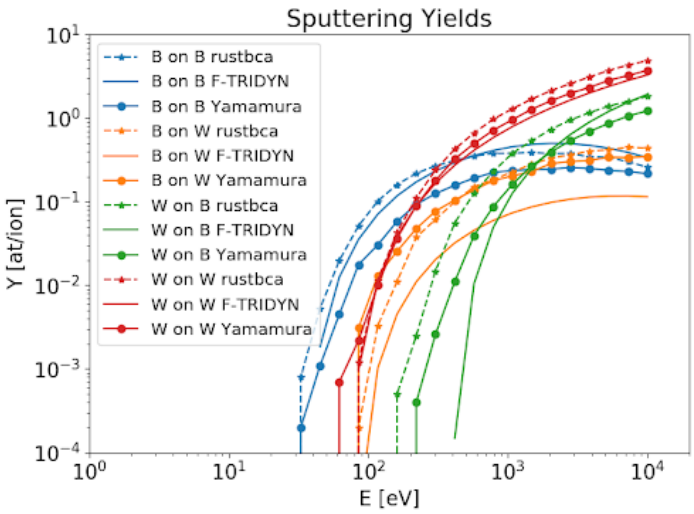

Figure 5.2: RustBCA benchmarking results. Extensive benchmarking against F-Tridyn, Yammamura, Bohdansky, homas, MD and experimental data. Figure taken from[12]

produced a list of particles sputtered and reflected from the PFC, which were analyzed in post-processing to obtain particle fluxes and sputtering yield as a function of time. A proper interface module was implemented for time resolved coupling. Due to the nature of the ICRH RF sheaths, the IEAD passed to RustBCA had to be time resolved.

5.3 Time resolved coupling

In order to couple hPIC and RustBCA together, a framework such as that illustrated in Fig. 5.3 was developed. Time-resolved fluxes and IEAD from hPIC were recorded as a list of particles interacting with the material at every time step. The recorded particle list was then converted to input files in TOML format, readable by RustBCA. Additionally, the particle lists were up-sampled for better statistics by using the RustBCA up-sampling feature. RustBCA can re-run a non-deterministic simulation N_{up} times for

a particle, where N_{upi} is the up-sampling ratio for the particle i in the list. As RustBCA is a non-deterministic model, each particle was up-sampled 200 times by setting the parameter $N_{upi} = 200$ for all the particles in the list.

Time resolved coupling was performed by coupling of hPIC and RustBCA at every time step. This task required the development of appropriate normalization methods to properly calculate the sputtered particles fluxes. Time resolved coupling now allows the hPIC-RustBCA framework to quantify :

- Time resolved density of impurities in the plasma
- Time resolved sputtering yield
- Time resolved kinetic description of the plasma material interaction
- Time resolved kinetic description of the sputtered particles including energy and angle distributions
- Relation between sputtered particle fluxes and plasma density and temperature
- Calculation of the spectral radiance of the sputtered flux

RustBCA solves the problem of the ion trajectory inside the material, and produces as an output the kinetic information of the reflected, sputtered, and deposited particles. For the scope of this thesis, we are only concerned with the sputtered particles. The sputtered particle list can be converted into sputtered flux by applying the proper normalization shown in Eq. 5.1:

$$\Gamma_{sputt} = \frac{1}{N_{sputt}} \sum_{i}^{N_{sputt}} v_i m_i \frac{N_{p2c}}{N_{up,i}} \tag{5.1}$$

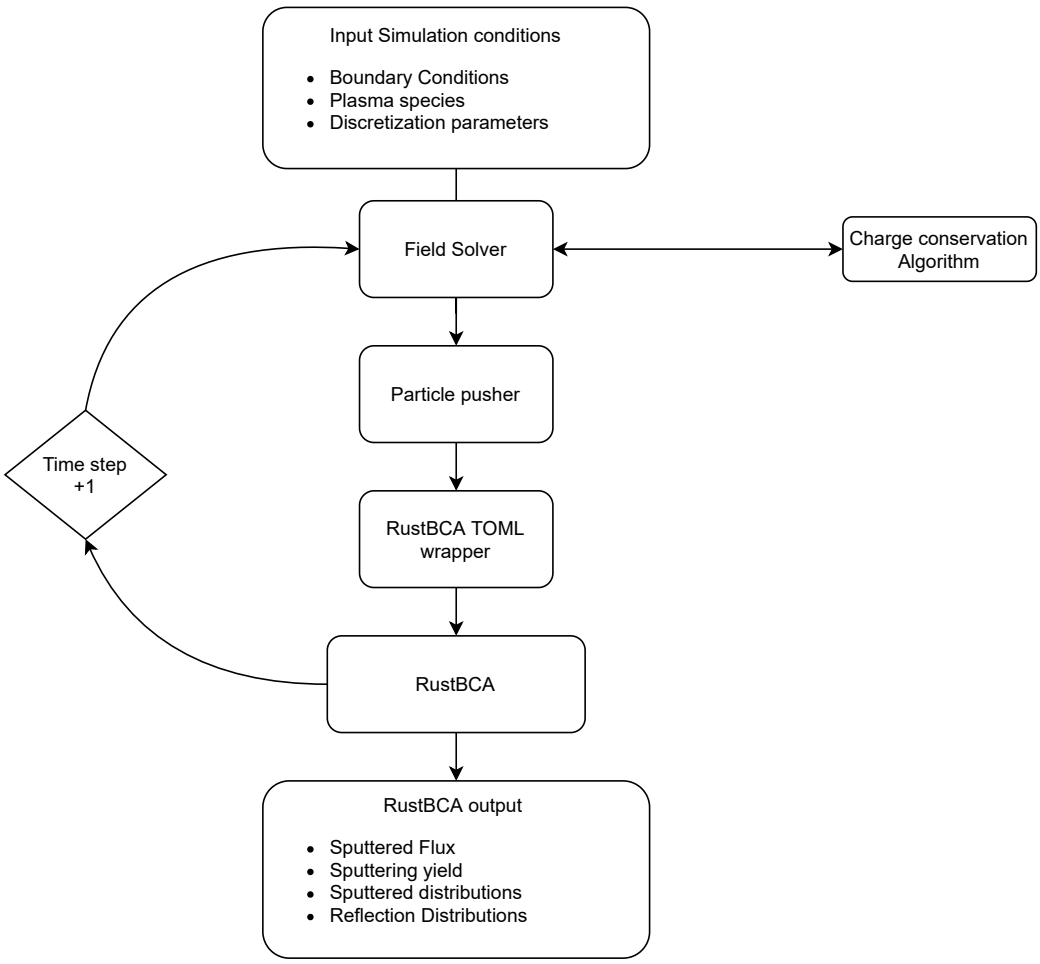

Figure 5.3: hPIC-RustBCA framework including time-resolved coupling.

where N_{p2c} is the physical-to-computational ratio of hPIC (i.e., how many physical particles are represented by a single computational macro-particle of the PIC), N_{sputt} is the total number of sputtered particles, v_i, and m_i are the sputtered particle velocity and mass, and $N_{up,i}$ is the up-sampling ratio passed to RustBCA.

5.4 The dependence of sputtering on RF phase

Sputtering has a strong non-linear dependence upon ion energy, and it is thus expected that material emission will change considerably during one RF

cycle. In order to demonstrate the dependence of sputtering on RF sheath phase, we ran two RF sheath cases with varying RF frequencies using time resolved coupling. The simulation domain used, shown in Fig. 4.1, is a dual plate system with a magnetic field angle ψ evaluated with respect to the wall normal. The plasma density, ion temperature and electron temperature were set to $5 \times 1016\ m^{-3}$, 10 eV and 10 eV respectively. The walls are biased using a sinusoidal voltage with a peak-to-peak voltage of $V_{pp} = 200$ V, a magnetic field strength $B = 1\,T$ and an angle of $\psi = 0°$. The RF frequency denoted by ω was set to 16 and 64 MHz for the cases (a) and (b) respectively. The 1-D computational domain has a size of 200 Debye lengths and is divided into 400 computational nodes.

The simulation variables are passed to hPIC. hPIC produces a list of particles that pass out of the domain on the left and right walls. The particles that leave the plasma domain are assumed to interact with the PMI. Fig. 5.4 presents the time resolved ion flux that leaves the domain through the left wall, domain presented in Fig. 4.1, for both simulated cases $\omega = 16$ MHz and 64 MHz.

Strong nonlinear oscillation in the ion flux arise during the RF cycle. The nonlinear oscillations are dependent on the RF frequency ω. As the RF frequency ω increases, the ion inertia effect becomes evident, decreasing the ion mobility across the sheath. At low RF frequency $\omega = 16$ MHz, the ions have more time to react to the variations in RF voltages. A higher RF frequency $\omega = 64$ MHz leads to a delay in the ion response and a flatter impacting flux. Case (b) $\omega = 64$ MHz produced a more moderated impacting ion flux when compared to case (a) $\omega = 16$ MHz. This is attributed to the ions being less mobile at higher RF frequencies, and hence see more of an averaged out RF potential drop.

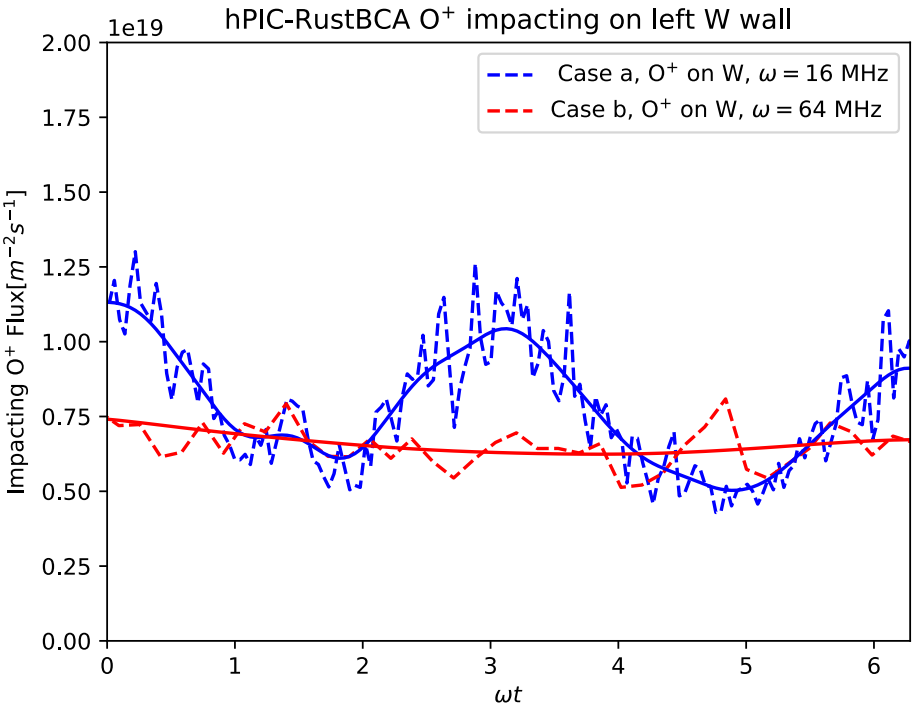

Figure 5.4: Time Resolved O^{1+} ions flux impacting on the left wall of simulation domain over one RF cycle calculated from hPIC. The kinetic description of the ion flux is passed to RustBCA for sputtering calculations. The left wall is taken to be made of tungsten W. Two cases presented with $\omega = 16$ MHz and 64 MHz.

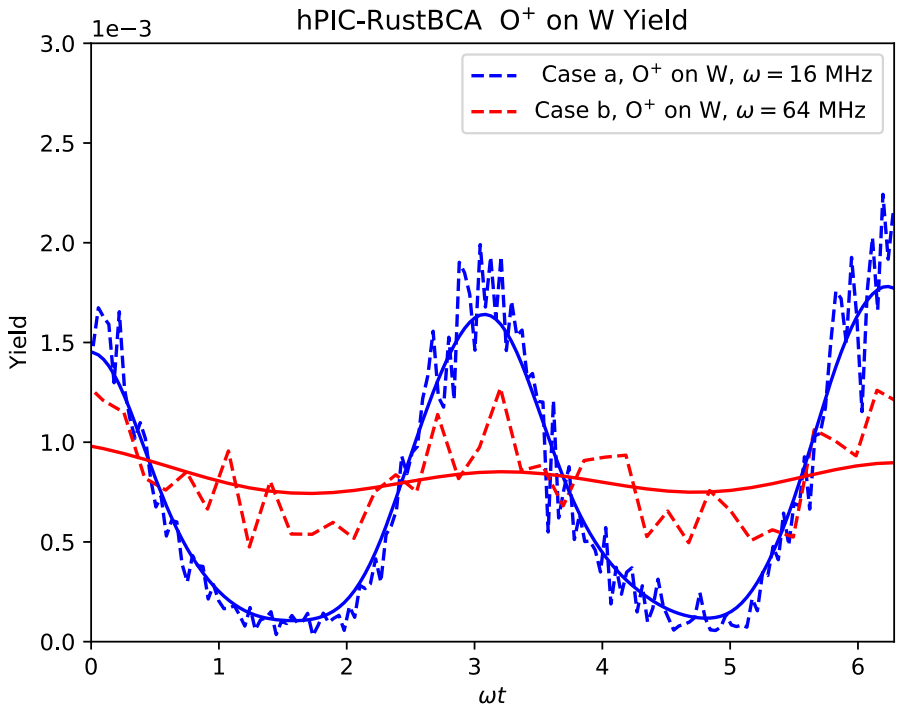

Figure 5.5: Time Resolved O^{1+} ions on W sputtering yield over one RF cycle. Two cases presented with $\omega = 16$ MHz and 64 MHz.

The oscillations in ion impact energy and flux translate directly into oscillations in the sputtered flux and sputtering yield. Variations in IEAD as a function of RF phase and RF frequency have been discussed and analyzed in depth in Chapter 4. The IEAD for case (a) $\omega = 16$ MHz, and case (b) $\omega = 64$ MHz are shown in Fig. 4.5 as cases (a) and (b) respectively. Case (a), with two distinctive high and low energy peaks in the IEAD, has larger oscillations when compared to case (b) were the high and low energy peaks in the IEAD are closer and more blended in.

The resulting dependence of the sputtering yield on the changes in IEAD is shown in Fig. 5.5. The sputtering yield oscillates within an order of magnitude depending on the RF phase. The oscillations are attributed to the changes in the IEAD during an RF phase. The oscillations in the sputtering yield follows the oscillations in the incoming ion flux, also dependent on the IEAD, adding a layer of non-linearity to the sputtered flux. Consequently, the sputtered flux produced follows the combined effect of variations in impacting ion flux and sputtering yield.

Fig. 5.6 shows the time resolved sputtered flux for cases (a) and (b) during one complete RF period. The sputtered W flux from case (a) is initially double the W sputtered flux in case (b) during RF phases with high RF sheath rectification. However, during RF phases with low RF sheath rectification sputtered flux W flux from case (a) is half the W sputtered flux in case (b). The highly nonlinear oscillations in the sputtering yield overlap with the oscillations in the incoming particle flux, resulting in large variations in W sputtered flux during an RF cycle. The interplay between the non-linearity in the IEAD, the incoming particle flux, and the sputtering yield is captured using a kinetic description of the incoming and sputtered particles fluxes.

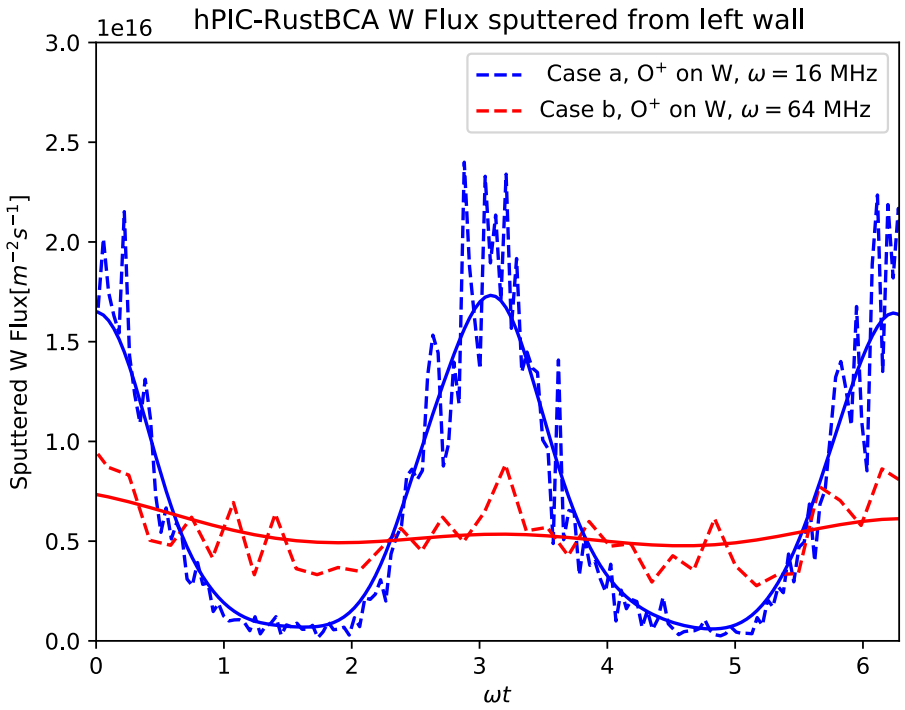

Figure 5.6: Time Resolved W flux sputtered by O^{1+} ions flux impacting on the left wall of simulation domain over one RF cycle. The sputtered particles list was calculated using RustBCA[13] and post-processed to produce the W sputtered flux. Two cases presented with $\omega = 16$ MHz and 64 MHz.

5.5 The dependence of sputtering on RF sheath parameters

Fig. 5.6 demonstrates the oscillatory nature of the sputtered flux. The instantaneous sputtered flux from case (a) can be higher or lower than case (b) depending on RF phase. The oscillatory nature of RF sheaths makes the comparison of instantaneous sputtered flux a bad metric for characterization of impurity sputtering.

Comparison of impurity sputtering must take into account the total flux sputtered over an RF cycle. Since the RF cycles vary in time periods, comparisons between RF sheath regimes are done using the cumulative fluence over a set period of time in seconds. We adopted an observation window of 1 μs. The cumulative sputtered fluence was calculated using Eq 5.2:

$$\Gamma_{fluence} = \frac{10^{-6}}{N_{2\pi}\Delta t}\int_0^{2\pi}\Gamma_W(t)dt \tag{5.2}$$

where $\Gamma_{fluence}$, $\Gamma_W(t)$, $N_{2\pi}$, and Δt are the cumulative fluence, the instantaneous sputtered flux at time t, the number of time steps per RF phase time period, and the simulation time step respectively. The 10^{-6} factor is the observation window of 1 μs.

Additionally, over time scales much longer than one RF cycle, the plasma effectively sees a continuous flux of impurities. Comparing the cumulative fluence over a period of $1\mu s$ provides a useful metric to compare the net effect of impurity production at the surface of the RF antenna. This comparison metric was adopted for characterization of the different RF sheath parameters.

Dual Plate Model

The simulation domain is similar to the one in Sec. 5.4, shown in Fig. 4.1. It is a dual plate system with a magnetic field angle ψ evaluated with respect to the wall normal. The plasma density, ion temperature and electron temperature were set to $5e16\ m^{-3}$, 10 eV and 10 eV respectively.

The walls are biased using a sinusoidal voltages with a peak-to-peak voltage V_{pp} in the range of $0-200$ V. The magnetic field strength was set to $B = 1\,T$, with varying angles ψ in the range $0° - 80°$. The RF frequencies ω used in the simulations are within the range of $0 - 64$ MHz. When normalized with respect to the plasma frequency ω_{pi}, the RF frequency range is given in normalized unit as $\hat{\omega} = \frac{\omega}{\omega_{pi}} = 0 - 2$ s. We adopted natural units in this chapter to provide the reader with the sense of magnitudes considered for RF frequencies.

The 1-D computational domain has a size of 200 Debye lengths and is divided into 400 computational nodes. The total physical simulation time is set to $1\mu s$ and the cumulative fluence was compared. The parameters $V_{pp}\,, \omega$ and ψ were chosen in line with the cases discussed in Chapter 4. In this section, we will focus on the resulting sputtered fluence rather than the IEAD. The reader is referred back to Chapter 4 for a discussion on the IEAD in RF sheaths.

Sputtered fluence vs peak to peak RF wall bias

The main parameter governing the enhancement in impurity sputtering is the peak-to-peak voltage bias V_{pp}. We analyze the effects of V_{pp} on the sputtered fluence by scanning over a wide range of V_{pp}. We chose values $V_{pp} = 0-200\,V$ to span cases containing different rectification degrees $V_{pp} = 0$, $V_{pp} = T_i$ and

$V_{pp} > T_i$. A constant RF frequency $\omega = 16$ MHz and magnetic field angle $\psi = 0°$ are adapted.

Fig. 5.7 shows the sputtered fluence for a time period of $1\mu s$ vs V_{pp} in Volts. A clear relation between the sputtered fluence and V_{pp} can be seen. As V_{pp} increases, the RF plasma sheath exhibit larger potential drops. The ions falling through the larger potential impact the wall at higher energies. This in turn leads to an increase in the sputtering yield and an increase in the sputtered flux.

Discussed in further detail in Chapter 4, the IEAD in RF frequency cases have a high energy peak center and a low energy peak center. As V_{pp} increases, the ions gain higher impact energies and the high energy peak is shifted to energies similar to V_{pp}. The ions in the high energy peak sputter more particles from the PFC. The increase in sputtering yield is attributed to the ions coming from the high energy peak.

The sputtered fluence in turn increases by an order of magnitude from 2.72×10^{17} for no wall bias $V_{pp} = 0$ V, a case resembling a classical thermal plasma sheath, to 8.8×10^{18} for $V_{pp} = 200$ V. Optimizing the needed wall bias V_{pp} for power delivery plays an important role in minimizing the plasma impurity content.

Sputtered fluence vs magnetic field angle

The antenna alignment with respect to background magnetic field is an important design parameter when operating ICRH devices. We can simulate different antenna alignments by adapting different magnetic field angles ψ. Power delivery requirements and range of RF frequencies the ICRH can launch limit the range of possible V_{pp} and ω parameters. However, the mag-

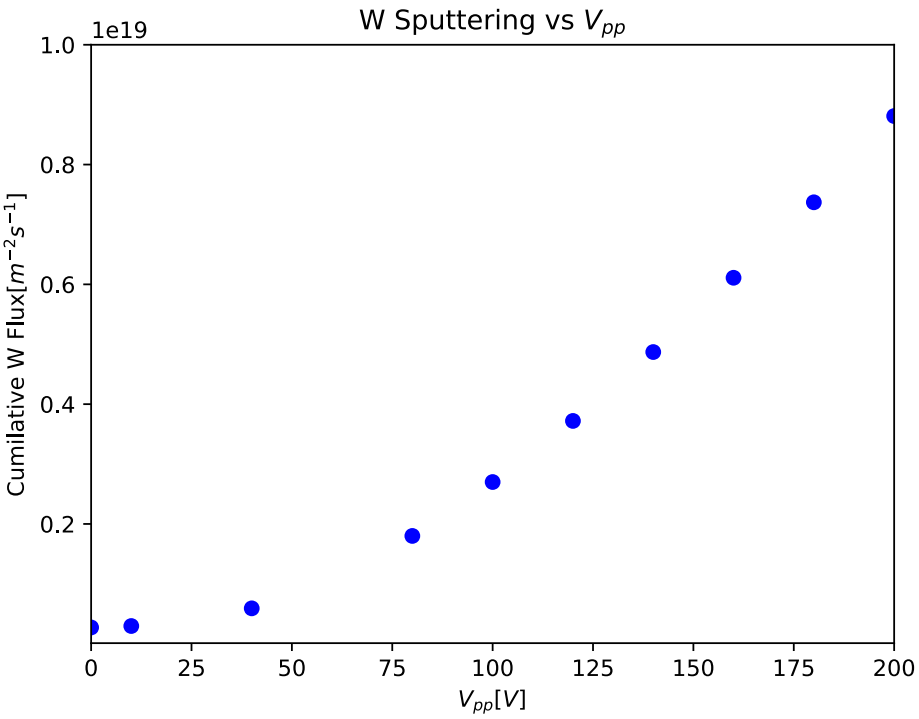

Figure 5.7: Sputtered W impurity flux vs Peak to Peak wall bias. The simulations ran for case with $\omega = 16$ MHz, $\psi = 0°$ and varying V_{pp}. Model presented in Fig. 4.1 with wall material made of W and plasma mixture of 95% D^+ ions and 5% O^+ ions.

netic field angle ψ is less constricted by the power delivery requirements.

Two antenna alignments have been considered and studied in literature: field aligned and toroidally aligned antenna[6]. We analyze the effects of ψ on the sputtered fluence by scanning over the range of ψ. We chose values $\psi = 0° - 80°$ to span all cases capturing the different ICRH alignment configurations. A constant RF frequency $\omega = 16$ MHz and peak to peak wall bias $V_{pp} = 200$ V are adapted.

Fig. 5.8 shows the sputtered fluence for a time period of $1\mu s$ vs ψ in Degrees. Where ψ is measured with respect to the surface normal. A clear relation between the sputtered fluence and ψ can be seen. The sputtered fluence tends to drop at larger magnetic inclinations.

At larger inclinations, the magnetic field plays a larger role in the ion trajectories. The magnetic field changes the IEAD considerably as seen in Fig. 4.4. The two distinct IEAD peaks seen at low magnetic inclination angles collapse into one. Additionally, large magnetic field inclinations demonstrate interesting kinetic effects discussed in Sec. 4.3.

Magnetic fields parallel to the wall have a stronger effect on the ion gyromotion. As the ion stream approaches the wall, the ions are turned back along their ion gyro orbit with a fraction of the ion stream glazing off the wall without impact. This ion gyromotion reduces the sheath ion flux impacting on the wall. The reduced flux translates directly into a reduction in the sputtered fluence.

Additionally, at larger magnetic inclinations, the IEAD is shifted towards larger impact angles. As the sputtering yield is nonlinear, the sputtering yield decreases for ions impacting at larger impact angles. Combined with the ion kinetic effects, we see a drop in sputtered fluence as the magnetic inclination increases. The best configuration is found to be with a $\psi = 80°$

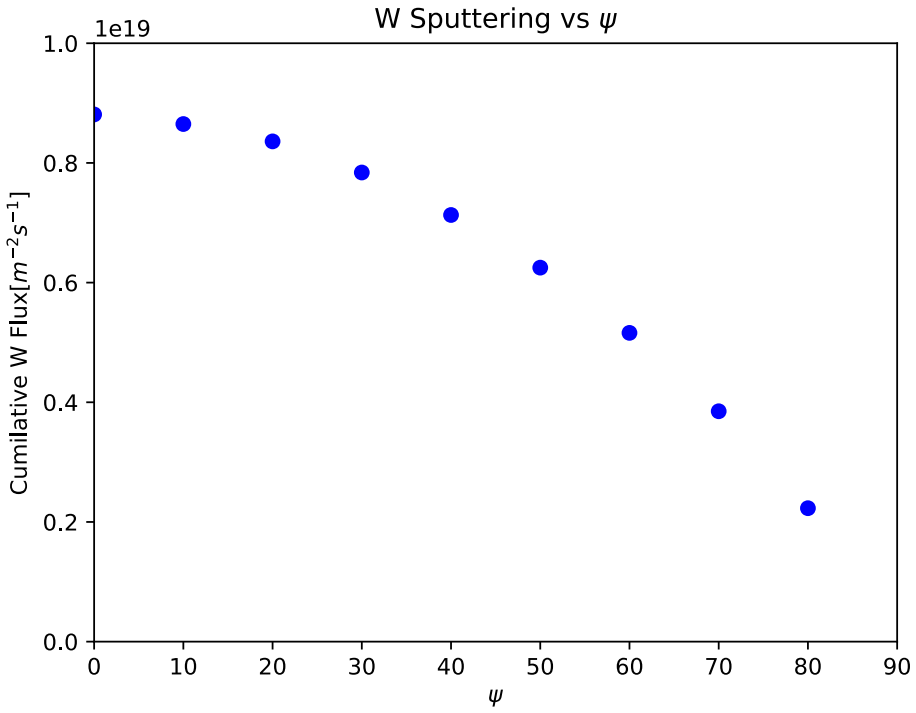

Figure 5.8: Sputtered W impurity flux vs magnetic field angle. The simulations ran for case with $\omega = 16$ MHz, $V_{pp} = 200$ V and varying ψ. Model presented in Fig. 4.1 with wall material made of W and plasma mixture of 95% D^+ ions and 5% O^+ ions. The x-axis represents the magnetic inclination with respect to the normal in Degrees.

that represents a field aligned antenna. This is consistent with experimental results found in Alcator C-MOD [6].

Sputtered fluence vs RF frequency

The final tuning parameter considered in this thesis is the RF frequency ω. RF frequency ω affects the regime of ion mobility and thus the IEAD and incoming particle flux as discussed in Sec. 5.4. We analyze the effects of ω on the sputtered fluence by scanning over the range of ω.

We chose values $\omega = 0, 8, 16, 24, 32, 30, 48, 54, 64$ MHz to span cases capturing the different ion mobility regimes. The cases cover the range of

ICRH operation, 40-55 MHz, planned for ITER . Additionally, the cases overlap with the characteristic ion plasma and cyclotron frequencies, $\omega_{pi} = 32$ MHz and $\omega_{ci} = 8$ MHz. The case of $\omega = 0$ represents classical sheaths. The cases cover the range of high, medium and low ion mobility. A constant magnetic field angle $\psi = 0°$ and peak to peak wall bias $V_{pp} = 200$ V are adapted.

The effect of ω and ion mobility on the instantaneous impacting ion flux, the instantaneous sputtering yield and the instantaneous sputtered flux is discussed in Sec. 5.4. However, as the RF phase periods vary, we compared the sputtered fluence over a time period of $1\mu s$ to average out for the difference in RF phase periods.

Fig. 5.9 shows the sputtered fluence for a time period of $1\mu s$ vs ω in MHz. At low frequencies $\omega < 32$ MHz, the RF wall bias oscillates at a slower pace compared to the ion plasma frequency. The ions have a high mobility and respond to the changes in potential drop promptly. The sputtered fluence peaks at the characteristic ion cyclotron frequency $\omega = \omega_{ci} = 8$ MHz

Fig. 5.9 showed that while a slight initial decrease in sputtered fluence is seen at frequencies higher than 8 MHz, the amount of sputtered fluence quickly plateaus for $\omega \geq 32$ MHz. At frequencies $\omega \geq 32$ MHz, the majority of the ion mobility is lost and the ions see an average potential drop to fall through. Any further loss in ion mobility has no effect on the sputtered fluence. Additionally, the sputtered fluence is independent of the RF frequency over the range $40 - 55$ MHz that ITER operates in.

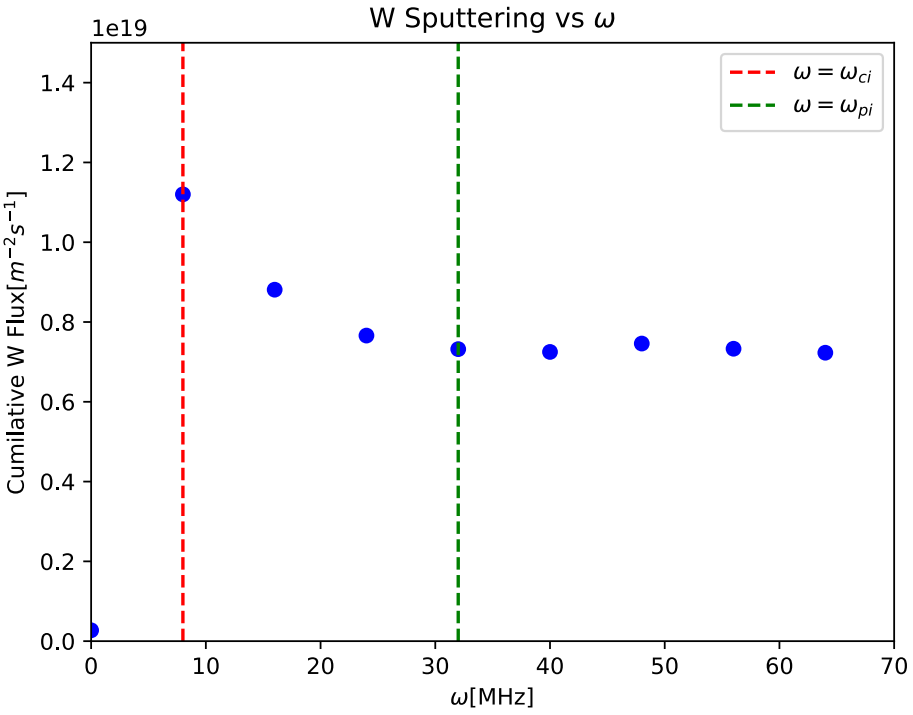

Figure 5.9: Sputtered W impurity flux vs RF frequency. The simulations ran for case with $\psi = 0°$, $V_{pp} = 200$ V and varying $\omega = 16\,, 32\,, 48\,, 64$ MHz. Model presented in Fig. 4.1 with wall material made of W and plasma mixture of 95% D^+ ions and 5% O^+ ions.

5.6 The dependence of sputtering impurity distribution on RF sheath parameters

The effect of sputtered impurities on the total impurity content in the plasma core depends on the kinetic distribution of the particles that leave the antenna faraday screen. The particles can flow into the plasma core or be promptly redeposited. Additionally, the kinetic description can be used by external codes to evaluate the contamination of the upstream plasma and the potential transport to the plasma core.

Fig. 5.10 shows the Energy-Angle distribution (EAD) for different operational parameters in nine sub-figures. We provided the scan over $V_{pp} = 10, 100, 200$ V, magnetic angle $\psi = 0°, 30°, 60°, 80°$ and the RF frequency $\omega = 16\,, 32\,, 48\,, 64$ MHz. The nine subplots are presented in three rows. Each row of sub-figures changes one of the three parameters, V_{pp}, ψ, ω, while keeping the other two constant.

For each of the nine sub-figures, the X-axis and Y-axis are the inclination angle Θ[deg] and energy E_s[eV] of the particles sputtered from the surface. Note that Θ[deg] is measured differently than the magnetic inclination angle ψ or the ion impact angle θ used in Chapter 4. The sputtered angle Θ[deg] is measured with respect to the antenna Faraday screen. The angle Θ[deg] is the classical β angle used in sputtering codes [12].

The EAD of the sputtered particles shown in Fig. 5.10 is independent of the RF sheath parameters. Instead, the EAD is a function of material properties such as surface binding energy. The EAD of sputtered particles represents particles being emitted along oblique trajectories, with the majority of the particles emitted with energies $E_s < 5$ eV.

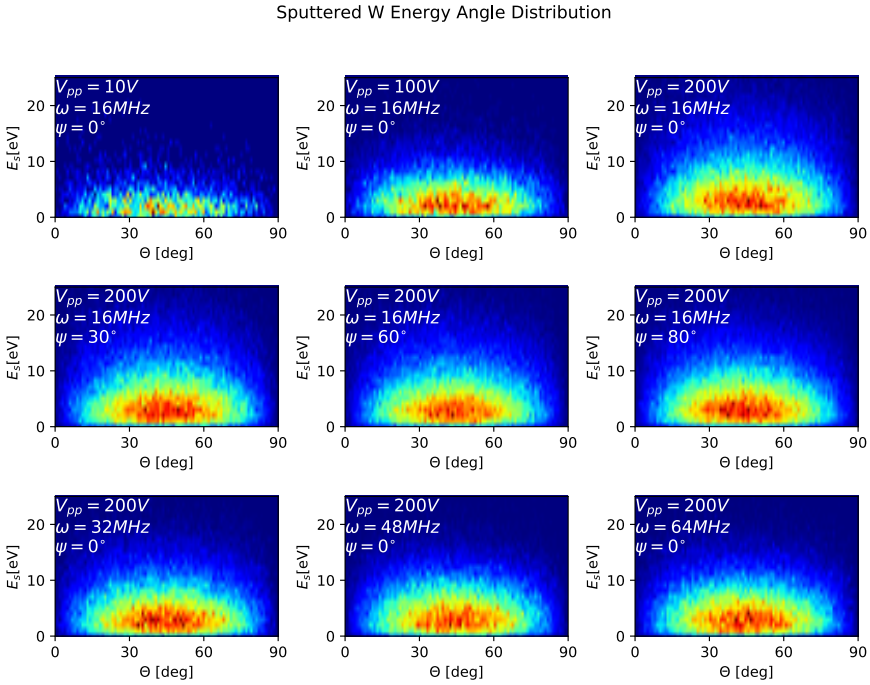

Figure 5.10: Sputtered W impurity flux Energy Angle distribution. The simulations ran for case various combinations of $\psi = 0°, 30°, 60°, 80°$, $V_{pp} = 10, 100, 200$ V and varying $\omega = 16\,, 32\,, 48\,, 64$ MHz. Model presented in Fig. 4.1 with wall material made of W and plasma mixture of 95% D^+ ions and 5% O^+ ions. The X-axis and Y-axis are the inclination angle Θ[deg] and energy E_s[eV] of the particles sputtered from the surface. Note that Θ[deg] is measured differently than the magnetic inclination angle ψ or the ion impact angle θ used in Chapter 4. The angle Θ[deg] is the classical β angle used in sputtering codes [12]. The nine subplots are presented in three rows. Each row of sub-figures changes one of the three parameters, V_{pp}, ψ, ω, while keeping the other two constant.

5.7 Discussion

Several parameters affect the operation of ICRH devices in future tokomak devices. These parameters affect several aspects of Tokomak operations. The peak to peak antenna bias determines the heating power delivered, the RF frequency determines the location of power delivery and the magnetic field alignment determines the coupling efficiency.

Choosing the optimal operating parameters, for sputtering reduction and power delivery purposes, has to factor in the interplay between the parameters. A quantifiable comparable material emission metric has to be calculated for the proposed parameter combinations. In order to quantify material emission consequent to ion bombardment, the hPIC framework was interfaced to the RustBCA sputtering code. Time resolved coupling allowed us to inspect changes in sputtering yield during each RF cycle and evaluate the cumulative sputtered flux for 1 μs. Using the cumulative sputtered flux for 1 μs as our material emission evaluation metric our simulations showed that:

- The peak to peak antenna wall bias V_{pp} heavily affects the sputtering yield as a consequence of the exponential dependence of sputtering vs. energy across the sputtering threshold. During part of the RF cycle the ions impact the wall at energies equivalent to V_{pp}. Larger V_{pp} lead to an increase in the impact energy and in the cumulative sputtered flux. The antenna wall bias should be optimized between the heating power delivery requirement and impurity emission constraints.

- The magnetic field angle, dictated by the antenna alignment, plays a role in kinetic ion dynamics. A field aligned antenna decreases the impacting ion flux, reduces the sputtering yield by decreasing the impact energy and increasing the impact angle. Field aligned antennas are

optimal for the reduction of sputtered impurity emission.

- The RF frequency determines the ion mobility and the nonlinear evolution of the sputtering yield during each RF cycle. The largest amount of sputtering occurs when the RF frequency ω equals the ion cyclotron frequency $\omega = \omega_{ci}$. Cumulative sputtered flux is independent of ω above the plasma frequency threshold $\omega > \omega_{pi}$. The cumulative sputtered flux has been found to be independent of ω in the range of ITER operation, 40-55 MHz.

CHAPTER 6

VALIDATION AGAINST SPECTRAL RADIANCE MEASUREMENTS ON THE WEST TOKAMAK

An important step in establishing the reliability and trust worthiness of our integrated hPIC-RustBCA model is comparing it against experimental data in a validation step. The nature of ICRH impurity sputtering has made experimental data hard to obtain. ICRH sputtering is a local phenomenon with plasma parameters (n_e, T_e) and local impurity density requiring a dedicated spectroscopy experimental campaign to investigate.

For the purpose of validation, the experimental data was acquired from the recent diagnostics campaign performed at the WEST tokamak, at CEA, France. WEST recently underwent an experimental campaign [11] to investigate the effects of ICRF and Lower Hybrid Antennas on limiter and plasma sputtering. US WEST-PMI Team and WEST spectroscopy group have performed an experimental campaign with great levels of data collection using antennas coated with W, shown in Fig 1.3. WEST collected data on the plasma parameters (n_e, T_e) using a Reciprocating Collector Probe (RCP) hosting both a triple Langmuir probe and a Mach probe. Power scans were performed, providing the radial profiles of electron densities n_e and temperature T_e, both necessary inputs to our codes.

6.1 WEST Experiment Data

WEST, formerly known as Tora Supra, is a French tokamak device operated by CEA with a major radius of 2.5 m, a minor radius of 0.5 m and a magnetic field of 3.7 T. WEST protects the RF actuators with W/Mo/CFC coated limiters. The limiters are coated with 100 μm thick W layer. Fig. 6.1 demonstrates the CAD design of the limiters used in the experimental campaign. The limiter has 30 tiles. As part of the C4 experimental campaign, experiments were run at WEST with the goal of diagnosing and quantifying the amount of impurities produced by the antenna limiters when operated with lower-hybrid current drive and ICRH heating.

Lines of sight targeting the limiters and measuring optical spectroscopy of impurities from the limiter[49] were deployed using an endoscope and mirrors.

In addition, a reciprocating probe was used to measure the radial electron temperature and density profiles. This spectroscopic arrangement combined with reciprocating probe data provided by WEST CEA team has provided an excellent well diagnosed validation target for our model.

6.2 Magnetic Configuration

The magnetic equilibrium for the experimental run was provided by WEST in terms of magnetic flux surfaces. The magnetic flux scan provided for the experimental run corresponds to shot 54696 using RF heating power of 2 MW. Fig. 6.2 show the magnetic flux surfaces for the experimental run. The tile centers of the limiter, shown in Fig. 6.1, are overlaid as red dots over the magnetic surfaces.

The magnetic flux was processed to extract the magnetic field magnitude and angle at each of the 30 tile centers. The total magnetic field profile, and

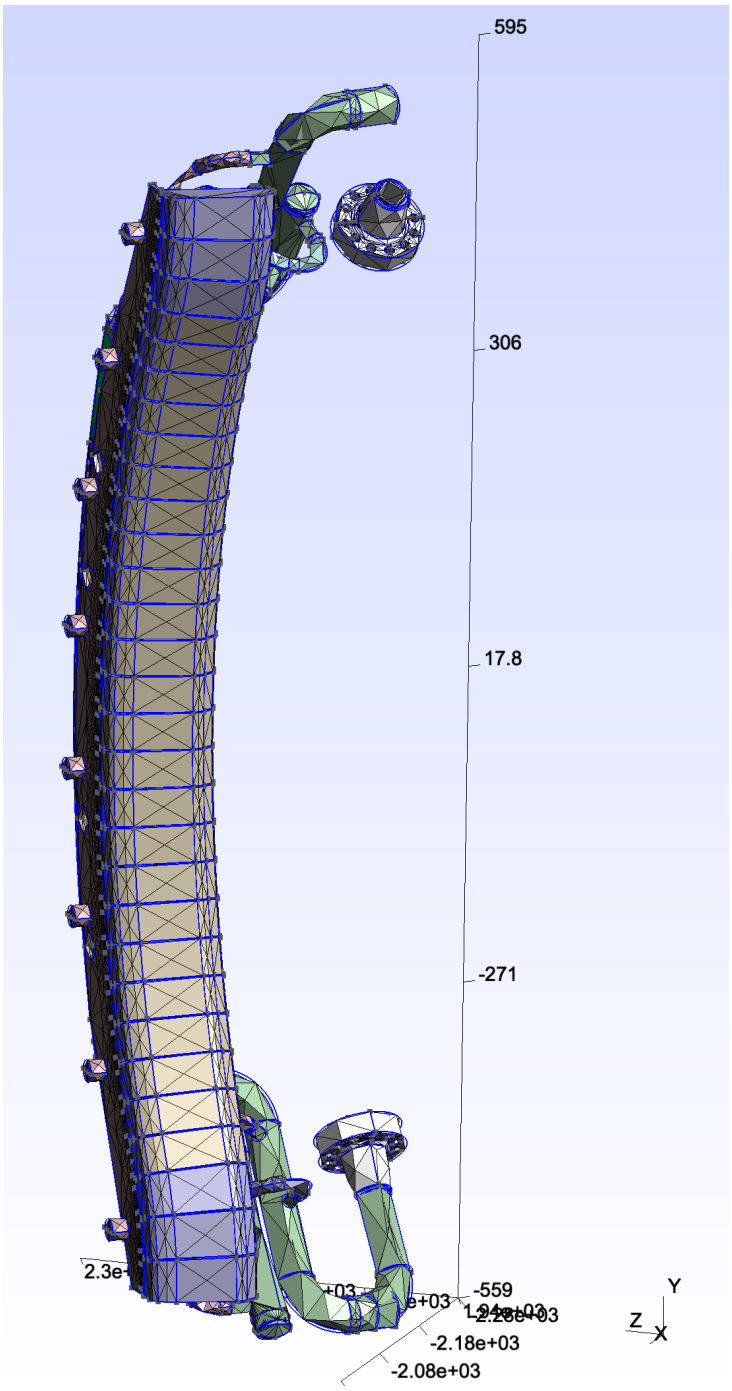

Figure 6.1: CAD Design of the Limiters deployed by WEST. Thanks to the WEST team, CEA.

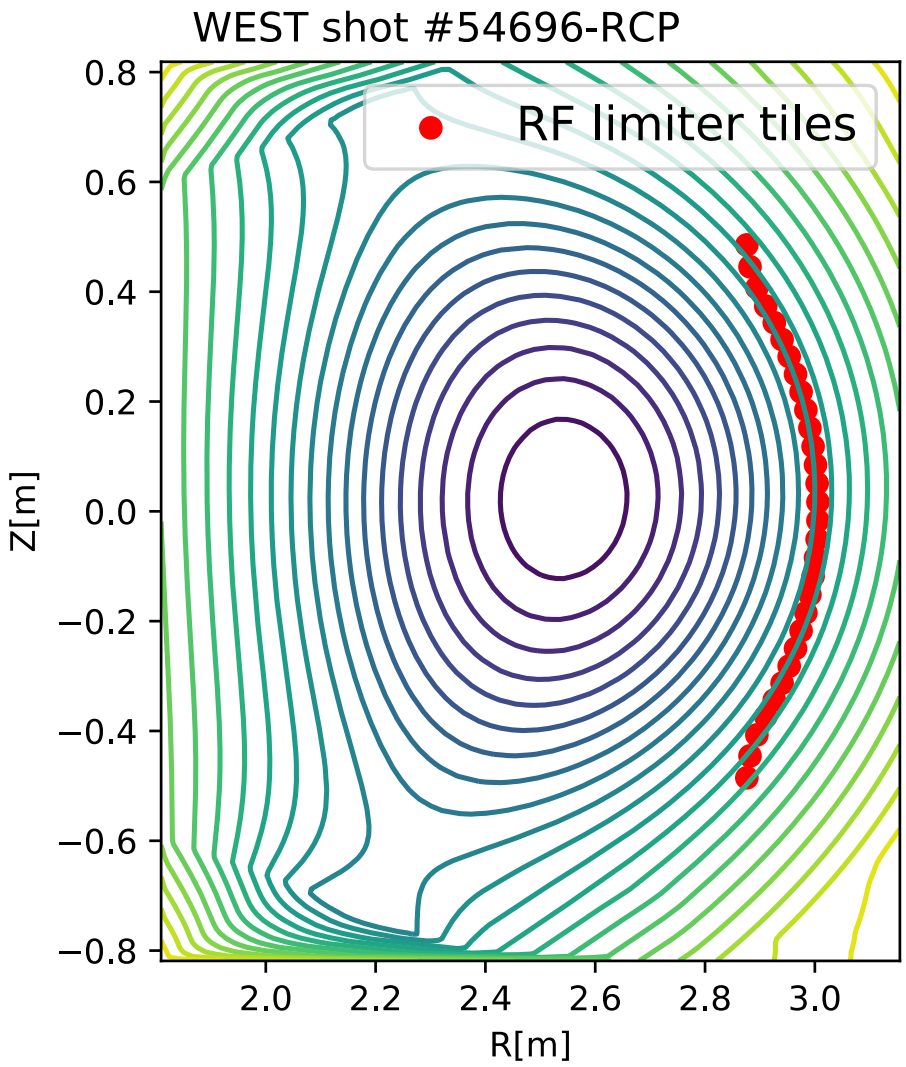

Figure 6.2: Magnetic flux surface for shot 54696 RCP in WEST. The experimental run was performed using 2 MW of Heating power. RF limiter tile centers overlaid in red over the magnetic surfaces.

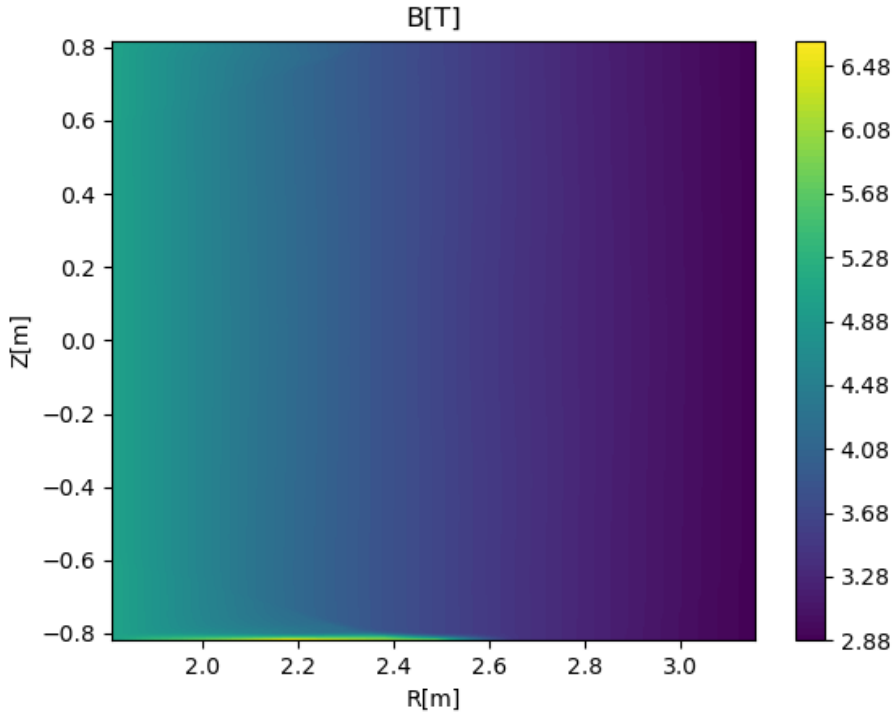

Figure 6.3: Magnetic field B[T] configuration used for Experimental Shot 54696 in WEST. The experimental run was performed using 2 MW of Heating power.

individual vector components, are shown in figures 6.3-6.6. Magnetic fields on the tile centers ranged around 3.05-3.17[T] and magnetic angles ranged $66.3° - 70.15°$. The magnetic field magnitude and angle were provided as inputs to hPIC.

6.3 Tile Densities and Temperatures

Simulating the sputtering infront of the RF limiter tiles requires prior knowledge of plasma conditions for each tile. Reciprocating probes were used to provide a radial profile of the electron density and temperature in front of the limiter. The radial profiles were linked to the tile centers through continuous magnetic flux line tracing.

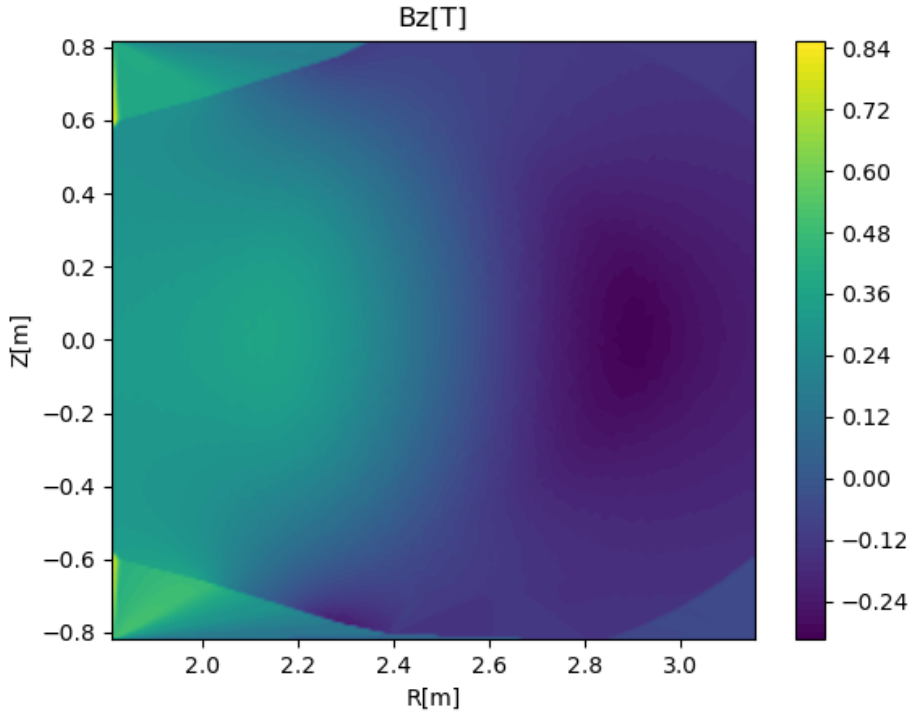

Figure 6.4: Magnetic field component along the vertical Z-axis of the tokomak $B_z[T]$ used for Experimental Shot 54696 in WEST. The experimental run was performed using 2 MW of Heating power.

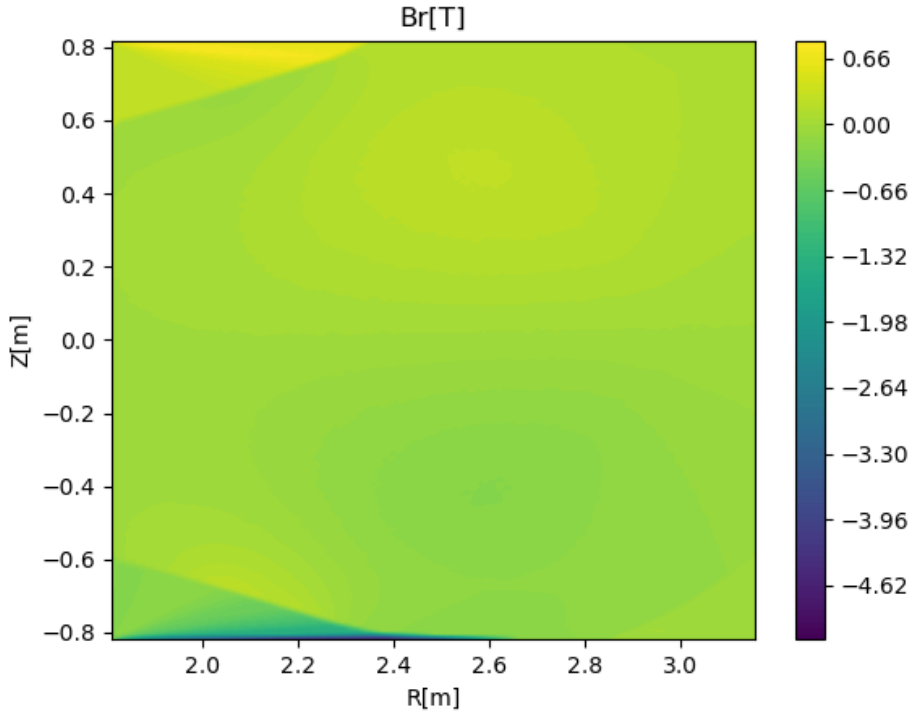

Figure 6.5: Magnetic field component along the horizontal R-axis of the tokomak $B_r[T]$ used for Experimental Shot 54696 in WEST. The experimental run was performed using 2 MW of Heating power.

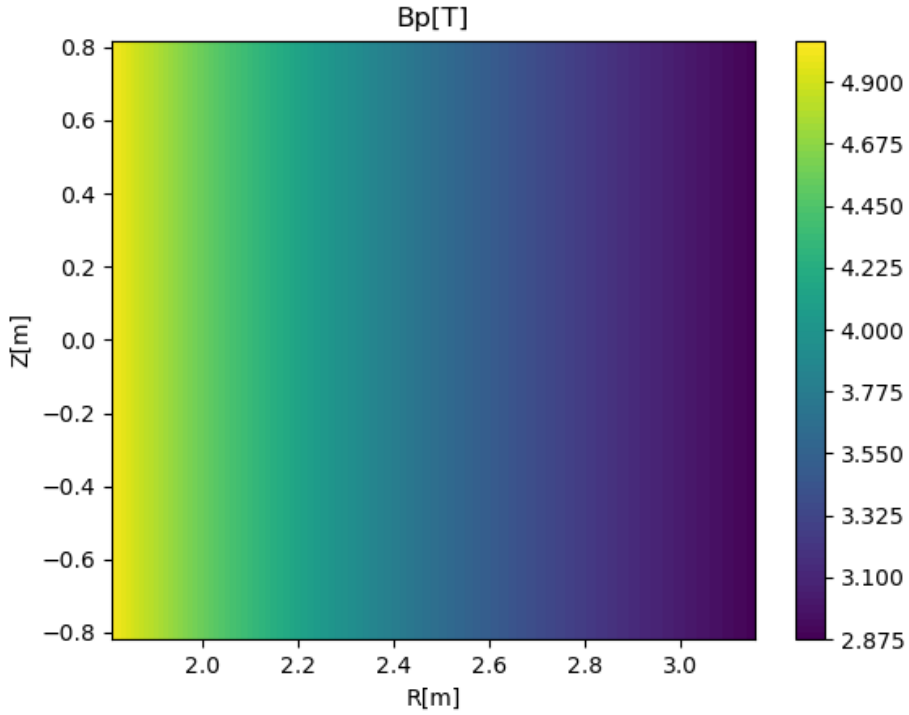

Figure 6.6: Magnetic field component along the poloidal component of the tokomak $B_p[T]$ used for Experimental Shot 54696 in WEST. The experimental run was performed using 2 MW of Heating power.

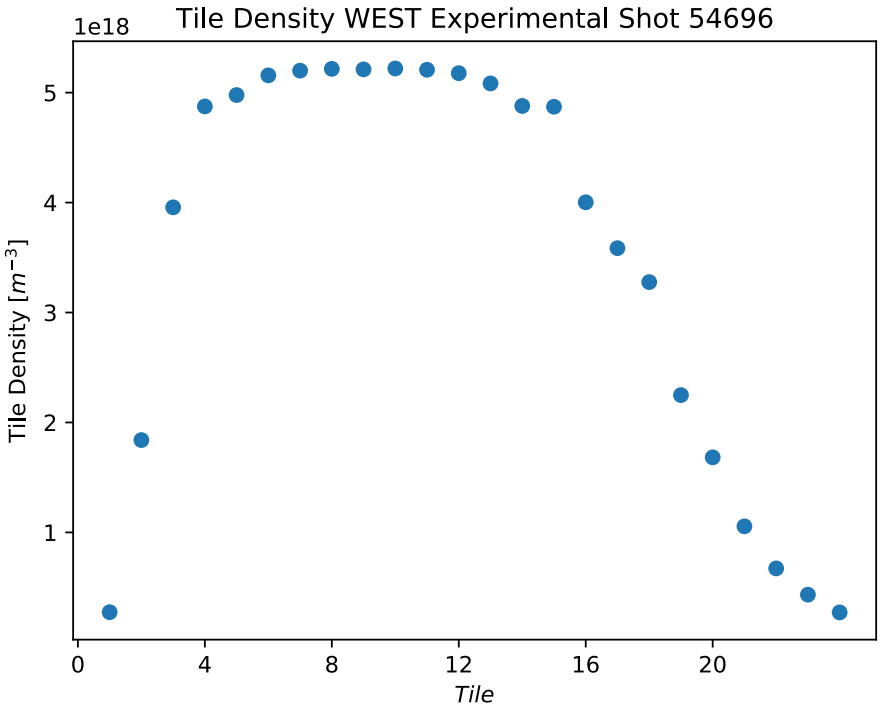

Figure 6.7: Electron density profile for the simulated tiles. Densities at tiles centers extracted from RCP data for the experimental run shot 54696.

The magnetic field lines connecting to the tile centers can be seen in Fig. 6.2. The gathered experimental data covers the first 24 tiles from top to bottom in Fig. 6.1. The density and temperature profiles for the simulated tiles is provided in Fig. 6.8. As the density and temperature profiles peak around the center tiles (Tiles 8-12) we expect the highest sputtering to come from the center tiles.

6.4 Sources of Uncertainties

WEST shot 54696 had a clear signature of the tungsten WI 4008 Å emission line, where the absolute spectral radiance [Ph m^{-2} s^{-1} sr^{-1}] emitted by the sputtered impurities across the whole RF limiter was recorded. This provides

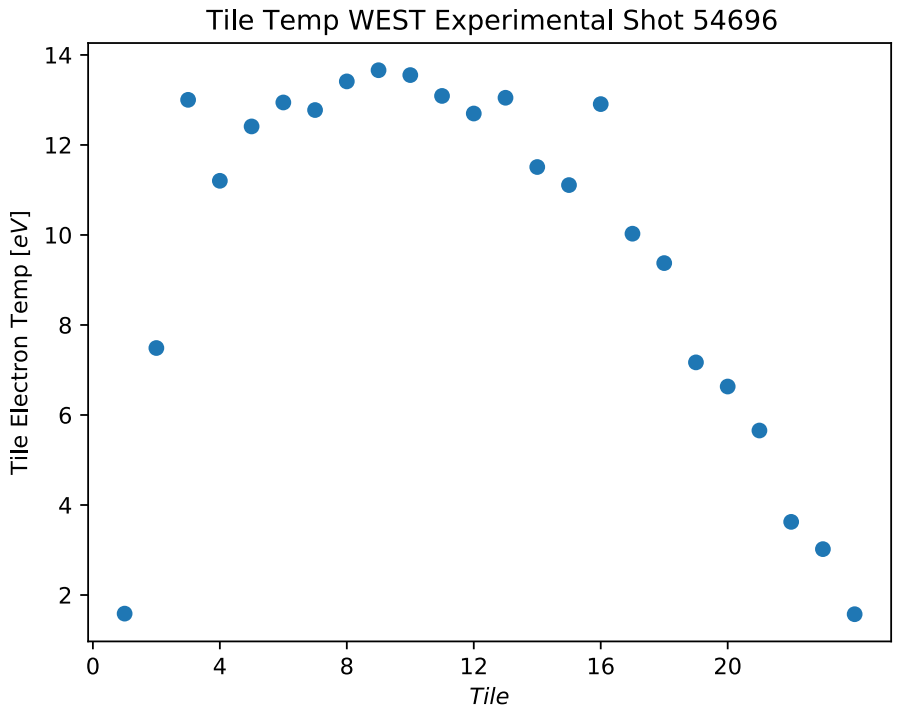

Figure 6.8: Electron temperature profiles for the simulated tiles. Temperatures at tiles centers extracted from RCP data for the experimental run shot 54696.

an excellent validation target for our simulations. The plasma conditions (n_e electron density, T_e electron temperature) and magnetic field configurations were well diagnosed, enabling the simulation of the sputtered flux across the tile centers.

Using the plasma conditions and magnetic field configurations, we performed simulations of the sputtered W impurity flux along the vertical Z-axis. However, three main sources of uncertainties have been identified before comparison with experimental data. Namely, (1) the inverse photon efficiency, also known as the S/XB ratio, (2) the distribution of higher charge states (e.g. O^{+}, O^{2+}, O^{3+}, ..., O^{8+}), and (3) the atomic composition of the impurities (O, C, F, Cu, etc.) in front of the limiter. In the following considerations we will use oxygen as the most-abundant equivalent impurity.

Inverse Photon Efficinecy, S/XB

While the sputtered flux is not available experimentally to compare against, the radiance [Ph m^{-2} s^{-1} sr^{-1}] produced by the sputtered W flux was measured. The radiance [Ph m^{-2} s^{-1} sr^{-1}] of the WI 4008 Å emission line was scanned over the RF limiter vertical axis Z[m] providing the radiance [Ph m^{-2} s^{-1} sr^{-1}] vs Z[m]-axis profile for experimental validation. We converted our simulated sputtered W flux Γ_W into radiance I_W [Ph m^{-2} s^{-1} sr^{-1}] using Eq. 6.1[50]:

$$I_W = \frac{\Gamma_W}{4\pi(SXB)} \tag{6.1}$$

where S/XB is the number of ionization events per photon, or inverse photon efficiency. S/XB data is a function of the electron temperature and density, as well as sputtered material. The S/XB data can be fetched from several independent different experiments and methods including weight loss [50]

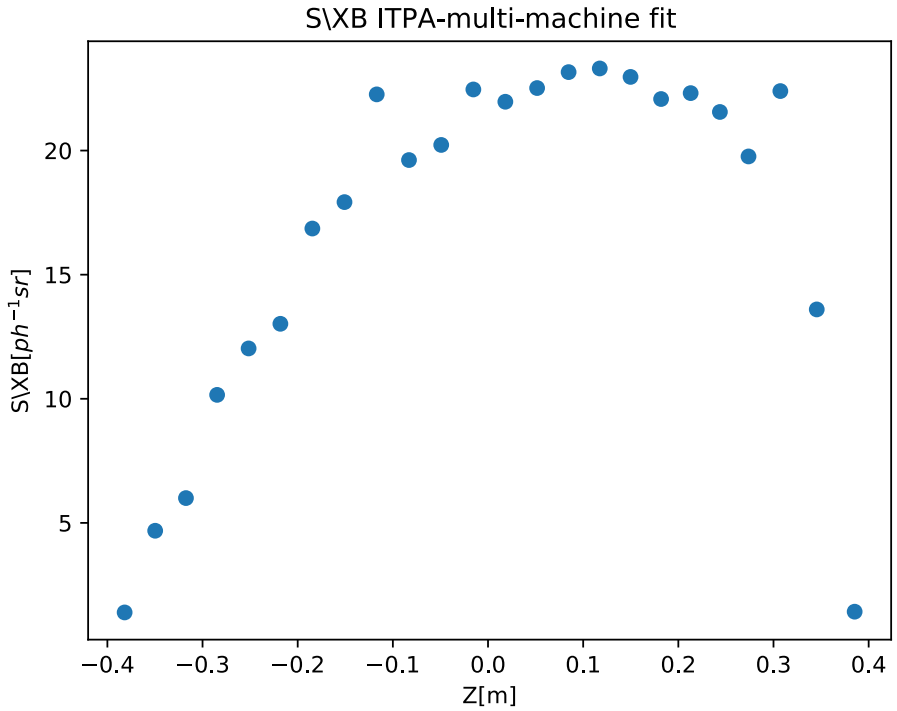

Figure 6.9: Electron temperature profiles for the simulated tiles. Temperatures at tiles centers extracted from RCP data for the experimental run shot 54696.

in PISCES-B, evaporation in ASDEX Upgrade [51]. Additionally, Atomic Data and Analysis Structure (ADAS) provides multi-machine experimental data for the S/XB[52]. The uncertainties in S/XB data can reach an order of magnitude. Choosing the S/XB data source depends on the device and plasma conditions.

For the purpose of this thesis and validation, we chose a multi-machine S/XB fit as the best option. A multi-machine S/XB data fit for the Tungsten W impurity, called ITPA [53], is available in the literature. Using the experimentally measured electron density and temperature in combination with the ITPA multi-machine fit, the S/XB profile along the vertical Z-axis was calculated and illustrated in Fig. 6.9.

Oxygen charge state distribution

The spectroscopic lines of sight, discussed in Sec. 6.1, provided a scan of the line emission intensity over the vertical position of the tokamak, Z[m] in Fig. 6.3. Spectroscopic measurements indicated the presence of an oxygen impurity in the plasma sheaths.

However, the charge of O impurity particles was not diagnosed. For the purpose of this validation, we assume a range of O^{4+}-O^{8+} ion impurity was present in the plasma and makes 5% of the plasma density. We adopted the upper limit of 5% oxygen impurity density in our simulation as the conservative estimate. As the exact distribution of impurity in the plasma is unknown, we repeated the simulations using five different O ion impurity charges ,O^{4+}, O^{5+}, O^{6+} O^{7+} O^{8+}, to provide a lower estimate and an upper estimate on the sputtered impurity flux.

6.5 W Impurity Flux Calculated via hPIC-RustBCA

In order to validate hPIC-RustBCA framework, we simulated the sputtered flux of impurities generated from the limiter due to the limiter's interaction with the plasma sheath. Twenty-four simulations representing the first 24 tiles in the WEST limiter were performed. The simulations emulated the experimental conditions by using the experimentally determined magnetic field angle and magnitude, the plasma electron temperature and density at the tile centers, a Deuterium plasma species and a Tungsten W limiter material. Additionally, the plasma was found to contain an oxygen impurity in the D plasma. Five different O ion impurity charges ,O^{4+}, O^{5+}, O^{6+} O^{7+} O^{8+}, were simulated.

The simulation domain is shown in Fig. 4.1. It is a dual plate system

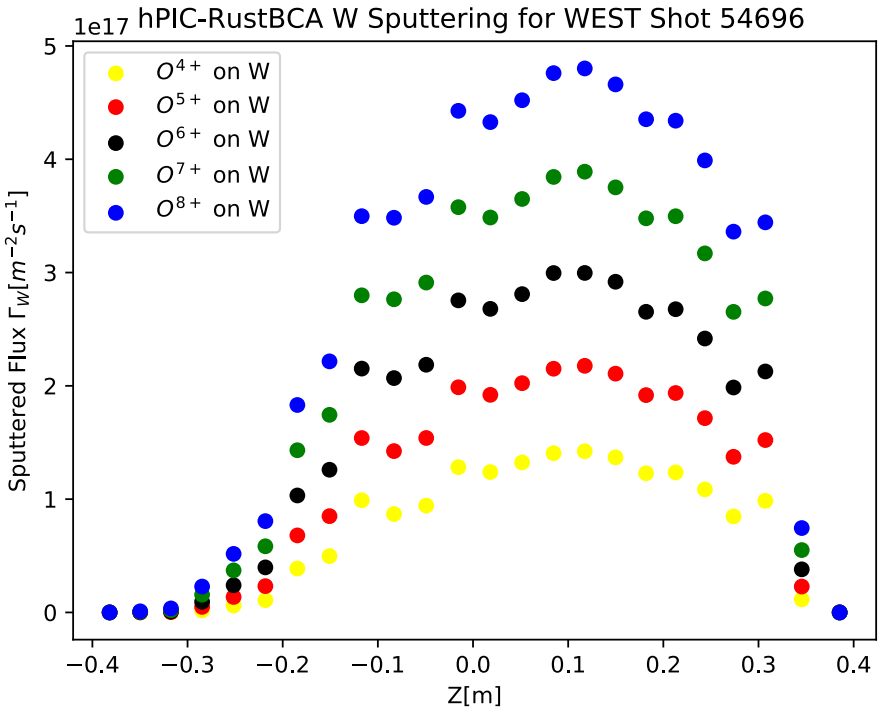

Figure 6.10: Simulated sputtered W flux Γ_W $[m^{-2}s^{-1}]$ from the WEST limiter vs vertical Z-axis[m]. Simulations emulated the experimental conditions by using the experimentally determined magnetic field angle and magnitude, the plasma electron temperature and density for the experimental run shot 54696.

with a magnetic field angle ψ evaluated with respect to the wall normal. The walls are biased using $V_{pp} = 0$ V, as the WEST limiter tiles are not electrically connected to the RF antenna. The 1-D computational domain has a size of 200 Debye lengths and is divided into 400 computational nodes. The simulation time was set for twice the ion transit time.

6.6 Comparison against measured spectral radiance

Fig. 6.11 presents the main results of the validation attempt. The simulated sputtered W flux Γ_w was converted into radiance using Eq. 6.1. The simulations performed using O^{7+} and O^{8+} ion impurities provide the best agree-

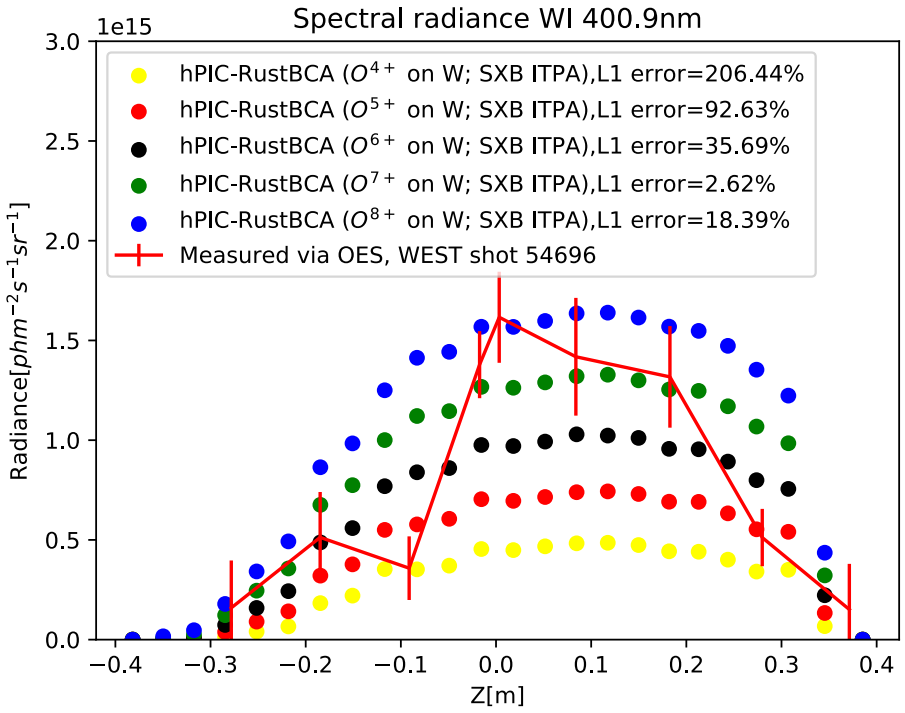

Figure 6.11: Validation of hPIC-RustBCA framework with experiment data from WEST shot 54696.

ment with the experimental results quantitatively and qualitatively. While the exact plasma impurity content in the experimental WEST shot 54696 is unknown, any impurity mixture of O^{7+} impurity and O^{8+} impurity will fall within the range set by the two simulations. As most experimental data points fall within the range set by two simulations, O^{7+} impurity and O^{8+} impurity, the validation exercise has successfully provided trust in the hPIC-RustBCA framework.

In conclusion, The validation exercise provided trust in the hPIC-RustBCA framework that can now be used to investigate the effects of different RF field conditions on the impurity sputtering and other PMI.

CHAPTER 7

SUMMARY, CONCLUSIONS AND FUTURE WORK

In summary, this thesis discusses the mitigation of enhanced impurity sputtering due to Ion Cyclotron Resonance Heating (ICRH). Chapter 1 provided the reader with the background and literature review associated with the ICRH. The need for ICRH, the emergence of RF sheaths and the enhanced sputtering that is associated with RF sheaths were discussed. Finally, based on the state of literature, the justification and need for a new RF sheath code capable of simulating kinetic ions was provided.

Chapter 2 detailed the development of the hybrid Particle-In-Cell(PIC) model used in this thesis. The hybrid model simulates the ions using kinetic PIC method and the electrons are approximated as Boltzmann electrons. Boltzmann electrons allow efficient hybrid PIC plasma simulations, applicable to all cases where the electron behavior can be approximated to an inertia-less charged fluid balancing the electrostatic and pressure forces. However, the numerical implementation of Boltzmann electrons requires to solve for a non-linear Poisson problem, plus an additional condition enforcing global charge conservation for the calculation of the reference Boltzmann density. In time-dependant problems, such as radio-frequency sheaths or other low-frequency transient phenomena, the correct normalization of the reference Boltzmann density requires a self-consistent numerical scheme.

In Chapter 2, we presented an explicit scheme which was used to naturally enforce global charge conservation in our PIC simulations with Boltz-

mann electrons. The scheme directly follows from a general expression of charge conservation, and has the innovative property of being local in time, thus avoiding artificial filtering typical of previous explicit schemes [7]. The scheme was developed to enable the simulation of transient plasma sheaths. The scheme was tested for both steady-state plasma sheaths and time-dependent RF sheaths, with results in agreement with theoretical expected values.

In Chapter 3 we preformed extensive numerical testing of hPIC and Benchmarking hPIC framework in RF conditions. Primary quantities of interest for benchmarking included the upstream RF voltage rectification and the RF sheath admittance. We compared hPIC results with results from NoFlu, a well established RF sheath code that simulates the plasma using fluid ions and Boltzmann electrons. The comparison spanned a range of RF parameters and included cases with high and low RF frequencies, positive and negative net DC current. An excellent agreement with NoFlu was found in all compared cases.

In Chapter 4, the hPIC model was used to perform a parametric investigation of the IEAD in RF sheaths, and evaluate the impact of the ion bombardment on the Faraday screen of an ICRH antenna. The model successfully captured the sheath structure, including the magnetic presheath and the Debye sheath, and how the structure varies with different magnetic field angles. RF sheath voltages were successfully captured. Parametric scans were performed as a function of the three main normalized parameters affecting the RF sheath physics, namely: RF peak-to-peak voltage, normalized frequency, and magnetic field angle. The IEAD was found to be highly dependent on frequency and magnetic angle.

In typical tokamak conditions (e.g. the JET-ICRH antenna), the hPIC simulations showed the presence of a cusp in the ion energy-angle distribu-

tion. A detailed analysis of the phase-space indicated the cusp formation is attributed to effect of the ExB drift and the finite-Larmor orbit resulting from the ion gyromotion. In this and similar cases, typified by grazing angle ($\psi = 85°$) and moderately low frequencies, it was shown that the hPIC model enabled a solution that was not accessible in a standard fluid model. The reason was traced to the reflection of ions from the wall back into the plasma, necessitated by the very small electron wall flux at grazing incidence.

In Chapter 5, the hPIC framework was coupled to rustBCA, a binary collision approximation code, to enable the investigation of the effects of changes in IEAD on the sputtered flux. The mechanism of time resolved coupling to rustBCA was discussed in Chapter 5. Time resolved coupling was demonstrated, showing how the instantaneous impacting ion flux, sputtering yield and sputtering flux change during an RF phase. The time resolved coupling showed that the magnitude of sputtered impurities oscillates during an RF phase and that the oscillations are dependent on RF frequency.

The hPIC-RustBCA framework was used to perform a parametric investigation of the sputtered fluence as a function of the three main parameters affecting the RF sheath physics, namely: RF peak-to-peak voltage, RF frequency, and magnetic field angle. The effect of the changes in the IEAD on the sputtered fluence was discussed for all three parameters. Additionally, the hPIC-RustBCA framework showed that the kinetic distribution of sputtered impurities is independent on any RF sheath parameters.

Chapter 6 provided a validation of the complete hPIC-RustBCA framework against experimental data provided by recent WEST experimental campaign. The chapter overviews the plasma sheath conditions measured during the experimental run, specifically during shot 54696. hPIC-RustBCA framework uses the experimentally measured conditions to provide the simulated

sputtered flux and radiance. The simulated radiance was compared with experimentally measured radiance. A good agreement between simulated and experimental results was found. Finally, a discussion on the uncertainties in this validation attempt was provided in Chapter 6.

In addition to allowing the calculation of the sputtered fluence, the kinetic ion, Boltzmann electron PIC simulations presented in the thesis exemplify an important rung in the hierarchy of RF sheath models. Together with the fluid model and fully kinetic ion and electron models, they provide a variety of useful tools for the simulation and analysis of RF sheaths, and advance the prospect of mitigating deleterious RF sheath effects in fusion experiments. We provided a validated tool that can simulate and analyze proposed ICRH RF impurity mitigations strategies in an RF sheath environment using a Particle in cell kinetic ion model coupled to a plasma material interactions code.

Future Work

Further development of the hPIC-RustBCA framework can be beneficial for specific research topics. Beyond the scope of this thesis, the hPIC-RustBCA framework facilitates addressing future research questions. We list several examples of possible future developments and studies that can be done using the hPIC-RustBCA framework:

- Validation of hPIC-RustBCA framework with other fusion devices.
- Coupling of hPIC-RustBCA to global impurity transport codes.
- Analysis of sputtering yield sensitivity to different wall material.

CHAPTER 8

REFERENCES

[1] J. P. Freidberg, *Plasma physics and fusion energy.* Cambridge University Press, 1 2007, vol. 9780521851. [Online]. Available: /core/books/plasma-physics-and-fusion-energy/CD7B530D2889F70446F34E14EE0EF703

[2] P. Chappuis, C. Portafaix, E. Thomas, B. Bertrand, R. Walton, V. Riccardo, R. Baker, I. Barlow, A. Kaye, A. Lorenz, and F. Durodier, "Design of a limiter for the JET EP ICRH antenna," *Fusion Engineering and Design*, vol. 75-79, no. SUPPL., pp. 413–416, 11 2005.

[3] J. M. Bernard, A. Argouarch, G. BergerBy, C. Brun, F. Clairet, L. Colas, C. Dechelle, F. Durodié, M. Firdaouss, F. Ferlay, J. C. Giacalone, J. Hillairet, J. Jacquot, D. Keller, D. Milanesio, M. Missirlian, M. Shannon, and A. Simonetto, "CEA contribution to the ITER ICRH antenna design," *Fusion Engineering and Design*, vol. 88, no. 6-8, pp. 950–955, 2013.

[4] M. L. Garrett and S. J. Wukitch, "Mitigation of radio frequency sheaths through magnetic field-aligned ICRF antenna design," *Fusion Engineering and Design*, vol. 87, no. 9, pp. 1570–1575, 9 2012.

[5] C. M. Qin, Y. P. Zhao, H. Qwang, X. J. Zhang, B. N. Wan, J. M. Noterdaeme, F. Braun, V. Bobkov, H. Kasahara, E. H. Kong, L. Wang, Y. Shuai, Z. X. He, and B. J. Ding, "Experimental investigation of the potentials modified by radio frequency sheaths during ion cyclotron range of frequency on EAST," *Plasma Physics and Controlled Fusion*, vol. 55, no. 1, p. 15004, 1 2013.

[6] S. J. Wukitch, M. L. Garrett, R. Ochoukov, J. L. Terry, A. Hubbard, B. Labombard, C. Lau, Y. Lin, B. Lipschultz, D. Miller, M. L. Reinke, and D. Whyte, "Characterization and performance of a field aligned ion cyclotron range of frequency antenna in Alcator C-Mod," *Physics of Plasmas*, vol. 20, no. 5, p. 56117, 5 2013. [Online]. Available: http://aip.scitation.org/doi/10.1063/1.4803882

[7] G. J. M. Hagelaar, "How to normalize Maxwell–Boltzmann electrons in transient plasma models," *Journal of Computational Physics*, vol. 227, no. 2, pp. 871–876, 12 2007. [Online]. Available: https://www.sciencedirect.com/science/article/pii/S0021999107004329

[8] M. A. M. A. Lieberman and A. J. Lichtenberg, *Principles of plasma discharges and materials processing*. Wiley-Interscience, 2005.

[9] M. Elias, D. Curreli, T. G. Jenkins, J. R. Myra, and J. Wright, "Numerical model of the radio-frequency magnetic presheath including wall impurities," *Physics of Plasmas*, vol. 26, no. 9, 2019.

[10] J. R. Myra, M. T. Elias, D. Curreli, and T. G. Jenkins, "Effect of net direct current on the properties of radio frequency sheaths: Simulation and cross-code comparison," *Nuclear Fusion*, vol. 61, no. 1, p. 016030, 1 2020. [Online]. Available: https://iopscience.iop.org/article/10.1088/1741-4326/abc4c4 https://iopscience.iop.org/article/10.1088/1741-4326/abc4c4/meta

[11] L. Colas, P. Jacquet, V. Bobkov, M. Brix, L. Meneses, K. Kirov, E. Lerche, C. C. Klepper, M. Goniche, A. Křivská, P. Dumortier, and A. Czarnecka, "2D mappings of ICRF-induced SOL density modifications on JET," *Nucl. Fusion*, vol. 57, 2017.

[12] J. Drobny, A. Hayes, D. Curreli, and D. N. Ruzic, "F-TRIDYN: A Binary Collision Approximation code for simulating ion interactions with rough surfaces," *Journal of Nuclear Materials*, vol. 494, pp. 278–283, 10 2017.

[13] J. Drobny and D. Curreli, "RustBCA: A High-Performance Binary-Collision-Approximation Code for Ion-Material Interactions," *Journal of Open Source Software*, 2021.

[14] M. D. Campanell, "PLASMA INTERACTION WITH ELECTRON-EMITTING SURFACES," Ph.D. dissertation, Princeton, 2014. [Online]. Available: https://dataspace.princeton.edu/handle/88435/dsp01cj82k951c

[15] V. V. Bobkov, F. Braun, R. Dux, A. Herrmann, L. Giannone, A. Kallenbach, A. Krivska, H. W. Müller, R. Neu, J. M. Noterdaeme, T. Pütterich, V. Rohde, J. Schweinzer, A. Sips, and I. Zammuto, "Assessment of compatibility of ICRF antenna operation with full W wall in ASDEX Upgrade," *Nuclear Fusion*, vol. 50, no. 3, p. 035004, 2 2010. [Online]. Available: https://iopscience.iop.org/article/10.1088/0029-5515/50/3/035004 https://iopscience.iop.org/article/10.1088/0029-5515/50/3/035004/meta

[16] R. Neu, V. Bobkov, R. Dux, A. Kallenbach, T. Pütterich, H. Greuner, O. Gruber, A. Herrmann, C. Hopf, K. Krieger, C. F. Maggi, H. Maier, M. Mayer, V. Rohde, K. Schmid, and W. Suttrop, "Final steps to an all tungsten divertor tokamak," *Journal of Nuclear Materials*, vol. 363-365, no. 1-3, pp. 52–59, 6 2007.

[17] V. Bobkov, M. Balden, R. Bilato, F. Braun, R. Dux, A. Herrmann, H. Faugel, H. Fünfgelder, L. Giannone, A. Kallenbach, H. Maier, H. W. Müller, R. Neu, J. M. Noterdaeme, T. Pütterich, V. Rohde, N. Tsujii, F. Zeus, and H. Zohm, "ICRF operation with improved antennas in ASDEX Upgrade with W wall," *Nuclear Fusion*, vol. 53, no. 9, p. 93018, 9 2013.

[18] L. Colas, S. Heuraux, S. Brémond, and G. Bosia, "RF current distribution and topology of RF sheath potentials in front of ICRF antennae," *Nuclear Fusion*, vol. 45, no. 8, p. 767, 7 2005.

[19] L. Colas, J. Jacquot, S. Heuraux, E. Faudot, K. Crombé, V. Kyrytsya, J. Hillairet, and M. Goniche, "Self consistent radio-frequency wave propagation and peripheral direct current plasma biasing: Simplified three dimensional non-linear treatment in the "wide" sheath asymptotic regime," *Physics of Plasmas*, vol. 19, no. 9, p. 92505, 9 2012. [Online]. Available: http://aip.scitation.org/doi/10.1063/1.4750046

[20] S. J. Wukitch, B. Lipschultz, E. Marmar, Y. Lin, A. Parisot, M. Reinke, J. Rice, and J. Terry, "RF plasma edge interactions and their impact on ICRF antenna performance in Alcator C-Mod," *Journal of Nuclear Materials*, vol. 363-365, no. 1-3, pp. 491–497, 6 2007.

[21] V. Bobkov, D. Aguiam, R. Bilato, S. Brezinsek, L. Colas, A. Czarnecka, P. Dumortier, R. Dux, H. Faugel, H. Fünfgelder, P. Jacquet, A. Kallenbach, A. Krivska, C. C. Klepper, E. Lerche, Y. Lin, D. Milanesio, R. Maggiora, I. Monakhov, R. Neu, J. M. Noterdaeme, R. Ochoukov, T. Pütterich, M. Reinke, W. Tierens, A. Tuccilo, O. Tudisco, D. Van Eester, J. Wright, S. Wukitch, and W. Zhang, "Impact of ICRF on the scrape-off layer and on plasma wall interactions: From present experiments to fusion reactor," *Nuclear Materials and Energy*, vol. 18, pp. 131–140, 1 2019.

[22] S. A. Cohen, S. Bernabei, R. Budny, T. K. Chu, P. Colestock, E. Hinnov, W. Hooke, J. Hosea, D. Hwang, F. Jobes, D. Manos, R. Motley, D. N. Ruzic, J. Stevens, B. Stratton, S. Suckewer, S. Goeler, and R. Wilson, "Plasma-material interactions during rf experiments in tokomaks," *Journal of Nuclear Materials*, vol. 128-129, pp. 280–291, 1984.

[23] J. R. Myra, D. A. D'Ippolito, and M. J. Gerver, "Faraday screen sheaths and impurity production during ion cyclotron heating," *Nuclear Fusion*, vol. 30, no. 5, pp. 845–858, 1990. [Online]. Available: http://stacks.iop.org/0029-5515/30/i=5/a=004?key=crossref.6d1672cb4d651ee6a6b3685b2b7cbf9f

[24] J. R. Myra, "Physics-based parametrization of the surface impedance for radio frequency sheaths," *Physics of Plasmas*, vol. 24, no. 7, p. 72507, 7 2017. [Online]. Available: http://aip.scitation.org/doi/10.1063/1.4990373

[25] P. Jacquet, L. Colas, M.-L. Mayoral, G. Arnoux, V. Bobkov, M. Brix, P. Coad, A. Czarnecka, D. Dodt, F. Durodie, A. Ekedahl, D. Frigione, M. Fursdon, E. Gauthier, M. Goniche, M. Graham, E. Joffrin, A. Korotkov, E. Lerche, J. Mailloux, I. Monakhov, C. Noble, J. Ongena, V. Petrzilka, C. Portafaix, F. Rimini, A. Sirinelli, V. Riccardo, Z. Vizvary, A. Widdowson, K.-D. Zastrow, and J. E. T. E. Contributors, "Heat loads on JET plasma facing components from ICRF and LH wave absorption in the SOL," *Nuclear Fusion*, vol. 51, no. 10, p. 103018, 8 2011.

[26] Y. Corre, M. Firdaouss, L. Colas, A. Argouarch, D. Guilhem, J. Gunn, C. Hamlyn-Harris, J. Jacquot, M. Kubic, X. Litaudon, M. Missirlian, M. Richou, G. Ritz, D. Serret, and K. Vulliez, "Characterization of heat flux generated by ICRH heating with cantilevered bars and a slotted box Faraday screen," *Nuclear Fusion*, vol. 52, no. 10, p. 103010, 8 2012.

[27] L. Colas, L. Costanzo, C. Desgranges, S. Br mond, J. Bucalossi, G. Agarici, V. Basiuk, B. Beaumont, A. B coulet, and F. Nguyen, "Hot spot phenomena on Tore Supra ICRF antennas investigated by optical diagnostics," *Nuclear Fusion*, vol. 43, no. 1, pp. 1–15, 1 2003. [Online]. Available: http://stacks.iop.org/0029-5515/43/i=1/a=301?key=crossref.b3d4f4ca1420a710efdf7a601ed13259

[28] C. C. Klepper, D. Borodin, M. Groth, A. Lasa, M. Airila, V. Bobkov, L. Colas, P. Jacquet, A. Kirschner, A. Terra, T. M. Biewer, E. Delabie, C. Giroud, and J. E. T. Contributors, "Estimates of RF-induced erosion at antenna-connected beryllium plasma-facing components in JET," *Physica Scripta*, vol. 2016, no. T167, p. 14035, 1 2016.

[29] J. M. Noterdaeme and G. V. Oost, "The interaction between waves in the ion cyclotron range of frequencies and the plasma boundary," *Plasma Physics and Controlled Fusion*, vol. 35, no. 11, pp. 1481–1511, 11 1993. [Online]. Available: https://iopscience.iop.org/article/10.1088/0741-3335/35/11/001

[30] D. A. D'Ippolito and J. R. Myra, "ICRF-edge and surface interactions," *Journal of Nuclear Materials*, vol. 415, no. 1 SUPPL, p. S1001–S1004, 8 2011. [Online]. Available: https://www.sciencedirect.com/science/article/pii/S0022311510004307

[31] E. Kawamura, V. Vahedi, M. A. Lieberman, and C. K. Birdsall, "Ion energy distributions in rf sheaths; review, analysis and simulation," *Plasma Sources Science and Technology*, vol. 8, no. 3, p. R45–R64, 8 1999. [Online]. Available: http://stacks.iop.org/0963-0252/8/i=3/a=202?key=crossref.56f39a7614b999c254cbe3bdbf28d523

[32] J. Jacquot, D. Milanesio, L. Colas, Y. Corre, M. Goniche, J. Gunn, S. Heuraux, and M. Kubič, "Radio-frequency sheaths physics: Experimental characterization on Tore Supra and related self-consistent modeling," *Physics of Plasmas*, vol. 21, no. 6, 2014.

[33] A. Lasa, D. Borodin, J. M. Canik, C. C. Klepper, M. Groth, A. Kirschner, M. Airila, I. Borodkina, R. Ding, and J. Contributors, "ERO modeling and sensitivity analysis of locally enhanced beryllium erosion by magnetically connected antennas *," *Nucl. Fusion*, vol. 58, p. 17, 2018. [Online]. Available: https://doi.org/10.1088/1741-4326/aa90c0

[34] R. Ochoukov, D. G. Whyte, D. Brunner, D. A. D'Ippolito, B. LaBombard, B. Lipschultz, J. R. Myra, J. L. Terry, and S. J. Wukitch, "ICRF-enhanced plasma potentials in the SOL of Alcator C-Mod," *Plasma Physics and Controlled Fusion*, vol. 56, no. 1, p. 15004, 1 2014.

[35] J. R. Myra, D. A. D'Ippolito, D. A. Russell, L. A. Berry, E. F. Jaeger, and M. D. Carter, "Nonlinear ICRF-plasma interactions," *Nuclear Fusion*, vol. 46, no. 7, p. S455–S468, 2006. [Online]. Available: http://stacks.iop.org/0029-5515/46/i=7/a=S08?key=crossref.31d13957aa1c526d9fe88b1528256b19

[36] J. R. Myra and D. A. D'Ippolito, "Radio frequency sheaths in an oblique magnetic field," *Physics of Plasmas*, vol. 22, no. 6, p. 62507, 2015. [Online]. Available: http://aip.scitation.org/doi/10.1063/1.4922848

[37] D. A. D'Ippolito, "Modeling of mixed-phasing antenna-plasma interactions applied to JET A2 antennas," in *AIP Conference Proceedings*, vol. 595, no. 1. AIP Publishing, 2 2003. [Online]. Available: http://aip.scitation.org/doi/abs/10.1063/1.1424157 pp. 114–117.

[38] T. G. Jenkins and D. N. Smithe, "High-performance finite-difference time-domain simulations of C-Mod and ITER RF antennas," in *AIP Conference Proceedings*, vol. 1689, no. 1. American Institute of Physics Inc., 12 2015. [Online]. Available: http://aip.scitation.org/doi/abs/10.1063/1.4936468 p. 030003.

[39] M. Bures, J. J. Jacquinot, M. F. Stamp, D. D. R. Summers, D. F. H. Start, T. Wade, D. A. D'Ippolito, and J. R. Myra, "Assessment of beryllium Faraday screens on the JET ICRF antennas," *Nuclear Fusion*, vol. 32, no. 7, pp. 1139–1145, 1992. [Online]. Available: http://iopscience.iop.org/article/10.1088/0029-5515/32/7/I05/pdf

[40] M. Elias and D. Curreli, "An explicit scheme to enforce charge conservation in transient Particle-in-Cell simulations with Maxwell-Boltzmann electrons," *Journal of Computational Physics*, vol. 409, p. 109320, 5 2020.

[41] K. L. Cartwright, J. P. Verboncoeur, and C. K. Birdsall, "Nonlinear hybrid Boltzmann–particle-in-cell acceleration algorithm," *Physics of Plasmas*, vol. 7, no. 8, pp. 3252–3264, 8 2000. [Online]. Available: http://aip.scitation.org/doi/10.1063/1.874191

[42] J. Carlsson, M. Manente, and D. Pavarin, "Implicitly charge-conserving solver for Boltzmann electrons," *Physics of Plasmas*, vol. 16, no. 6, p. 62310, 6 2009. [Online]. Available: http://aip.scitation.org/doi/10.1063/1.3152288

[43] R. Khaziev and D. Curreli, "hPIC: A scalable electrostatic Particle-in-Cell for Plasma–Material Interactions," *Computer Physics Communications*, vol. 229, pp. 87–98, 8 2018.

[44] F. F. Chen, *Introduction to plasma physics and controlled fusion*, 2016.

[45] D. J. Griffiths, *Introduction to electrodynamics*, 2015.

[46] J. R. Myra, D. Curreli, M. T. Elias, and T. G. Jenkins, "Recent progress in microscale modeling of RF sheaths," *Proceedings*, vol. 2254, p. 50007, 2020. [Online]. Available: https://doi.org/10.1063/5.0013522

[47] R. Khaziev and D. Curreli, "Ion energy-angle distribution functions at the plasma-material interface in oblique magnetic fields," *Phys. Plasmas*, vol. 22, p. 43503, 2015. [Online]. Available: https://doi.org/10.1063/1.4916910

[48] Y. Yamamura and H. Tawara, "Energy dependence of ion-induced sputtering yields from monatomic solids at normal incidence," *Atomic Data and Nuclear Data Tables*, vol. 62, no. 2, pp. 149–253, 3 1996.

[49] D. Van Houtte, "Current status of the west project," CEA, Tech. Rep., 2020.

[50] D. Nishijima, R. P. Doerner, M. J. Baldwin, A. Pospieszczyk, and A. Kreter, "Experimental determination of S/XB values of W i visible lines," *Physics of Plasmas*, vol. 16, no. 12, p. 122503, 12 2009. [Online]. Available: https://aip.scitation.org/doi/abs/10.1063/1.3270108

[51] A. Geier, H. Maier, R. Neu, and K. Krieger, "Determination of the tungsten divertor retention at ASDEX Upgrade using a sublimation probe," *Plasma Physics and Controlled Fusion*, vol. 44, no. 10, pp. 2091–2100, 10 2002. [Online]. Available: https://iopscience.iop.org/article/10.1088/0741-3335/44/10/302 https://iopscience.iop.org/article/10.1088/0741-3335/44/10/302/meta

[52] "ADAS: OPEN-ADAS." [Online]. Available: https://www.adas.ac.uk/openadas.php

[53] S. Brezinsek, M. Laengner, J. W. Coenen, M. G. O'Mullane, A. Pospieszczyk, G. Sergienko, and U. Samm, "Spectroscopic determination of inverse photon efficiencies of W atoms in the scrape-off layer of TEXTOR," in *Physica Scripta*, vol. 2017, no. T170. Institute of Physics Publishing, 12 2017. [Online]. Available: https://iopscience.iop.org/article/10.1088/1402-4896/aa8a45 https://iopscience.iop.org/article/10.1088/1402-4896/aa8a45/meta p. 014052.

[54] J. J. Scholtz and R. Schmitz, "Secondary Electron Emission Properties," *Philips Journal of Research*, vol. 50, no. 3-4, pp. 375–389, 1996.

APPENDIX A

SECONDARY ELECTRON EMISSION

Electron emission is a phenomenon observed when electrons are emitted from plasma facing surfaces. The electron emission can be through several pathways, each relevant under different conditions. When energetic electrons, such as the ones observed in RF sheaths, strike the plasma facing component, they lead to the emission of one or more electrons [54]. If the emission happens after the surface is bombarded with charged ions and electrons, the phenomena is known as Secondary Electron Emission (SEE). SEE is particularly relevant in hot plasma conditions like tokamaks and RF sheaths.

Capturing the dynamics between plasma sheaths and electron emission maybe relevant to RF sheaths simulations. Emitted electrons force the plasma to send more electrons to the wall in order to balance the ion flux and maintain charge neutrality. This decreases the resulting plasma sheath potential. The effect of electron emission on the plasma potential is illustrated in Fig. A.1. In RF sheaths, with large plasma sheath potentials, this mechanism can provide a negative feedback loop limiting the RF sheaths to an upper limit on plasma sheath potentials.

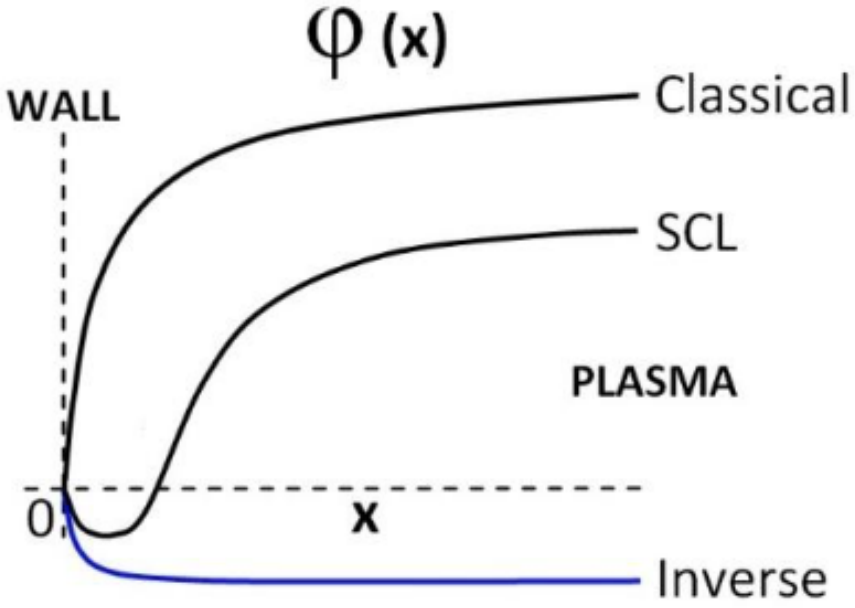

Figure A.1: Qualitative illustration of plasma potential in different SEE conditions. Classical, Space Charge limited, and inverse plasma sheath [14].

A.1 Effect of secondary electrons on RF potentials

In high magnetic field RF sheath configurations, the effect of secondary electrons on the plasma sheath is suppressed. The emitted secondary electrons are quickly redeposited into the plasma surface due to their gyro-motion. A competing force is the high electric field perpendicular to the plasma surface that aids emitted electrons in escaping to the plasma sheath. In order to evaluate the expected contributions and effects that secondary electrons has on RF sheaths, and thus the importance of including it in our model, we performed a preliminary study into the percentage of secondary electrons that escape into the plasma.

Model

We developed a model to estimate the percentage of emitted electrons that are redeposited on the surface. Electrons are emitted from the surface with energies ranging from $5-35$ eV and with angles $0°-90°$. Our model pushes the emitted electrons using a Boris pusher with a frequency correction in static magnetic and electric fields. Electrons are deemed to have been redeposited if their path crosses the emission surface within a 100 cyclotron cycles. The particle pusher model is summarized in Eqs. A.1-A.4:

$$\mathbf{r^{t+1}} = \mathbf{r^t} + \mathbf{v^{t+\frac{1}{2}}}\boldsymbol{\Delta}\mathbf{t} \tag{A.1}$$

$$v_{\parallel} = v_{\parallel}^0 + \frac{q}{m}E_{\parallel}\Delta t \tag{A.2}$$

$$v_{\perp}^{t+\frac{1}{2}} = v_{\perp}^{t-\frac{1}{2}} + \alpha_c\left[\frac{q\mathbf{E}}{m}\Delta t(v_{\perp}^{t+\frac{1}{2}} - v_{\perp}^{t-\frac{1}{2}}) \times \frac{q\mathbf{B}}{m}\frac{\Delta t}{2}\right] \tag{A.3}$$

$$\alpha_c = \frac{2m}{q\mathbf{B}\boldsymbol{\Delta}\mathbf{t}}\tan\frac{q\mathbf{B}\boldsymbol{\Delta}\mathbf{t}}{2m} \tag{A.4}$$

where $\mathbf{r^t}$ and $\mathbf{v^t}$ are the electron's position and velocity vectors at time step t,$v_{\parallel}$ and $v_{\perp}$ are the velocity components parallel and perpendicular to the magnetic field B. The electron mass m and charge q as well as the electric field E are used in the calculation of α_c the frequency correction factor.

The magnetic and electric field are set to constant values, taken to represent RF sheath profiles presented in Sec. 3.1. The analysis was performed by scanning over all possible emitted angles, emitted electron energy range from $5-35$ eV and magnetic fields from $1-4$ T.

Simulation results

Tab. A.1 shows the maximum percentage of electron Esp escaping for various B. As the magnetic field strength increases, more electrons are trapped and redeposited to the plasma surface. This is attributed to the effect of the magnetic field strength on the electron gyro orbits.

We focus on the case of $B = 3$ T, the magnetic field strength that resembles the conditions used for WEST. The results of our simulation are presented in Fig. A.2 for the case of $B = 3$ T. The X and Y axis are the electron emitted energy and angle. The angular scan is provided in polar coordinates. Electrons escaping into the plasma sheath are shown in blue and electrons redeposited into the solid Plasma facing components are shown in red.

The highest percentage of electrons escaping into the plasma sheath is 1%. This can be attributed to the strong magnetic field at the surface of the ICRF antenna that redeposits most electrons within one gyro orbit. The escaping electrons leave the surface with an emission angle close to 0° as seen in Fig. A.2. A percentage less than 1% of the emitted electrons is not expected to play an important role in the plasma sheath potential. This provides justification for the approximation of not including secondary electron emission used in our RF sheath model.

Table A.1: Maximum percentage of electrons Esp escaping into the plasma for various magnetic field strengths B[T].

B[T]	1	2	3	4
Esp	2.5%	1.3%	1%	0.6%

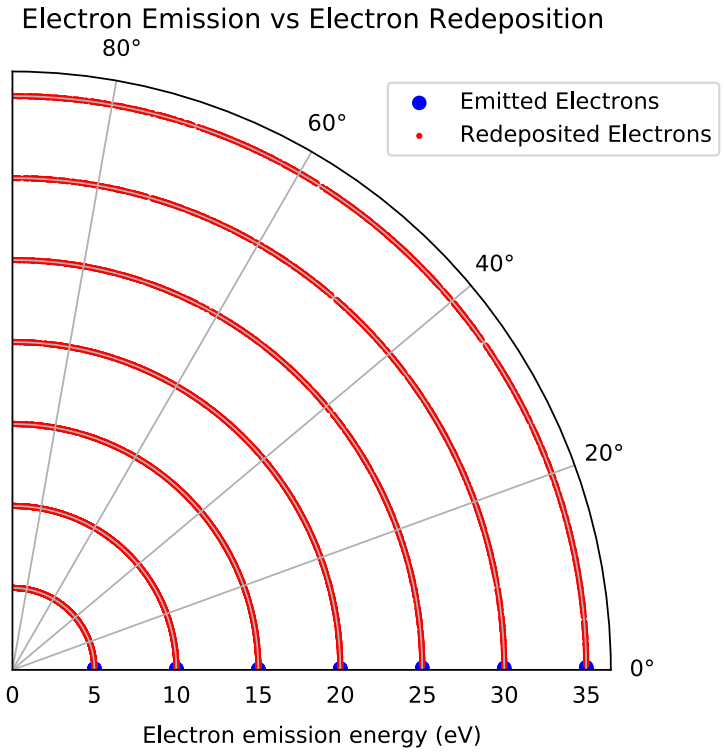

Figure A.2: Secondary Electron Emission vs Secondary electron redeposition. Plot shown in polar coordinates. X and Y axis represent the electron sputtering energy and angle respectively. Electrons escaping into the plasma sheath are shown in blue and electrons redeposited into the solid Plasma facing components are shown in red.